



HAL
open science

The planar rocking-block: analysis of kinematic restitution laws, and a new rigid-body impact model with friction

Hongjian Zhang, Bernard Brogliato

► **To cite this version:**

Hongjian Zhang, Bernard Brogliato. The planar rocking-block: analysis of kinematic restitution laws, and a new rigid-body impact model with friction. [Research Report] RR-7580, 2011. inria-00579231v1

HAL Id: inria-00579231

<https://inria.hal.science/inria-00579231v1>

Submitted on 23 Mar 2011 (v1), last revised 23 Mar 2011 (v2)

HAL is a multi-disciplinary open access archive for the deposit and dissemination of scientific research documents, whether they are published or not. The documents may come from teaching and research institutions in France or abroad, or from public or private research centers.

L'archive ouverte pluridisciplinaire **HAL**, est destinée au dépôt et à la diffusion de documents scientifiques de niveau recherche, publiés ou non, émanant des établissements d'enseignement et de recherche français ou étrangers, des laboratoires publics ou privés.

*The planar rocking-block: analysis of kinematic
restitution laws, and a new rigid-body impact model
with friction*

Hongjian Zhang — Bernard Brogliato

N° 7580

March 2011

Modeling, Optimization, and Control of Dynamic Systems



*Rapport
de recherche*

The planar rocking-block: analysis of kinematic restitution laws, and a new rigid-body impact model with friction

Hongjian Zhang*, Bernard Brogliato †

Theme : Modeling, Optimization, and Control of Dynamic Systems
Équipes-Projets Bipop

Rapport de recherche n° 7580 — March 2011 — 106 pages

Abstract: In this report we first analyse the capabilities of a generalized kinematic (Newton's like) restitution law for the modeling of a planar rigid block that impacts a rigid ground. The relationships with the classical angular velocity restitution law for rocking motion are examined in detail. Then a new impact law based on the Darboux-Keller's approach with energetic coefficients of restitution (proposed recently in [31, 32, 71, 34]) and which allows one to incorporate Coulomb's friction, is applied and many cases are studied numerically. The numerical results show that this restitution law is able to reproduce a rich set of block motions with complex energy dispersion effects, that are consistent with everyday life observations. Most importantly it is shown that the kinetic angle between the two unilateral constraints is a parameter that plays a fundamental role in the block's motion, and a critical kinetic angle θ_c is exhibited that allows one to split the blocks into two main classes: slender blocks with a height/width ratio larger than θ_c , and flat blocks when the ratio is smaller than θ_c . The value of θ_c varies with the friction value. Detailed comparisons with experimental results on free-rocking and with base excitation found in the literature [46, 29, 17] are proposed and confirm the validity of the proposed model. New results concerning the conditions for the onset or rocking and for the overturning are presented. All the simulations are done with an event-driven algorithm that is available on the INRIA SICONOS open-source software platform.

Key-words: Rocking block, rigid body, overturning, Coulomb friction, multiple impact, event-driven simulation, experimental results, restitution law, restitution coefficient

* State Key Laboratory for Turbulence and Complex Systems, College of Engineering, Peking University, Beijing 100871, People's Republic of China. Work performed while at INRIA, BIPOP project-team, ZIRST Montbonnot, 655 avenue de l'Europe, 38334 Saint Ismier, France, e-mail: hongjian.zhang@inrialpes.fr, zhanghj@pku.edu.cn; Funded by China Scholarship Council No. 2009601276 and by ANR project Multiple Impact ANR-08-BLAN-0321-01.

† INRIA, BIPOP project-team, ZIRST Montbonnot, 655 avenue de l'Europe, 38334 Saint Ismier, France, e-mail: Bernard.Brogliato@inrialpes.fr

Analyse et simulation du “rocking-block”: analyse de lois de restitutions cinématiques, et une nouvelle loi d’impact avec frottement

Résumé : Dans ce rapport nous commençons par l’analyse d’une loi d’impact cinématique généralisée (à la Newton) pour le cas d’un bloc planaire qui impacte un sol rigide. Les relations avec la loi classique de restitution de vitesse angulaire sont examinées en détail. Ensuite une nouvelle loi d’impact proposée dans [31, 32, 71, 34] est appliquée. Les simulations numériques concernent les dynamiques de type free-rocking (avec fondation fixe), ainsi que les dynamiques avec fondation mobile, telle que le retournement (overturning). Les résultats numériques sont comparés à de nombreux résultats expérimentaux qui les valident.

Mots-clés : Bloc oscillant, corps rigide, retournement, frottement de Coulomb, impact multiple, simulation par évènements, résultats expérimentaux, loi de choc, coefficient de restitution.

1 Introduction

Modeling the dynamics of a rigid block hitting a rigid ground has attracted the attention of scientists in the field of earthquake engineering for a long time [47, 39], see *e.g.* [4, 5, 19, 23, 29, 45, 50, 51, 53, 56, 62, 63, 64, 65, 67, 68, 70] to cite a few recent works. This is also of interest for the study of blocks falling on very steep planes in the mountain [22], and whose trajectories need to be estimated with sufficient accuracy. In parallel the field of impact dynamics has witnessed an intense activity in the past twenty-five years, see *e.g.* [10, 21, 61] and references therein. It happens that the problem of modeling impacts with friction is a tough issue, especially when there are several simultaneous contact points and when friction is present during the impacts (multiple impacts with friction). Typically the so-called *rocking block* problem involves double-impacts with friction, when one assumes that the base contacts the ground at two points only. Together with chains of balls (Newton's cradles), the rocking block is an apparently simple multibody system (the block and the ground), however it involves multiple impacts with friction and its modeling is consequently not simple at all. In this paper we first analyse the capabilities of a generalized kinematic restitution law, *i.e.* a restitution law based on restitution coefficients which are defined as ratios of post- and pre-impact velocities. The relationships with the classical angular velocity restitution law introduced in [23] and used since then in many papers on the rocking block, are studied. The major drawback of such restitution laws is that they do not allow to predict the extremely rich dynamical behavior of a block with frictional impacts, because they model in a very crude way the frictional phenomenon at the impacts. The second part of the paper is dedicated to study in detail the block's dynamics with double-impacts and friction, using the multiple impact model developed in [31, 32, 71, 34]. This model is based on the Darboux-Keller model studied previously for single impacts with friction in two and three dimensions [10, 61]. It has been extended to the multiple impact case in [31, 32, 71, 34], without and with friction. In these references many numerical simulation results are shown and compared to experimental results obtained elsewhere on chains of balls [18] and Newton's cradle [11], as well as for a bouncing dumbbell [14]. Those comparisons are quite successful and they demonstrate that the proposed model encapsulates the most important features of multiple impacts for rate-independent materials. In particular both the dissipation (with energetic coefficients of restitution) and the dispersion effects are well reproduced. In sections 3 through 7 simulation results are presented for the block, in the case of no gravity no friction, gravity and no friction, and gravity and friction. Since there are too many parameters that may be varied in such a system (two restitution coefficients, two friction coefficients, the elasticity constant, the dimensions, the mass, the initial state), it is important to provide a simple guide-line that indicates general patterns for the block motions. It is shown here that the kinetic angle between the constraints plays a significant role.

2 The generalized kinematic restitution approach

In this section we consider the block as a lagrangian system subject to unilateral constraints in its configuration space. The objective of this paper is the modeling of multiple impacts, which we precisely define now.

Definition 1. *Let a mechanical lagrangian system have generalized coordinates $q \in \mathbb{R}^n$, and a configuration space $\mathcal{C} \subseteq \mathbb{R}^n$. Let it be subject to a set of unilateral constraints $f_i(q) \geq 0$, $1 \leq i \leq m$, where the functions f_i are continuously differentiable. We denote $\Sigma_i = \{q \in \mathbb{R}^n \mid f_i(q) = 0\}$ the co-dimension one constraints boundaries. The admissible domain is therefore a finitely represented set $\Phi = \{q \in \mathbb{R}^n \mid f_i(q) \geq 0, 1 \leq i \leq m\} \subseteq \mathcal{C}$. The boundary $Bd(\Phi)$ of Φ is the union of facets $\bar{\Sigma}_i \subseteq \Sigma_i$, $1 \leq i \leq m$, whose boundaries are made of co-dimension p subspaces that correspond to intersections between p surfaces Σ_i . A collision with such a co-dimension p surface of $Bd(\Phi)$ is a multiple impact of order p , or a p -impact.*

When a p -impact occurs, the system undergoes p simultaneous impacts at p different points. The planar block will undergo simple (one) and 2-impacts. In multiple impacts, two major energetical effects play a role: the *dissipation* of the energy, and the *dispersion* of the energy. In a multibody system the dispersion characterizes the bodies post-impact kinetic energies. In a single body system like the rocking block we shall rather speak of dispersion among the contact points.

2.1 The block dynamics

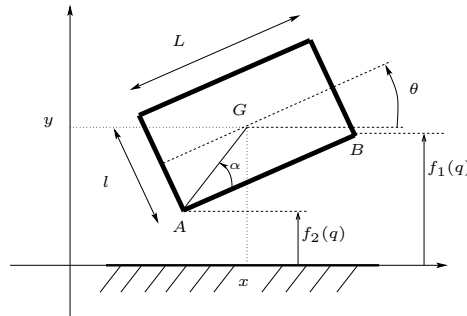


Figure 1: The block.

Let us consider the block as a three degrees of freedom planar homogeneous solid, with generalized coordinates $q^T = (x, y, \theta)$, where x and y and the horizontal and vertical positions of the center of gravity, θ is the angular position, see figure 1. Following [10, Chapter 6] we infer that the block, when $y \leq \sqrt{l^2 + L^2}$, is subject to two unilateral constraints:

$$\begin{cases} f_1(q) = \theta + \theta_{\max}(y) \geq 0 \\ f_2(q) = -\theta + \theta_{\max}(y) \geq 0 \end{cases} \quad (1)$$

where $\theta_{\max} = -\arccos\left(\frac{2y}{\sqrt{l^2+L^2}}\right) + \arctan\left(\frac{L}{l}\right)$. These two constraints can be equivalently written as:

$$\begin{cases} f_1(q) = y - \frac{l}{2} \cos(\theta) + \frac{L}{2} \sin(\theta) \geq 0 \\ f_2(q) = y - \frac{l}{2} \cos(\theta) - \frac{L}{2} \sin(\theta) \geq 0 \end{cases} \quad (2)$$

where $f_1(q) \geq 0$ expresses that point B cannot penetrate into the ground, while $f_2(q) \geq 0$ expresses the same for point A . The underlying assumption is that the block/ground contact can be represented by the two points A and B at the corners. Obviously, when the block rotates by an angle larger than $\pm\frac{\pi}{2}$, the contact points change and one has to reconsider new unilateral constraints (this is what happens when so-called *overturn* occurs). The admissible domain defined by the unilateral constraints in the (y, θ) plane, is depicted in section 4 (see *e.g.* figures 7 (a), 8 (a) and 9 (a)). It is not convex. One can already see two particular initial angles: the critical angles $\pm\theta_c$ at which the curve (θ_0, y_G) attains its maximum values, and $\theta_0 = 0$. The critical angle corresponds to a colinear single impact of the block at A or B , with AG (resp. BG) colinear to the normal to the ground, and therefore $\theta_c = \frac{\pi}{2} - \alpha$. One expects that this is linked to the overturn of the block. At $\theta_0 = 0$ one has a double-impact (A and B hit the ground simultaneously). The dynamics of the block subject to frictionless constraints and gravity is:

$$\begin{cases} m\ddot{x}(t) = 0 \\ m\ddot{y}(t) = \lambda_{n,1}(t) + \lambda_{n,2}(t) - mg \\ I_G\ddot{\theta}(t) = \lambda_{n,1}(t)\left(\frac{l}{2} \sin(\theta(t)) + \frac{L}{2} \cos(\theta(t))\right) + \lambda_{n,2}(t)\left(\frac{l}{2} \sin(\theta(t)) - \frac{L}{2} \cos(\theta(t))\right) \\ 0 \leq \lambda_n(t) \perp f(q(t)) \geq 0 \end{cases} \quad (3)$$

where the complementarity conditions are componentwise, $f(q)^T = (f_1(q), f_2(q))$, $\lambda_n^T = (\lambda_{n,1}, \lambda_{n,2})$. For a block with G at the geometric center one has $I_G = \frac{m}{12}(l^2 + L^2)$. In (3) we have not yet considered the impacts with the ground, but only those phases of motion where the contact force is a bounded function of time. From (2) and (3) the Linear Complementarity Problem (LCP) that allows one to calculate the contact forces during the smooth phases of motion (*i.e.* outside impacts) is given by:

$$0 \leq \lambda_n(t) \perp \frac{d^2}{dt^2} f(q(t)) = A(\theta)\lambda_n + B(\theta, \dot{\theta}) \geq 0 \quad (4)$$

$$\text{with } A(\theta) = \begin{pmatrix} \frac{1}{m} + \frac{1}{4I_G}(l \sin(\theta) + L \cos(\theta))^2 & \frac{1}{m} + \frac{1}{4I_G}(l^2 \sin^2(\theta) - L^2 \cos^2(\theta)) \\ \frac{1}{m} + \frac{1}{4I_G}(l^2 \sin^2(\theta) - L^2 \cos^2(\theta)) & \frac{1}{m} + \frac{1}{4I_G}(l \sin(\theta) - L \cos(\theta))^2 \end{pmatrix},$$

$$A(\theta) = A^T(\theta), \quad B(\theta, \dot{\theta}) = \begin{pmatrix} -g + \frac{1}{2}\dot{\theta}^2(l \cos(\theta) - L \sin(\theta)) \\ -g + \frac{1}{2}\dot{\theta}^2(l \cos(\theta) + L \sin(\theta)) \end{pmatrix}. \quad \text{One calculates}$$

that $\det(A(\theta)) = \frac{L^2}{mI_G} \cos^2(\theta)$ so that $A(\theta)$ is positive definite except at $\theta = \pm\frac{\pi}{2}$. These values are however outside the range of block orientations within which the analysis is done. We conclude that for all angles $\theta \in (-\frac{\pi}{2}, \frac{\pi}{2})$ $A(\theta) > 0$ and the normal contact force λ_n can be computed uniquely as the solution of the LCP in (4) whatever θ and $\dot{\theta}$. $A(\theta)$ is the so-called Delassus' matrix of the system (2) (3).

When Coulomb's friction acts at the contact points the dynamics in (3) becomes:

$$\left\{ \begin{array}{l} m\ddot{x}(t) = \lambda_{t,1}(t) + \lambda_{t,2}(t) \\ m\ddot{y}(t) = \lambda_{n,1}(t) + \lambda_{n,2}(t) - mg \\ I_G\ddot{\theta}(t) = \lambda_{n,1}(t) \left(\frac{l}{2} \sin(\theta(t)) + \frac{L}{2} \cos(\theta(t)) \right) + \lambda_{n,2}(t) \left(\frac{l}{2} \sin(\theta(t)) - \frac{L}{2} \cos(\theta(t)) \right) \\ \quad + \left(\frac{l}{2} \cos(\theta) - \frac{L}{2} \sin(\theta) \right) \lambda_{t,1} + \left(\frac{l}{2} \cos(\theta) + \frac{L}{2} \sin(\theta) \right) \lambda_{t,2} \\ \\ 0 \leq \lambda_n(t) \perp f(q(t)) \geq 0 \\ \lambda_{t,i}(t) \in -\mu_i \lambda_{n,i}(t) \operatorname{sgn}(v_{t,i}(t)), i = 1, 2 \end{array} \right. \quad (5)$$

where $\mu_i > 0$ is the friction coefficient at contact i , and $v_{t,i}$ is the tangential (more generally, horizontal) velocity at the point i , *i.e.* $v_{t,1} = \dot{x} + \left(\frac{l}{2} \cos(\theta) + \frac{L}{2} \sin(\theta) \right) \dot{\theta}$ at B and $v_{t,2} = v_{t,1}$ at A . Notice that if the contact point i detaches then the complementarity conditions imply that $\lambda_{n,i} = 0$ so $\lambda_{t,i} = 0$. The dynamics in (5) stands for fixed ground. If the base has a horizontal motion denoted as $x_b(t)$, then the friction law is changed to $\lambda_{t,i}(t) \in -\mu_i \lambda_{n,i}(t) \operatorname{sgn}(v_{t,i}(t) - v_b(t))$, $i = 1, 2$, where $v_b(t)$ is the base horizontal velocity.

Remark 1. *The Coulomb's law is set-valued at 0 velocity, i.e. we consider that $\operatorname{sgn}(0) = [-1, 1]$.*

Since we will be interested later in the onset of rocking for the block on a moving base, let us first study two important behaviours which are due to the presence of friction: stick/slip and detachment.

2.2 A generalized kinematic restitution mapping

We take it as granted here that the positions are continuous functions of time while the velocities are right-continuous of local bounded variations, with possible discontinuities at the impact times, see [7, 38, 15] for more details on such system's well-posedness. Let us introduce a specific change of generalized velocities [10, Chapter 6] (see also [37]) for an n -dimensional lagrangian system subject to m unilateral constraints $f_i(q) \geq 0$, $1 \leq i \leq m$, that we suppose to be mutually independent. The vector $\mathbf{n}_{q,i} = \frac{M^{-1}(q)\nabla f_i(q)}{\sqrt{\nabla f_i(q)^T M^{-1}(q)\nabla f_i(q)}}$

denotes the unit normal vector to the surface $\Sigma_i = \{q \in \mathbb{R}^n \mid f_i(q) = 0\}$, in the kinetic metric¹. One may form an orthonormal basis by completing the $\mathbf{n}_{q,i}$ normal vectors with $n - m$ tangential vectors $\mathbf{t}_{q,i}$ such that $\mathbf{n}_{q,i}^T M(q) \mathbf{t}_{q,j} = 0$ for all $i \in \{1, \dots, m\}$ and $j \in \{m + 1, \dots, n\}$, and such that $\mathbf{t}_{q,j}^T M(q) \mathbf{t}_{q,j} = 1$. We have thus constructed an orthonormal basis in the configuration space \mathcal{C} of the system, at the point q on the boundary of the admissible domain $\Phi = \{q \in \mathcal{C} \subseteq \mathbb{R}^n \mid f_i(q) \geq 0, 1 \leq i \leq m\}$. Let $\Xi(q) = \begin{pmatrix} \mathbf{n}_q^T \\ \mathbf{t}_q \end{pmatrix}$ be an $n \times n$

¹The kinetic metric is the metric defined with the mass matrix $M(q) = M^T(q) > 0$, such that for two vectors x and y the inner product is $x^T M(q) y$.

full-rank matrix, $\mathbf{n}_q^T = \begin{pmatrix} \mathbf{n}_{q,1}^T \\ \vdots \\ \mathbf{n}_{q,m}^T \end{pmatrix}$, $\mathbf{t}_q^T = \begin{pmatrix} \mathbf{t}_{q,m+1}^T \\ \vdots \\ \mathbf{t}_{q,n}^T \end{pmatrix}$, and $\mathcal{M}(q) = \Xi(q)M(q)$.

The transformed velocities are given by:

$$\begin{pmatrix} \dot{q}_{\text{norm}} \\ \dot{q}_{\text{tan}} \end{pmatrix} = \mathcal{M}(q)\dot{q} \quad (6)$$

where a normal and a tangential components appear. Notice that $\dot{q}_{\text{norm},i} = \frac{\nabla f_i^T(q)\dot{q}}{\sqrt{\nabla f_i(q)^T M^{-1}(q)\nabla f_i(q)}}$. The lagrangian dynamics is then transformed into [10, Section 6.2]:

$$\begin{pmatrix} \ddot{q}_{\text{norm}} \\ \ddot{q}_{\text{tan}} \end{pmatrix} + F(q, \dot{q}) = \begin{pmatrix} \mathbf{n}_q^T \nabla f(q) \lambda_n \\ 0 \end{pmatrix} \quad (7)$$

where it is still assumed that the constraints are frictionless. The term $F(q, \dot{q})$ gathers smooth, bounded functions only. The advantage of this velocity transformation is that the system appears to be decoupled because the contact force does not act in the tangential direction. The dynamics in (7) is not in a lagrangian formalism, however. Notice that $\mathbf{n}_q^T \nabla f(q)$ is the Delassus' matrix with normalizations of the components. If all the constraints are pairwise orthogonal in the kinetic metric, then $\mathbf{n}_q^T \nabla f(q) = \text{diag}(\sqrt{\nabla f_i^T(q)M^{-1}(q)\nabla f_i(q)})$: the normal directions are also decoupled. In such a case the kinetic angle between all the couples of surfaces, *i.e.* $\theta_{i,j} = (\widehat{\Sigma_i, \Sigma_j})_{M(q)}$, $i \neq j$, are equal to $\frac{\pi}{2}$. We recall that

$$\theta_{ij} = \pi - \arccos \frac{\mathbf{n}_{q,i}^T M(q) \mathbf{n}_{q,j}}{\|\mathbf{n}_{q,i}\|_{M(q)} \|\mathbf{n}_{q,j}\|_{M(q)}} \text{ so } \theta_{ij} = \pi - \arccos \frac{\nabla f_i(q)^T M^{-1}(q) \nabla f_j(q)}{\sqrt{\nabla f_i(q)^T M^{-1}(q) \nabla f_i(q)} \sqrt{\nabla f_j(q)^T M^{-1}(q) \nabla f_j(q)}}$$

Remark 2. For the rocking block, the kinetic angle θ_{12} between the two constraints is given by $\theta_{12} = \pi - \arccos \left(\frac{l^2 - 2L^2}{l^2 + 4L^2} \right)$ at $\theta = 0$. Denoting the aspect ratio $a = \frac{l}{L}$ we may rewrite it as $\theta_{12} = \pi - \arccos \left(\frac{a^2 - 2}{a^2 + 4} \right)$: there is a one-to-one correspondance between a and θ_{12} . It satisfies $\theta_{12} = \frac{\pi}{2}$ if $l = \sqrt{2}L$, $0 < \theta_{12} < \frac{\pi}{2}$ if $0 < l < \sqrt{2}L$ (flat block), and $\pi > \theta_{12} > \frac{\pi}{2}$ if $l > \sqrt{2}L$ (slender block). The interest of studying the block's dynamics as a function of the kinetic angle between the two boundaries at $\theta = 0$, is that it allows us to determine that a block is not of the slender type when $l > L$, but when $l > \sqrt{2}L$.

Remark 3. The calculations are made in this paper for a perfect rectangular homogenous block. It is clear that all the calculations can easily be done for more general blocks when for instance the center of mass and the geometric center do not coincide, or when the block's geometry is not rectangular. Since most of the literature on the topic deals with perfect blocks we however lead our developments with such an assumption, keeping in mind that generalizations are quite possible. For instance all the calculations that are made next in this paper could be led keeping I_G and not specifying its value.

²The kinetic angle is obtained after subtraction from π because the normal vectors point outside the admissible domain of the configuration space.

At an impact time we deduce from (7), the contact force being a Dirac measure $\lambda_n = p_n(t)\delta_t$, that:

$$\begin{cases} \dot{q}_{\text{norm}}(t^+) - \dot{q}_{\text{norm}}(t^-) = \mathbf{n}_q^T \nabla f(q) p_n(t) \\ \dot{q}_{\text{tan}}(t^+) - \dot{q}_{\text{tan}}(t^-) = 0, \end{cases} \quad (8)$$

which is similar to the impact dynamics of a particle hitting a frictionless wall, where the normal and the tangential directions are decoupled. The percussion $p_n(t)$ is the density of the measure λ_n at time t , and is indeed a function of time. Then it is natural to mimic the case of a particle and to define a generalized Newton's (or kinematic) restitution rule as:

$$\dot{q}_{\text{norm}}(t^+) = -\mathcal{E}_n \dot{q}_{\text{norm}}(t^-), \quad \dot{q}_{\text{norm},i}(t^-) < 0, \quad i \in \{1, \dots, m\} \quad (9)$$

at an impact time t where all the m surfaces are collided at the same time, where t^+ and t^- indicate the right and left limits as usual. The matrix $\mathcal{E}_n \in \mathbb{R}^{m \times m}$ is a matrix of normal restitution. From (9) it follows that \dot{q}_{tan} is continuous at such t . It is easy to compute that the loss of kinetic energy is given by $T_L(t) = T(t^+) - T(t^-) = \frac{1}{2} \dot{q}_{\text{norm}}^T(t^-) (\mathcal{E}_n^T \mathcal{E}_n - I_m) \dot{q}_{\text{norm}}(t^-)$. From the *energetic constraint* that $T_L(t) \leq 0$ one finds that $\mathcal{E}_n^T \mathcal{E}_n - I_m \leq 0$ is sufficient to guarantee the kinetic energy loss. Actually a less stringent condition is that $-\mathcal{E}_n^T \mathcal{E}_n + I_m$ is a *copositive* matrix on the cone \mathbb{R}_-^m . Since an impact has occurred with all m surfaces, one has $\dot{q}_{\text{norm},i}(t^-) < 0$ for all $1 \leq i \leq m$. The post-impact velocity has to be admissible, *i.e.* it has to point inside the admissible domain Φ : this is a *kinematic constraint*. In other words $\dot{q}_{\text{norm},i}(t^+) \geq 0$ for all $1 \leq i \leq m$. If \mathcal{E}_n is diagonal with m non negative coefficients $e_{n,i}$, then this implies that $e_{n,i} \geq 0$, whereas the energetic constraint implies that $-1 \leq e_{n,i} \leq 1$. We deduce that the energetic and the post-impact velocity admissibility imply that $e_{n,i} \in [0, 1]$ when $\mathcal{E}_n = \text{diag}(e_{n,i})$. A third constraint is the form of the contact force (and of its impulse as a consequence), that we name the *kinetic constraint*. In (7) we have supposed that the constraints are frictionless, *i.e.* there are no contact forces in the generalized tangential direction. This means that the right-hand-side is as in (7), and it implies that \dot{q}_{tan} is continuous at the impact time, see (8). One also has an additional kinetic constraint $p_n(t) \geq 0$.

The above three constraints (energetic, kinetic and kinematic) tell us that the following has to hold: $\mathcal{E}_n^T \mathcal{E}_n - I_m \leq 0$, $p_n \geq 0$ under (8) and (9), *i.e.* $(\mathbf{n}_q(t)^T \nabla f(q(t)))^{-1} (\mathcal{E}_n + I_n) \dot{q}_{\text{norm}}(t^-) \leq 0$, and $\mathcal{E}_n \geq 0$ if it is a diagonal matrix. These conditions will be examined and derived for particular cases of the block motion in the next section.

It is obvious that by modifying the kinetic constraint (*i.e.* the form of the contact force impulse) one may also define a general restitution matrix

$$\mathcal{E} = \begin{pmatrix} \mathcal{E}_n & 0 \\ 0 & \mathcal{E}_{\text{tan}} \end{pmatrix} \text{ such that}$$

$$\begin{pmatrix} \dot{q}_{\text{norm}}(t^+) \\ \dot{q}_{\text{tan}}(t^+) \end{pmatrix} = -\mathcal{E} \begin{pmatrix} \dot{q}_{\text{norm}}(t^-) \\ \dot{q}_{\text{tan}}(t^-) \end{pmatrix} \quad (10)$$

and \dot{q}_{tan} may jump, with generalized tangential restitution coefficients $e_{t,i}$, $m+1 \leq i \leq n$. By suitably varying the coefficients of \mathcal{E} , then the whole space of admissible post-impact velocities can be spanned, which is sometimes

viewed as a desired property for a restitution law [12, 21]. An example of such a restitution matrix will be given in remark 9. In the frictionless case one has $\mathcal{E} = \begin{pmatrix} \mathcal{E}_n & 0 \\ 0 & I_{n-m} \end{pmatrix}$.

Remark 4. *The above velocity decomposition and restitution rule is interesting because it allows one to decouple the normal and tangential directions for a lagrangian system in its configuration space, hence recovering the case of a particle hitting a frictionless wall. Moreover it may be given several nice interpretations following the developments in [21]. First notice that $\dot{q} = \sum_{i=1}^m \dot{q}_{\text{norm},i} \mathbf{n}_{q,i} + \sum_{i=m+1}^n \dot{q}_{\text{tan},i} \mathbf{t}_{q,i}$. This decomposition is the same as the one in [21, §6] and it follows in particular that the impact law in (9) is equivalent to Moreau's impact law with a global dissipation index, provided the kinetic constraint is properly chosen. Such a kinematic impact law is known not to cover the whole set of admissible post-impact velocities (see e.g. Figure 11 in [21]). This will be illustrated on the rocking block example in the next section.*

It is important however to keep in mind that these developments and conclusions hold as long as the constraints are perfect, i.e. there are no tangential forces at the contact points. One objective of this paper is to study what happens when Coulomb's friction is added at the impacts.

2.3 Application to the block impact dynamics

Let us see now how the above material may be applied to the particular case of the planar block. More specifically in this section we will investigate how the rocking motion of the block may be modeled with the above generalized kinematic law. The rocking motion is an interesting one because it involves a double-impact each time one of the corners hits the ground. In this paper we will focus on several particular motions of the block: free rocking with sliding contact points, half-rocking, free-rocking with sticking contact points. Each one of these implies a set of kinematic constraints (equality constraints on the velocities).

The frictionless impact dynamics of the block is given by:

$$\begin{cases} m(\dot{x}(t^+) - \dot{x}(t^-)) = 0 \\ m(\dot{y}(t^+) - \dot{y}(t^-)) = p_{n,1}(t) + p_{n,2}(t) \\ I_G(\dot{\theta}(t^+) - \dot{\theta}(t^-)) = p_{n,1}(t)(\frac{1}{2} \sin(\theta(t)) + \frac{L}{2} \cos(\theta(t))) + p_{n,2}(t)(\frac{1}{2} \sin(\theta(t)) - \frac{L}{2} \cos(\theta(t))) \end{cases} \quad (11)$$

where t is the impact time, and we recall that being the density of the measure λ_n at time t , the impulse p_n is a function of time. One can apply the restitution rule in (9) with $\mathcal{E}_n = \text{diag}(e_{n,1}, e_{n,2})$, so that there are five unknowns (three post-impact velocities and two impulses) and five equations. One has $\dot{q}_{\text{norm},1} = \frac{\dot{y} + (\frac{1}{2} \sin(\theta) + \frac{L}{2} \cos(\theta)) \dot{\theta}}{\sqrt{\frac{1}{m} + \frac{1}{4I_G} (L \sin(\theta) + L \cos(\theta))^2}}$, $\dot{q}_{\text{norm},2} = \frac{\dot{y} + (\frac{1}{2} \sin(\theta) - \frac{L}{2} \cos(\theta)) \dot{\theta}}{\sqrt{\frac{1}{m} + \frac{1}{4I_G} (L \sin(\theta) - L \cos(\theta))^2}}$ and $\dot{q}_{\text{tan}} = \sqrt{m} \dot{x}$. A particularity of the block is however that except if (i) $\theta(t) = 0$ in which case the two points A and B may hit the ground at the same time, there are only two possible other impact configurations: (ii) A (resp. B) is in lasting contact and the block hits the ground at B (resp. at A), (iii) A (resp. B) hits the ground while B (resp. A) is airborne. Let us study first the subcase of case (ii) that corresponds to a rocking motion of the block, *i.e.* when B sticks after the shock

while A detaches from the ground. We shall call *free-rocking* the rocking motion when the base is fixed and the block evolves freely from some initial state. The subcase of case (ii) where A (resp. B) keeps the contact after the shock and B (resp. A) rebounds will be called the *half-rocking* motion. Notice that the fact that a point keeps the contact does not mean that it is fixed: it may slide on the constraint surface. This is why we will introduce *sticking rocking* and *sliding rocking*. Sticking rocking occurs when the contact points are tangentially fixed (a tangential kinematic constraint is imposed), while sliding rocking occurs for frictionless systems. Notice that when there is no tangential effects at the contact points, then \dot{x} is constant so that the contact points necessarily slip on the ground when the block moves: free-rocking without friction occurs with slipping contact points. There are intermediate cases where the contact points may undergo stick and slip modes during impact and contact phases. However in this part we shall focus only on the above two limit cases (sticking and sliding). The general case of impacts with Coulomb's friction will be tackled in the other part of the paper.

2.3.1 Diagonal \mathcal{E}_n , $p_{n,1}(t) \neq 0$, $p_{n,2}(t) = 0$ (sliding rocking motion)

Suppose that the block rotates around A (i.e. $f_2(q) = 0$ on a non zero time interval, and we assume that $\lambda_{n,2}$ is a bounded function of time, i.e. $p_{n,2}(t) = 0$) and that B hits the ground and then sticks on it in the normal direction (it may slide). At the impact time one has $\theta(t) = 0$ and $\dot{q}_{\text{norm},2}(t^-) = 0$. One deduces that $\dot{y}(t^-) = \frac{L}{2}\dot{\theta}(t^-)$. The impact dynamics (11) together with (9) becomes:

$$\begin{cases} m\dot{x}(t^+) = \dot{x}(t^-) \\ m(\dot{y}(t^+) - \dot{y}(t^-)) = p_{n,1}(t) \\ I_G(\dot{\theta}(t^+) - \dot{\theta}(t^-)) = \frac{L}{2}p_{n,1}(t) \\ \dot{q}_{\text{norm},1}(t^+) = -e_{n,1}\dot{q}_{\text{norm},1}(t^-) \\ \dot{q}_{\text{norm},2}(t^+) = -e_{n,2}\dot{q}_{\text{norm},2}(t^-) = 0 \end{cases} \quad (12)$$

since $\dot{q}_{\text{norm},2}(t^-) = 0$ and \mathcal{E}_n is diagonal. Or equivalently (recall that $\theta(t) = 0$ at the double-impact):

$$\begin{cases} \dot{q}_{\text{norm}}(t^+) - \dot{q}_{\text{norm}}(t^-) = \begin{pmatrix} \frac{4L^2+l^2}{m(L^2+l^2)} & \frac{l^2-2L^2}{m(l^2+L^2)} \\ \frac{l^2-2L^2}{m(l^2+L^2)} & \frac{4L^2+l^2}{m(L^2+l^2)} \end{pmatrix} \begin{pmatrix} p_{n,1}(t) \\ p_{n,2}(t) \end{pmatrix} \\ \dot{q}_{\text{tan}}(t^+) = \dot{q}_{\text{tan}}(t^-) \\ \dot{q}_{\text{norm},1}(t^+) = -e_{n,1}\dot{q}_{\text{norm},1}(t^-) \\ \dot{q}_{\text{norm},2}(t^+) = -e_{n,2}\dot{q}_{\text{norm},2}(t^-) = 0 \end{cases} \quad (13)$$

From this we infer that

$$\dot{y}(t^+) = \frac{6L^2e_{n,1} + 2L^2 - l^2}{4L^2 + l^2}\dot{y}(t^-) \quad (14)$$

and

$$\dot{\theta}(t^+) = -\frac{6L^2e_{n,1} + 2L^2 - l^2}{4L^2 + l^2}\dot{\theta}(t^-). \quad (15)$$

Notice that the rocking motion implies that $e_{n,1} = 0$ because after the shock one has $f_1(q) = 0$ and $\dot{q}_{\text{norm},1}(t^+) = 0$ (the contact at B is lasting), so that

$\dot{y}(t^+) + \frac{L}{2}\dot{\theta}(t^+) = 0$. This together with $\dot{q}_{\text{norm},2}(t^+) = 0$ implies that $\dot{y}(t^+) = 0$ and $\dot{\theta}(t^+) = 0$, so that from (15) one has necessarily $l^2 = 2L^2$. We conclude that the impact map (9) with the assumption that $\lambda_{n,2}$ is a bounded function of time cannot model the rocking motion of the block and models only the most dissipative motion when the block comes at rest after the impact, for the case that the kinetic angle is equal to $\frac{\pi}{2}$.

From (15) and $e_{n,1} = 0$ one deduces that

$$\dot{\theta}(t^+) = -\frac{2L^2 - l^2}{4L^2 + l^2}\dot{\theta}(t^-) = -r\dot{\theta}(t^-), \quad (16)$$

and necessarily $r = 0$. By symmetry of the system we can do the same calculations when the block rotates around B and hits the ground at A .

Remark 5. *As we shall see in section 5, rocking may be approximated for non zero $e_{n,1}$. Then one does not get perfect rocking, a small rebound phase exists after the impacting corner has hit the ground. This is important because the reported values for the kinematic restitution coefficients for steel/steel [29] or blue granite/blue granite [45] systems, are around 0.9, which is quite far from zero. See section 5 and section 6.*

2.3.2 Diagonal \mathcal{E}_n , $p_{n,1}(t) \neq 0$, $p_{n,2}(t) \neq 0$ (sliding rocking block)

Let us now relax the assumption that $p_{n,2}(t) = 0$. The impact dynamics is:

$$\begin{cases} m\dot{x}(t^+) = \dot{x}(t^-) \\ m(\dot{y}(t^+) - \dot{y}(t^-)) = p_{n,1}(t) + p_{n,2}(t) \\ I_G(\dot{\theta}(t^+) - \dot{\theta}(t^-)) = \frac{L}{2}(p_{n,1}(t) - p_{n,2}(t)) \\ \dot{q}_{\text{norm},1}(t^+) = -e_{n,1}\dot{q}_{\text{norm},1}(t^-) \\ \dot{q}_{\text{norm},2}(t^+) = 0 \end{cases} \quad (17)$$

Doing similar calculations as above one deduces that $\dot{\theta}(t^+) = 0$ and $\dot{y}(t^+) = 0$ because for rocking to occur $e_{n,1} = 0$. One finds $p_{n,1}(t) = -\left(\frac{mL}{4} + \frac{I_G}{L}\right)\dot{\theta}(t^-) \geq 0$, and $p_{n,2}(t) = m\left(\frac{l^2 - 2L^2}{12L}\right)\dot{\theta}(t^-)$. Thus $p_{n,2}(t) \geq 0$ if and only if $l^2 \leq 2L^2$ (the kinetic angle at $\theta = 0$ is less than or equal to $\frac{\pi}{2}$). This means that according to this model, both percussions are non-zero while the block is in a motion like (ii) above, only if the block is of the flat type.

2.3.3 General \mathcal{E}_n , $p_{n,1}(t) \neq 0$, $p_{n,2}(t) \neq 0$ (sliding rocking block)

One concludes that the kinematic model of restitution with a diagonal \mathcal{E}_n is a quite poor model that allows one to cover only very few cases of rock motion. In order to enlarge the set of reachable post-impact velocities, let us investigate a more general impact law. In particular we may set \mathcal{E}_n with off-diagonal elements, *i.e.* we introduce couplings between the two normal directions at the impact times. Let us set $\mathcal{E}_n = \begin{pmatrix} e_{n,1} & e_{n,12} \\ e_{n,21} & e_{n,2} \end{pmatrix}$. The impact dynamics is:

$$\begin{cases} m\dot{x}(t^+) = m\dot{x}(t^-) \\ m(\dot{y}(t^+) - \dot{y}(t^-)) = p_{n,1}(t) + p_{n,2}(t) \\ I_G(\dot{\theta}(t^+) - \dot{\theta}(t^-)) = \frac{L}{2}(p_{n,1}(t) - p_{n,2}(t)) \\ \dot{q}_{\text{norm},1}(t^+) = -e_{n,1}\dot{q}_{\text{norm},1}(t^-) - e_{n,12}\dot{q}_{\text{norm},2}(t^-) \\ \dot{q}_{\text{norm},2}(t^+) = -e_{n,21}\dot{q}_{\text{norm},1}(t^-) - e_{n,2}\dot{q}_{\text{norm},2}(t^-) \end{cases} \quad (18)$$

From the fact that $\dot{q}_{\text{norm},1}(t^+) = \dot{q}_{\text{norm},2}(t^-) = 0$ we obtain $\dot{y}(t^-) = \frac{L}{2}\dot{\theta}(t^-)$ and $\dot{y}(t^+) = -\frac{L}{2}\dot{\theta}(t^+)$. After some calculations one gets $p_{n,1}(t) = -\left(\frac{mL}{4} + \frac{I_G}{L}\right)e_{n,21}\dot{\theta}(t^-) - \frac{m}{2}\dot{y}(t^-) - \frac{I_G}{L}\dot{\theta}(t^-) \geq 0$ since $\dot{\theta}(t^-) < 0$. Also $p_{n,2}(t) = \left(-\frac{mL}{2} + (e_{n,21} + 1)\frac{I_G}{L}\right)\dot{\theta}(t^-)$. The kinetic constraint $p_{n,2}(t) \geq 0$ implies that $l \leq \sqrt{\frac{5-e_{n,21}}{1+e_{n,21}}}L$ or equivalently $e_{n,21} \leq \frac{5L^2-l^2}{l^2+L^2}$. Recalling that $e_{n,1} = 0$ the energetic constraint implies that $e_{n,21} \in [-1, 1]$ and the kinematic constraint $\dot{q}_{\text{norm},2}(t^+) \geq 0$ implies $e_{n,21} \geq 0$, therefore $e_{n,21} \in [0, 1]$. We deduce that the kinematic, kinetic and energetic constraints imply that $e_{n,21} \in [0, \min(\frac{5L^2-l^2}{l^2+L^2}, 1)]$ if $\sqrt{5}L \geq l$. Otherwise there is no suitable restitution coefficient that allows one to model the rocking motion. This means that rocking is possible in the class of flat rocks (with $0 < l < \sqrt{2}L$) and of slender rocks with $\sqrt{2}L \leq l \leq \sqrt{5}L$. One has $\dot{\theta}(t^+) = e_{n,21}\dot{\theta}(t^-) \leq 0$ and $\dot{y}(t^+) = -\frac{e_{n,21}L}{2}\dot{\theta}(t^-) \geq 0$. Notice that in the limit $l = \sqrt{5}L$ then $e_{n,21} = 0$ and therefore $\dot{\theta}(t^+) = 0$ and $\dot{y}(t^+) = 0$. The admissible domain for $e_{n,21}$ is depicted in figure 2.

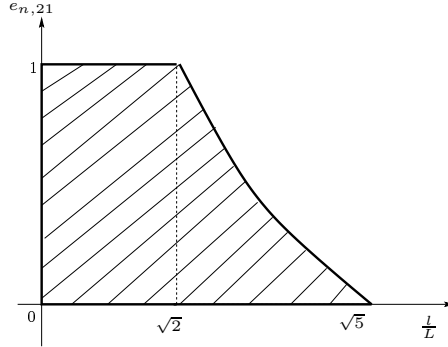


Figure 2: The admissible domain for $e_{n,21}$.

Remark 6. *The introduction of coupling terms in \mathcal{E}_n allows one to cover a larger set of the rocking motion. It has already been noticed elsewhere that one needs to introduce “distance” effects in order to solve multiple impact problems in chains of balls [20].*

Remark 7. *Depending on the type of motion (i.e. on the type of kinematic constraint that is imposed on the block), the energetic constraint may imply different bounds on the entries of \mathcal{E}_n . Indeed the energetic inequality $\mathcal{E}_n^T \mathcal{E}_n - I_m \leq 0$ defines a subset in the set of restitution coefficients (the entries of \mathcal{E}_n). The other constraints define sections of this subset.*

2.3.4 General \mathcal{E}_n , $p_{n,1}(t) \neq 0$, $p_{n,2}(t) \neq 0$ (sticking rocking block)

The kinematic constraints due to the sticking points (A sticks before the shock, B sticks after it) are given by $\dot{x}(t^-) = -\frac{l}{2}\dot{\theta}(t^-)$ and $\dot{q}_{\text{norm},2}(t^-) = \dot{y}(t^-) - \frac{L}{2}\dot{\theta}(t^-) = 0$. The point B is fixed in both directions after the shock, i.e. $\dot{x}(t^+) = -\frac{l}{2}\dot{\theta}(t^+)$ and $\dot{q}_{\text{norm},1}(t^+) = \dot{y}(t^+) + \frac{L}{2}\dot{\theta}(t^+) = 0$. The impact dynamics is as in (18) except for the first line for \dot{x} since \dot{x} may jump at the impact, see (26)

and remark 9. It is noteworthy that imposing *a priori* all the above kinematic constraints, imposes a very particular form of the percussion vector, see (26). One obtains $\dot{\theta}(t^+) = e_{n,21}\dot{\theta}(t^-)$, and since we deal with rocking $e_{n,21} > 0$. The kinetic constraint $p_{n,1}(t) \geq 0$ is always satisfied and $p_{n,2}(t) \geq 0$ if and only if $e_{n,21} \geq \frac{l^2 - 2L^2}{4L^2 + l^2}$. Therefore $e_{n,21} \geq \max\left(0, \frac{l^2 - 2L^2}{4L^2 + l^2}\right)$. The energetic constraint implies $e_{n,21} \in [-1, 1]$, which is always satisfied for this value of $e_{n,21}$. So we infer that $e_{n,21} \in [\max\left(0, \frac{l^2 - 2L^2}{4L^2 + l^2}\right), 1]$, as depicted in figure 3. Recall also that $e_{n,1} = 0$.

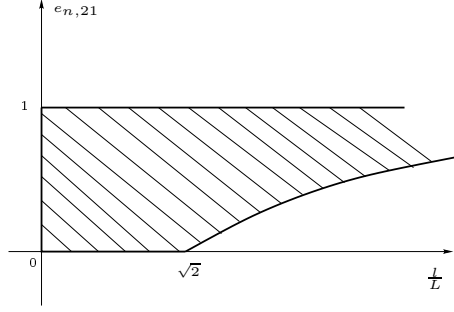


Figure 3: The admissible domain for $e_{n,21}$.

Let us comment that if \mathcal{E}_n is diagonal then one obtains that $e_{n,1} = 0$, $\dot{q}_{\text{norm},2}(t^+) = 0$ (since $\dot{q}_{\text{norm},2}(t^+) = -e_{n,2}\dot{q}_{\text{norm},2}(t^-)$ and $\dot{q}_{\text{norm},2}(t^-) = 0$), so that $\dot{y}(t^+) = \frac{L}{2}\dot{\theta}(t^+)$. This with $\dot{q}_{\text{norm},1}(t^+) = \dot{y}(t^+) + \frac{L}{2}\dot{\theta}(t^+) = 0$ implies that $\dot{y}(t^+) = \dot{\theta}(t^+) = 0$: only the most dissipative case is handled.

2.3.5 Diagonal \mathcal{E}_n , $p_{n,1}(t) \neq 0$, $p_{n,2}(t) \neq 0$ (half-rocking block)

We now turn our attention to the half-rocking motion problem. A stays in contact while B collides the ground and rebounds. The kinematic constraints are $f_2(q(t)) = 0$ and $\dot{y}(t) + \frac{l}{2}\dot{\theta}(t)\sin(\theta(t)) - \frac{L}{2}\dot{\theta}(t)\cos(\theta(t)) = 0$ for all t . The post- and pre-impact constraints are thus (at a double-impact time $\theta(t) = 0$): $\dot{y}(t^+) = \frac{L}{2}\dot{\theta}(t^+)$ and $\dot{y}(t^-) = \frac{L}{2}\dot{\theta}(t^-)$. The impact at B means that $\dot{q}_{\text{norm},1}(t^+) = -e_{n,1}\dot{q}_{\text{norm},1}(t^-)$ with $\dot{q}_{\text{norm},1}(t^-) < 0$ and $\dot{q}_{\text{norm},1}(t^+) \geq 0$. Combining all these equalities we obtain $\dot{\theta}(t^+) = -e_{n,1}\dot{\theta}(t^-)$ and consequently $\dot{y}(t^+) = -e_{n,1}\dot{y}(t^-)$. Let us now use the impact dynamics in (11). Simple calculations yield:

$$\begin{cases} p_{n,1}(t) = -\frac{m}{12L}(e_{n,1} + 1)\dot{\theta}(t^-)(4L^2 + l^2) \\ p_{n,2}(t) = \frac{m}{12L}(e_{n,1} + 1)\dot{\theta}(t^-)(l^2 - 2L^2) \end{cases} \quad (19)$$

Therefore $p_{n,1}(t) \geq 0$ always, whereas $p_{n,2}(t) \geq 0 \Leftrightarrow l^2 \leq 2L^2$. We retrieve again that only flat block ($\theta_{12} \leq \frac{\pi}{2}$) can be modeled, as in section 2.3.2.

The case where one assumes $p_{n,2}(t) = 0$ (the contact force at A remains a function of time) yields that necessarily $l^2 = 2L^2$ so that only $\theta_{12} = \frac{\pi}{2}$ can be treated. Finally assuming a general restitution matrix \mathcal{E}_n as in (18) yields since $\dot{q}_{\text{norm},2}(t^-) = 0$ and $\dot{q}_{\text{norm},2}(t^+) = 0$ that $e_{n,21} = 0$, so nothing is brought in the model compared to the diagonal restitution matrix case.

2.3.6 Diagonal \mathcal{E}_n , $p_{n,1}(t) \neq 0$, $p_{n,2}(t) \neq 0$, with Coulomb's friction

Let us now try to model Coulomb's friction at A and B , by setting at each of these point $p_{t,i}(t) \in -\mu p_{n,i}(t) \operatorname{sgn}(v_{t,i}(t^+))$, where $v_{t,1} = \dot{x} + \frac{\dot{\theta}}{2}(l \cos(\theta) - L \sin(\theta))$, $v_{t,2} = \dot{x} + \frac{\dot{\theta}}{2}(l \cos(\theta) + L \sin(\theta))$ are the tangential velocities at B and A (when contact is established at these points), and $\mu \geq 0$ is a friction coefficient, $\operatorname{sgn}(\cdot)$ is the multivalued at zero signum function. It is common in impact mechanics to introduce Coulomb's friction at the impulse level, but this may yield an energetically inconsistent model when coupled with a kinematic restitution coefficient [10, 13]. Introducing $\lambda_{t,1}$ and $\lambda_{t,2}$ the tangential reactions at B and A respectively, and the corresponding tangential impulses $p_{t,1}$ and $p_{t,2}$, the impact dynamics becomes:

$$\begin{cases} m(\dot{x}(t^+) - \dot{x}(t^-)) = p_{t,1}(t) + p_{t,2}(t) \\ m(\dot{y}(t^+) - \dot{y}(t^-)) = p_{n,1}(t) + p_{n,2}(t) \\ I_G(\dot{\theta}(t^+) - \dot{\theta}(t^-)) = \frac{L}{2}(p_{n,1}(t) - p_{n,2}(t)) + l(p_{t,1}(t) + p_{t,2}(t)) \\ p_{t,i}(t) \in -\mu p_{n,i}(t) \operatorname{sgn}(v_{t,i}(t^+)), i = 1, 2 \\ \dot{q}_{\text{norm},1}(t^+) = -e_{n,1} \dot{q}_{\text{norm},1}(t^-) \\ \dot{q}_{\text{norm},2}(t^+) = -e_{n,2} \dot{q}_{\text{norm},2}(t^-) \end{cases} \quad (20)$$

Before the impact A is sticking so $\dot{q}_{\text{norm},2}(t^-) = 0$ and $\dot{q}_{\text{norm},2}(t^+) = 0$. Thus $\dot{y}(t^-) = \frac{L}{2}\dot{\theta}(t^-)$ and $\dot{y}(t^+) = \frac{L}{2}\dot{\theta}(t^+)$. Therefore rocking is still impossible because the friction cannot help in making A detach from the ground after the shock. At best this model may describe half-rocking motion.

2.4 The angular velocity restitution law

Let us now start from the restitution law

$$\dot{\theta}(t^+) = -r\dot{\theta}(t^-) \quad (21)$$

(without considering it as a consequence of the above generalized kinematic law) and examine the consequences of rocking motion. First of all it has to be remarked that the kinematic restitution law in (21) is not associated with the unilateral constraints in (1) (or equivalently (2)), except if y is a constant in which case it makes perfect mechanical sense because $\nabla f_i^T(q)\dot{q} = \dot{\theta}$. However in general y is not constant and one may suspect that the impact law (21) may yield mechanical inconsistencies. Let us examine this in more details.

2.4.1 Sliding rocking block

Let us consider first the rocking case (ii) above: the block rotates around A , then hits the ground at B and starts rotating around B while A detaches from the constraint boundary. From (11) we deduce at the impact time ($\theta(t) = 0$):

$$\begin{cases} m(\dot{y}(t^+) - \dot{y}(t^-)) = p_{n,1} + p_{n,2} \\ I_G(\dot{\theta}(t^+) - \dot{\theta}(t^-)) = \frac{L}{2}(p_{n,1} - p_{n,2}) \\ \dot{q}_{\text{norm},1}(t^+) = \dot{y}(t^+) + \frac{L}{2}\dot{\theta}(t^+) = 0 \\ \dot{q}_{\text{norm},2}(t^-) = \dot{y}(t^-) - \frac{L}{2}\dot{\theta}(t^-) = 0 \end{cases} \quad (22)$$

The loss of kinetic energy at the impact is found to be equal to $T_L(t) = \frac{1}{2} \left(\frac{mL^2}{4} + I_G \right) (r^2 - 1) \dot{\theta}^2(t^-)$ so that $r \in [-1, 1]$ from the energetic constraint. Since we examine the rocking motion we have $\text{sgn}(\dot{\theta}(t^-)) = \text{sgn}(\dot{\theta}(t^+))$ so that $r \leq 0$, hence $r \in [-1, 0]$. From (22) one computes that

$$\begin{cases} p_{n,1}(t) = \left(\frac{mL}{4}r - \frac{2I_G}{L} \right) \dot{\theta}(t^-) - \frac{m}{2}\dot{y}(t^-) \\ p_{n,2}(t) = \left(\frac{mL}{4}r + \frac{2I_G}{L} \right) \dot{\theta}(t^-) - \frac{m}{2}\dot{y}(t^-) \end{cases} \quad (23)$$

In order to respect the kinetic constraint $p_{n,1}(t) \geq 0$ one has to have from (23) (recall that $I_G = \frac{m}{12}(l^2 + L^2)$):

$$r \leq \frac{l^2 + L^2 + 6L \frac{\dot{y}(t^-)}{\dot{\theta}(t^-)}}{2L^2 - l^2} = \frac{l^2 + 4L^2}{2L^2 - l^2} (> 0) \quad (24)$$

if $2L^2 - l^2 > 0$, and

$$r \geq \frac{l^2 + L^2 + 6L \frac{\dot{y}(t^-)}{\dot{\theta}(t^-)}}{2L^2 - l^2} = \frac{l^2 + 4L^2}{2L^2 - l^2} (< 0) \quad (25)$$

if $2L^2 - l^2 < 0$ (slender block), and recalling that $\dot{\theta}(t^-) < 0$, $\dot{y}(t^-) < 0$, $\dot{y}(t^-) = \frac{l}{2}\dot{\theta}(t^-)$. Both these upper-bounds are respected for $r \in [-1, 0]$, so that the first kinetic constraint is satisfied for $r \in [-1, 0]$. Let us now examine $p_{n,2}(t) \geq 0$. From (23) one has $p_{n,2}(t) = m \left(\frac{3L^2r + 2l^2 - L^2}{12L} \right) \dot{\theta}(t^-)$. It follows that $p_{n,2}(t) \geq 0 \Leftrightarrow r \leq \frac{L^2 - 2l^2}{3L^2}$. So if $l > \sqrt{2}L$ (slender block) one obtains $r < -1$ which is not possible from the energetic constraint. It is therefore necessary that $\frac{1}{\sqrt{2}}L < l < \sqrt{2}L$ so that $p_{n,2}(t) \geq 0$ and the energetic constraint is satisfied. We conclude that $r \in [-1, \min\left(0, \frac{L^2 - 2l^2}{3L^2}\right)]$ and that $\frac{1}{\sqrt{2}}L < l < \sqrt{2}L$. We therefore reach a similar conclusion to the one obtained with the generalized kinematic law and $p_{n,2}(t) \neq 0$ in section 2.3.3, that rocking can be described for this model only for a subclass of flat blocks. In figure 4 is depicted r as a function of $\frac{l}{L}$. Notice that $\dot{q}_{\text{norm},2}(t^+) = r\dot{q}_{\text{norm},1}(t^-)$, so $r = -e_{n,21}$: the angular coefficient of restitution adds a coupling in the matrix \mathcal{E}_n .

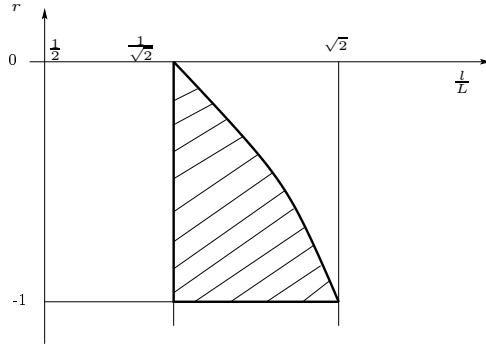


Figure 4: The admissible domain for r .

Finally it is easily computed that if $p_{n,2}(t) = 0$ then $p_{n,1}(t) = \frac{mL}{2}(r - 1)\dot{\theta}(t^-) = -\frac{2I_G}{L}(r + 1)\dot{\theta}(t^-)$, which yields $r = \frac{2L^2 - l^2}{4L^2 + l^2}$. We recover here the

value of r in (16) that was obtained with the generalized kinematic law, and with the assumption that $p_{n,2}(t) = 0$. Therefore if $l < \sqrt{2}L$ then $r > 0$ and $\text{sgn}(\dot{\theta}(t^+)) = -\text{sgn}(\dot{\theta}(t^-))$. It is not possible that the block sticks at B after the shock for rocking. Thus with these assumptions rocking cannot be modeled if $l < \sqrt{2}L$. Now if $r = \sqrt{2}L$ then $r = 0$ and the block stops after the shock since $\dot{\theta}(t^+) = 0$. Finally if $l > \sqrt{2}L$ then $r < 0$ and $\text{sgn}(\dot{\theta}(t^+)) = \text{sgn}(\dot{\theta}(t^-)) = -1$. The block can stick at B . One obtains $\dot{y}(t^+) = \frac{L}{2} \frac{2L^2 - l^2}{4L^2 + l^2} \dot{\theta}(t^-) > 0$. The energetic constraint implies that $r \in [-1, 1]$, so in this last case $r \in [-1, 0)$. This implies in turn that $l^2 - 1 \leq 2L^2 < l^2$. The admissible domain in the (l, L) plane is depicted in figure 5.

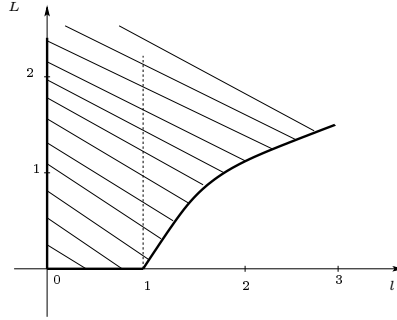


Figure 5: The admissible domain for l and L .

Remark 8. *From the results of this section and of section 2.3.3, it follows that both approaches to describe the rocking motion are quite close one to each other. The generalized kinematic restitution law of J.J. Moreau [10, 21] is unable to model rocking, which has led Moreau to introduce an ad hoc tangential coefficient at the local contact velocities level [40]. The introduction of a non-diagonal \mathcal{E}_n is quite similar.*

2.4.2 Sticking free-rocking block

In many papers r is calculated by equaling the moment of momentum at the rotating point, before and after the impact. Then one finds $r = -\frac{2l^2 - L^2}{2L^2 + 2l^2} = -(1 - \frac{3}{2} \sin^2(\alpha))$ [23, 29], where α is as in figure 1. We may name this r the Housner model. Notice that if we suppose that the problem is frictionless then $\dot{x} = 0$ and x is constant for zero initial data. The moment of momentum at B when free rocking occurs with rotation around A and collision at B , is equal to

$$\sigma_B = \begin{pmatrix} 0 \\ 0 \\ I_G \dot{\theta} \end{pmatrix} + m \begin{pmatrix} -\frac{L}{2} \\ \frac{l}{2} \\ 0 \end{pmatrix} \times \begin{pmatrix} \dot{x} \\ \dot{y} \\ 0 \end{pmatrix}, \text{ so } \sigma_B = I_G \dot{\theta} - m \frac{L}{2} \dot{y} - m \frac{l}{2} \dot{x}. \text{ Thus}$$

taking into account the kinematic constraints $\dot{y}(t^-) = \frac{L}{2} \dot{\theta}(t^-)$ and $\dot{y}(t^+) = -\frac{L}{2} \dot{\theta}(t^+)$, one finds that $\sigma_B(t^+) = \sigma_B(t^-)$ gives $r = \frac{2L^2 - l^2}{4L^2 + l^2}$. This indeed agrees with (16), but not with the above value $r = -\frac{2l^2 - L^2}{2L^2 + 2l^2}$ that is used in the literature, which is found by assuming another kinematic constraint: the contact points do not slip. This is in fact a very approximate way of introducing friction

that is responsible for stick/slip behavior, and may explain why this r is often found not to match with the one from experimental results.

Let us now analyze the free-rocking motion where the contact points stick. The kinematic constraints are as in section 2.3.4: $\dot{x}(t^-) = -\frac{l}{2}\dot{\theta}(t^-)$, $\dot{y}(t^-) - \frac{L}{2}\dot{\theta}(t^-) = 0$, $\dot{x}(t^+) = -\frac{l}{2}\dot{\theta}(t^+)$ and $\dot{y}(t^+) + \frac{L}{2}\dot{\theta}(t^+) = 0$. From (11) the impact dynamics is given by:

$$\begin{cases} m(\dot{x}(t^+) - \dot{x}(t^-)) = \frac{mL}{4I_G + ml^2}(p_{n,2}(t) - p_{n,1}(t)) = p_{t,1}(t) + p_{t,2}(t) \\ m(\dot{y}(t^+) - \dot{y}(t^-)) = p_{n,1}(t) + p_{n,2}(t) \\ I_G(\dot{\theta}(t^+) - \dot{\theta}(t^-)) = \frac{L}{2}(p_{n,1}(t) - p_{n,2}(t)) + \frac{l}{2}(p_{t,1} + p_{t,2}) \\ \dot{\theta}(t^+) = -r\dot{\theta}(t^-), \quad r = -\frac{2l^2 - L^2}{2L^2 + 2l^2} \end{cases} \quad (26)$$

One has $T_L(t) = T(t^+) - T(t^-) = \left(\frac{m}{8}(l^2 + L^2) + \frac{I_G}{2}\right)(r^2 - 1)\dot{\theta}^2(t^-)$ so that $T_L(t^-) \leq 0 \Leftrightarrow r \in [-1, 1]$. Note at once that such an r satisfies the energetic constraint $r \in [-1, 1]$. One finds after calculations $p_{n,1}(t) = \left(\frac{mL}{4}(r - 1) - \frac{4I_G + ml^2}{4L}\right)\dot{\theta}(t^-)$, and $p_{n,2}(t) = \left(\frac{mL}{4}(r - 1) + \frac{4I_G + ml^2}{4L}(r + 1)\right)\dot{\theta}(t^-)$. Therefore $p_{n,1}(t) \geq 0$ since $r \in [-1, 1]$ (the energetic constraint), and $p_{n,2}(t) \geq 0$ if and only if $r \leq \frac{L^2 + 2l^2}{2(L^2 + l^2)}$, which is precisely the value of r in (26) that is ≤ 1 . Thus $p_{n,2}(t) \geq 0$ if and only if $r \in [-1, \frac{L^2 + 2l^2}{2(L^2 + l^2)}]$. Recall now that rocking occurs only if both $\dot{\theta}(-)$ and $\dot{\theta}(+)$ have the same sign, *i.e.* $r < 0$, so that $l \geq \frac{1}{\sqrt{2}}L$. This gives an r in (26) that satisfies the kinetic, the energetic, and the kinematic constraints. This encompasses a subclass of flat blocks ($\frac{1}{\sqrt{2}}L \leq l < \sqrt{2}l$) and slender blocks ($l > \sqrt{2}L$).

One sees that $e_{n,21}$ in section 2.3.4 satisfies $e_{n,21} = -r$ since $\dot{\theta}(t^+) = e_{n,21}\dot{\theta}(t^-)$. However the moment of momentum equality $\sigma_B(t^+) = \sigma_B(t^-)$ is not used in section 2.3.4. This provides more freedom for the choice of $e_{n,21}$. The moment of momentum equality imposes a constraint on r and hence a particular energetic behavior at the impact. Indeed the kinetic energy loss is equal to $T_L(t) = \frac{1}{2}\left(\frac{l^2 + L^2}{4} + I_G\right)(r^2 - 1)(\dot{\theta}(t^-))^2$. The value of r in (26) gives:

$$T_L(t) = -\frac{3L^2}{4}\frac{L^2 + 4l^2}{2l^2 + 2L^2}\left(\frac{m}{8}(l^2 + L^2) + \frac{I_G}{2}\right)(\dot{\theta}(t^-))^2 \quad (27)$$

that is always negative. The restitution law of section 2.3.4 allows for $e_{n,21} \in [0, 1]$ if $l \leq \sqrt{2}L$ and $e_{n,21} \in [\frac{l^2 - 2L^2}{4L^2 + l^2}, 1]$ if $l \geq \sqrt{2}L$, and hence allows to describe more energetic behaviors.

Remark 9. *The sticking assumption introduces a jump in \dot{x} and hence in \dot{q}_{tan} (indeed from the kinematic constraints one has $\dot{x}(t^+) = -r\dot{x}(t^-)$ and $\dot{q}_{\text{tan}} = \sqrt{m}\dot{x}$) and modifies the impulse form. Hence it corresponds to some general restitution matrix \mathcal{E} as in (10) with discontinuous \dot{q}_{tan} . Taking into account that we may redo the same analysis when the block rotates around B and hits the ground at A to describe the rocking over a complete cycle, we obtain that*

$$\mathcal{E} = \begin{pmatrix} 0 & -r & 0 \\ -r & 0 & 0 \\ 0 & 0 & r \end{pmatrix}, \quad \text{with } \mathcal{E}^T \mathcal{E} = \text{diag}(r^2). \quad \text{In the case of the restitution law}$$

of section 2.3.4 one obtains $\mathcal{E} = \begin{pmatrix} 0 & e_{n,21} & 0 \\ e_{n,21} & 0 & 0 \\ 0 & 0 & -e_{n,21} \end{pmatrix}$ if one imposes the same coefficient for the two sub-cycles of the rocking motion, i.e. $e_{n,12} = e_{n,21}$.

Remark 10. *The physical phenomenon that is responsible for sticking of the contact points is Coulomb's friction. Thus the sticking free-rocking motion should not be postulated a priori, but should be the result of the effects of Coulomb's friction. This is what the impact model that is used in sections 4 to 7 allows one to do.*

Let us now study the angular velocity restitution for sticking free-rocking, and assuming that $\lambda_{n,2}$ is a function (there is no Dirac measure acting at A when the block collides at B). Imposing $p_{n,2}(t) = 0$ in (26) yields $r = \frac{2L^2 - l^2}{4L^2 + l^2}$. The moment of momentum equality yields $r = \frac{L^2 - 2L^2}{2L^2 + 2L^2}$. Let $\alpha = \frac{l^2}{L^2}$. We get that necessarily $\frac{2-\alpha}{4+\alpha} = \frac{1-2\alpha}{2+2\alpha} \Rightarrow \alpha = 0$. We conclude that this works only in the limit case of a block with $l = 0$, that is a rod with zero width with $\theta_{12} = \frac{3\pi}{4}$ and $r = \frac{1}{2}$. However since rocking implies that $r < 0$ we infer that sticking free-rocking cannot be handled with $p_{n,2}(t) = 0$.

2.4.3 Half-rocking block

The half-rocking implies $r > 0$ (the angular velocity reverses its sign after the impact at B), while $\dot{q}_{\text{norm},2}(t^-) = \dot{q}_{\text{norm},2}(t^+) = 0$, i.e. $\dot{y}(t^+) = \frac{L}{2}\dot{\theta}(t^+)$ and $\dot{y}(t^-) = \frac{L}{2}\dot{\theta}(t^-)$. The impact dynamics is thus rewritten as:

$$\begin{cases} \frac{mL}{2}(\dot{\theta}(t^+) - \dot{\theta}(t^-)) = p_{n,1}(t) + p_{n,2}(t) \\ \frac{2I_G}{L}(\dot{\theta}(t^+) - \dot{\theta}(t^-)) = p_{n,1}(t) - p_{n,2}(t) \end{cases} \quad (28)$$

It follows that $p_{n,1}(t) = -(r+1)(\frac{mL}{2} + \frac{2I_G}{L})\dot{\theta}(t^-)$ that is always positive, while $p_{n,2}(t) = (r+1)(-\frac{mL}{2} + \frac{2I_G}{L})\dot{\theta}(t^-)$. The energetic constraint implies $r \in [-1, 1]$. Therefore $p_{n,2}(t) \geq 0$ if and only if $-\frac{mL}{2} + \frac{2I_G}{L} > 0$ and $r = 1$ or $-\frac{mL}{2} + \frac{2I_G}{L} < 0$ and $r = -1$, which is not possible since $r > 0$. Thus this is equivalent to $l > \sqrt{2}L$ and $r = 1$.

Finally assuming that $p_{n,2}(t) = 0$ one finds that $\frac{mL}{2}(\dot{\theta}(t^+) - \dot{\theta}(t^-)) = p_{n,1}(t) = \frac{2I_G}{L}(\dot{\theta}(t^+) - \dot{\theta}(t^-))$ so that $\frac{mL}{2} = \frac{2I_G}{L}$ which is equivalent to $l = \sqrt{2}L$, i.e. $\theta_{12} = \frac{\pi}{2}$. Half-rocking implies $r > 0$ which together with the energetic constraint implies that $r \in [0, 1]$.

2.5 Characteristic kinetic angles

Several kinetic angle appeared in the foregoing calculations, that correspond at $\theta = 0$ to a) $l = \sqrt{5}L$ (section 2.3.3), b) $l = \frac{1}{\sqrt{2}}L$, c) $l = \sqrt{2L^2 + 1}$ (section 2.4). They are given by $\theta_{12} = \pi - \arccos \frac{l^2 - 2L^2}{4L^2 + l^2}$, see section 2.2 for the general formula. One therefore gets a) $\alpha \triangleq \pi - \arccos(\frac{1}{3}) > \frac{\pi}{2}$, b) $\gamma \triangleq \pi - \arccos(-\frac{1}{3}) < \frac{\pi}{2}$, c) $\beta \triangleq \pi - \arccos(\frac{1}{6L^2 + 1}) > \frac{\pi}{2}$, respectively.

2.6 General \mathcal{E}_n , $p_{n,1}(t) \neq 0$, $p_{n,2}(t) \neq 0$, rebound at B

Let us now study the case when the block rotates around A and sticks in the tangential direction, hits the ground at B , and we allow for $e_{n,1} > 0$, *i.e.* a positive restitution coefficient at B . This may be motivated by the fact that in most of the reported experiments, rocking occurs while $e_{n,i} \neq 0$, see remark 5. As will be shown the uniqueness of the restitution parameters (coefficients) may be lost for a given energetic behaviour. The kinematic constraints at A are $\dot{x}(t^-) = -\frac{l}{2}\dot{\theta}(t^-)$, $\dot{q}_{\text{norm},2}(t^-) = \dot{y}(t^-) - \frac{L}{2}\dot{\theta}(t^-) = 0$. The restitution law is $\dot{q}_{\text{norm}}(t^+) = -\mathcal{E}_n\dot{q}_{\text{norm}}(t^-)$, which gives $\dot{q}_{\text{norm},1}(t^+) = -e_{n,1}\dot{q}_{\text{norm},1}(t^-) - e_{n,12}\dot{q}_{\text{norm},2}(t^-) = -e_{n,1}\dot{q}_{\text{norm},1}(t^-)$, and $\dot{q}_{\text{norm},2}(t^+) = -e_{n,21}\dot{q}_{\text{norm},1}(t^-) - e_{n,2}\dot{q}_{\text{norm},2}(t^-) = -e_{n,21}\dot{q}_{\text{norm},1}(t^-)$. The impact dynamics is given by:

$$\begin{cases} m(\dot{x}(t^+) - \dot{x}(t^-)) = p_{t,1} + p_{t,2} \\ m(\dot{y}(t^+) - \dot{y}(t^-)) = p_{n,1} + p_{n,2} \\ I_G(\dot{\theta}(t^+) - \dot{\theta}(t^-)) = \frac{l}{2}(p_{n,1} - p_{n,2}) + \frac{l}{2}(p_{t,1} + p_{t,2}) \end{cases} \quad (29)$$

For the moment we have 6 unknowns and only 5 equations. A sixth equation is added by defining $\dot{x}(t^+) = -e_{n,3}\dot{x}(t^-) \Leftrightarrow \dot{q}_{\text{tan}}(t^+) = -e_{n,3}\dot{q}_{\text{tan}}(t^-)$ since $\dot{q}_{\text{tan}} = \sqrt{m}\dot{x}$. Combining the kinematic constraints and the impact dynamics together with the restitution law one obtains the following:

$$\begin{cases} \dot{x}(t^+) = -e_{n,3}\dot{x}(t^-) \\ \dot{y}(t^+) = -\frac{1}{2}(e_{n,1} + e_{n,21})L\dot{\theta}(t^-) \\ \dot{\theta}(t^+) = (-e_{n,1} + e_{n,21})\dot{\theta}(t^-) \end{cases} \quad (30)$$

After some calculations the kinetic energy loss is given by:

$$\begin{aligned} T_L(t) &= \frac{m}{8} \left[l^2(e_{n,3}^2 - 1) + L^2(e_{n,1} + e_{n,21})^2 - L^2 + \frac{l^2+L^2}{3}((-e_{n,1} + e_{n,21})^2 - 1) \right] \dot{\theta}^2(t^-) \\ &= \frac{m}{8} \dot{\theta}^2(t^-) \left[-\frac{4l^2+4L^2}{3} + l^2e_{n,3}^2 + L^2(e_{n,1} + e_{n,21})^2 + \frac{l^2+L^2}{3}(-e_{n,1} + e_{n,21})^2 \right] \end{aligned} \quad (31)$$

from which it follows that $T_L \leq 0$ is equivalent to:

$$(l^2 + 4L^2)(e_{n,1}^2 + e_{n,21}^2) + (4L^2 - 2l^2)e_{n,1}e_{n,21} + 3l^2e_{n,3}^2 \leq 4(l^2 + L^2) \quad (32)$$

Defining $e_1 \triangleq e_{n,1} + e_{n,21}$, $e_2 \triangleq e_{n,21} - e_{n,1}$, $e_3 \triangleq e_{n,3}$, one finds equivalently:

$$L^2e_1^2 + \frac{l^2 + L^2}{3}e_2^2 + l^2e_3^2 \leq \frac{4}{3}(l^2 + L^2) \quad (33)$$

Clearly for a given energetic behaviour (for instance the lossless case $T_L = 0$) the coefficients live on an ellipsoid \mathcal{S}_e , and are non-unique. This was already known for chains of balls [10] but is shown here for the block for the first time. One has $p_{n,1}(t) + p_{n,2}(t) = -\frac{mL}{2}(e_{n,1} + e_{n,21} + 1)\dot{\theta}(t^-)$, and $p_{n,1}(t) - p_{n,2}(t) = \left[\frac{2lG}{L}(e_{n,1} - e_{n,21} + 1) - \frac{ml^2}{2L}(e_{n,3} + 1) \right] \dot{\theta}(t^-)$. Hence the kinetic constraints are given by:

$$p_{n,1}(t) \geq 0 \Leftrightarrow (l^2 + 4L^2)e_{n,1} + (2L^2 - l^2)e_{n,21} + 3l^2e_{n,3} + 7l^2 + 4L^2 \geq 0 \quad (34)$$

and

$$p_{n,2}(t) \geq 0 \Leftrightarrow (2L^2 - l^2)(e_{n,1} + e_{n,21}) - 3l^2 e_{n,3} + 2(L^2 - 2l^2) \geq 0. \quad (35)$$

These two constraints define two subspaces \mathcal{S}_1 and \mathcal{S}_2 of the three-dimensional space of the restitution coefficients, and the admissible coefficients must lie in $\mathcal{S}_e \cap \mathcal{S}_1 \cap \mathcal{S}_2$.

Tangential restitution At an impact time the tangential velocities of A and B are equal to $v_{t,i} = \dot{x} + \frac{l}{2}\dot{\theta}$. Inserting the above results $v_{t,i}(t^+) = -e_{n,3}\dot{x}(t^-) + \frac{l}{2}(-e_{n,1} + e_{n,21})\dot{\theta}(t^-)$. Starting from $v_{t,i}(t^+) = e_t v_{t,i}(t^-)$ for some tangential restitution coefficient one obtains $v_{t,i}(t^+) = e_t \dot{x}(t^-) + \frac{l}{2}e_t \dot{\theta}(t^-)$. The relation between the generalized and the tangential coefficients is therefore $e_t = -e_{n,3} = -e_{n,1} + e_{n,21}$. We infer that imposing a tangential restitution at the local tangential velocities of the contact points, introduces a constraint on the generalized coefficients $e_{n,1}$, $e_{n,2}$, $e_{n,21}$. The fact that there exists constraints between various kinematic restitution coefficients is known in the case of single impacts [9, 10].

Let us impose further sticking at the end of the impact at B : $v_{t,1}(t^+) = \dot{x}(t^+) + \frac{l}{2}\dot{\theta}(t^+) = 0$, so that $\dot{x}(t^+) = -\frac{l}{2}\dot{\theta}(t^+)$. This imposes that $e_t = 0$ so that $e_{n,3} = 0$ and $e_{n,1} = e_{n,21}$. Thus the restitution matrix takes the form

$$\mathcal{E} = \begin{pmatrix} e_n & e_n & 0 \\ e_n & e_n & 0 \\ 0 & 0 & 0 \end{pmatrix}.$$

If we now impose $e_{n,1} = 0$ then $e_{n,3} = -e_{n,21}$ and $\mathcal{E} = \begin{pmatrix} 0 & e_{n,21} & 0 \\ e_{n,21} & 0 & 0 \\ 0 & 0 & e_{n,21} \end{pmatrix}$.

The results in remark 9 are recovered.

2.7 Conclusions

We have examined the capabilities of a generalized restitution law, under the energetic, kinematic, and kinetic constraints. This boils down to finding \mathcal{E}_n such that, given pre-impact velocities one has:

$$\begin{cases} -\mathcal{E}_n^T \mathcal{E}_n + I_m \geq 0 \text{ (or copositive on } \mathbb{R}^m) \\ (\mathbf{n}_q(t)^T \nabla f(q(t)))^{-1} (\mathcal{E}_n + I_n) \dot{q}_{\text{norm}}(t^-) \leq 0 \\ \mathcal{E}_n \dot{q}_{\text{norm}}(t^-) \leq 0 \\ A \dot{q}_{\text{norm}}(t^-) = 0 \end{cases} \quad (36)$$

for some matrix A with entries 0 or 1. The results are recapitulated in the table 1, where the kinetic angles α , β , γ , are given in section 2.5. It is noteworthy that we have done all the calculations when the block rotates around A and collides the ground at B . By doing the reverse (impact at A and rotation around B) one infers similar values for the restitution coefficients $e_{n,2}$ and $e_{n,12}$, which we do not indicate in the table to lighten the presentation.

The value $\theta_{12} = \frac{3\pi}{4}$ corresponds to the limit case $l = 0$.

Comments: Introducing the generalized impact law defined from the configuration space normal vectors has allowed us, among other things, to give a

| Assumptions | Free-rocking (sliding) | Half-rocking (sliding) | Free-rocking (sticking) |
|--|---|--|--|
| diagonal \mathcal{E}_n $p_{n,1} \neq 0$ $p_{n,2} = 0$ | $e_{n,1} = 0$ $\theta_{12} = \frac{\pi}{2}$ $l = \sqrt{2}L$ $\dot{y}(t^+) = \dot{\theta}(t^+) = 0$ | $e_{n,1} \in [0, 1]$ $\theta_{12} = \frac{\pi}{2}$ $l = \sqrt{2}L$ | $e_{n,1} = 0$ $\dot{y}(t^+) = \dot{\theta}(t^+) = 0$ |
| diagonal \mathcal{E}_n $p_{n,1} \neq 0$ $p_{n,2} \neq 0$ | $e_{n,1} = 0$ $\theta_{12} \in [\frac{\pi}{4}, \frac{\pi}{2}]$ $l \leq \sqrt{2}L$ $\dot{y}(t^+) = \dot{\theta}(t^+) = 0$ | $e_{n,1} \in [0, 1]$ $\theta_{12} \in [\frac{\pi}{4}, \frac{\pi}{2}]$ $l \leq \sqrt{2}L$ | $e_{n,1} = 0$ $\dot{y}(t^+) = \dot{\theta}(t^+) = 0$ |
| general \mathcal{E}_n $p_{n,1} \neq 0$ $p_{n,2} \neq 0$ | $e_{n,1} = 0$ $e_{n,21} \in [0, \min(1, \frac{5L^2-l^2}{3L^2})]$ $\theta_{12} \in [\frac{\pi}{4}, \alpha]$ $\sqrt{2}L \leq l \leq \sqrt{5}L$ | $e_{n,1} \in [0, 1]$ $e_{n,21} = 0$ $\theta_{12} \in [\frac{\pi}{4}, \frac{\pi}{2}]$ $l \leq \sqrt{2}L$ | $e_{n,21} = -r \in [\max(0, \frac{l^2-2L^2}{4L^2+l^2}), 1]$ $e_{n,1} = 0$ $\theta_{12} \in [\frac{\pi}{4}, \pi)$ |
| angular restitution r $p_{n,1} \neq 0$ $p_{n,2} \neq 0$ | $r \in [-1, \min(0, \frac{L^2-2l^2}{3L^2})]$ $\theta_{12} \in [\gamma, \frac{\pi}{2}]$ $\frac{1}{\sqrt{2}}L \leq l \leq \sqrt{2}L$ | $r = 1$ $\theta_{12} \in [\frac{\pi}{2}, \pi)$ $l \geq \sqrt{2}L$ | $r = -\frac{2l^2-L^2}{2L^2+2l^2}$ $\theta_{12} \in [\gamma, \pi)$ $l \geq \frac{1}{\sqrt{2}}L$ |
| angular restitution r $p_{n,1} \neq 0$ $p_{n,2} = 0$ | $r = \frac{2L^2-l^2}{4L^2+l^2}$ $\theta_{12} \in [\frac{\pi}{2}, \beta]$ $l^2 - 1 \leq 2L^2 \leq l^2$ | $r \in [0, 1]$ $\theta_{12} = \frac{\pi}{2}$ $l = \sqrt{2}L$ | X |

Table 1: The various kinematic restitution laws.

rigorous meaning to and to extend the well-known (in the rocking block literature) Housner angular restitution coefficient (compare entries (3,3) and (4,3) in the above table). Interestingly enough the value of r obtained from the moment of momentum conservation, corresponds to the most dissipative case of the kinematic law of section 2.3.4, which we may name the *enhanced angular-velocity restitution law*. The bounds on the restitution coefficients due to the energetical constraint, depend on the type of motion (see remark 7). This may have important practical consequences, as a different restitution matrix may have to be estimated experimentally for each initial condition, similarly to the Newton's cradle [44]. Ideally one would like to work with parameters which do not depend on the type of impact one is studying. Most importantly one would like to have a model that allows to predict whether or not a particular motion will occur (will the contact points slide or stick? Will the block rock or not?), for a given set of parameters (restitution, friction, dimensions, *etc*) to be estimated through simple, independent experiments. Such questions become fundamental if one thinks of the block motion when the base is excited: depending on the magnitude and frequency of the base excitation, the block may have several types of motions (rocking, bouncing, with stick/slip behavior of the contact points), as pointed out elsewhere [29, 46, 62]. This is already true for free rocking with fixed base (experiments reported in [29] for $\frac{l}{L} = 1$ show that after the impact at B , the block may become airborne before impacting at A , while sliding occurs at B). Predicting such complex dynamics is not possible with the kinematic laws of impact which just allow one to fit *a posteriori* the parameters with the observed experiments (as done *e.g.* in [6, 30, 51, 48]), especially when friction is considered. As an example one may consider the entry (3,3) of the

above table: $e_{n,21}$ is allowed to vary within some interval which guarantees some mechanical coherence. However how can one determine if rocking with sticking contacts will exist or not and will correspond to one such restitution? This is simply impossible.

In order to circumvent such drawbacks, one has therefore to look at restitution laws defined at another level: kinetic (Poisson's laws) or energetic. In the sequel we will adopt the impact dynamics proposed in [31, 32, 71, 34], which uses energetic coefficients [61]. This will allow us, most importantly, to include frictional effects at the impacts, which seems to be a novelty in the rocking block modeling in a rigid body framework. One may include friction into the kinematic framework [2, 40], however this is not an easy modeling task, even for a single point of impact [10, 61]. Kinematic laws however possess the huge advantage of being very tractable from the numerical point of view, which is of utmost importance when the system has a large number of contacts. Both the kinematic and the energetic approaches (to be presented in the sequel) may therefore be considered as being complementary approaches rather than opposite ones.

In [6] experimental tests were done and compared to the model with angular restitution r in (21). It was found that the analytical value of $r = -\frac{2l^2-L^2}{2L^2+2l^2}$ in [6] did not match with the experimental one, despite r was measured to be constant (but should be changed for each block). Similar conclusions were drawn in [48] who found a rather big discrepancy between the analytical and the experimental values of r (the analytical one being calculated from the conservation of angular momentum before and after the shock). Usually the experimentally measured values for r are larger than the theoretically predicted ones, and many authors simply fit r with the data without questioning the model [6, 29, 48, 59, 64, 69]. Recently experimental tests on concrete blocks have shown [17] that the ratio between the measured r and the above one may be smaller or larger than one, despite it is usually smaller (see Table II in [17]), contradicting the older conclusions. These authors also showed the inability of the kinematic angular restitution law to predict the free-rocking motion (see figure 18 in [17]). This has led some researchers in the field to propose new models. Lispcombe et al. [29] calculated r by introducing the kinematic restitution and adding constraints for no slipping or unidirectional slip, and found an expression similar to the one in (15). Yilmaz et al. [67] use a generalization of Routh's approach and so-called impulse correlation ratios, without friction. They found good agreements between their simulations and their experiments. Lourenço et al. [45, 46, 50] performed lots of experiments and also proposed a new model for rocking. It is noteworthy that in their experiments Pena et al. [45] found better matching between the above value of r and the experimental values, which differ by much smaller percentage than in [6, 48]. This is in accordance with the results presented in section 5. The fact that a block rotating around A and impacting at B may rebound at both A and B (and thus be airborne) is studied in [4, 29]. This is a particularly interesting feature which shows that "distance effects" have to be taken into account. It seems difficult to model such effects with kinematic restitution laws. Some authors like Andreaus et al. [4] and Palmeri et al. [42] introduced some compliance at the contacts and frictional effects in order to cope with such complex dynamics. In [5] the nonsmooth mechanics framework is adopted and friction with a non-constant sliding coefficient is used. In [51]

the normal and tangential (Coulomb's friction) models are penalized so that the rocking block (sticking rocking) dynamics is a smooth second order differential equation, that may be stiff. Taniguchi [62] uses the Housner angular velocity restitution coefficient, and Coulomb's law during non-impacting phases of motion. He points out that perfect rocking seldom occurs, whereas stick/slip phases may be the common behaviour. It is worth noting also that in most of the papers on the rocking block, the restitution coefficients at the contact points A and B are not measured, and sometimes even the friction coefficients are not given. Only r is measured, which means that the other parameters have to be fitted.

The conclusions to be drawn from all these works are that experimental results are not always easy to interpret, rendering the models' validation a hard task. It happens that the dynamics of a block on a rigid ground with friction is a rather unexpectedly complex process, certainly as complex as the Newton's cradle which is frictionless. This makes the design of good *predictive* models a rather tough task. Also, the experiments are always prone to a number of uncertainties like:

- friction with grooves on the foundation,
- vibrational effects inside the block, which are not well understood,
- deformation and vibrations of the foundation,
- heterogeneous material so that the center of mass is not the geometric center,
- damage at the contact points, so that the corners are not the exact rotation points,
- three-dimensional effects,
- pivot friction at the contact points,
- line or surface contact effects, *etc.*

By line or surface contact effects, we mean that the block's surface that collides with the ground, and the ground itself, never possess a perfect geometry. It may happen that the contact is established at some isolated points of the surface, or with some subsets of the surface. Thus the block's geometric width may not correspond to its "rocking block" equivalent width, or *effective* width. The two extreme cases are when the base is concave (the corners are the contact/impact points and the geometric and effective width are equal), and when it is convex (there are no more impacts). Such issues were raised in [52] where it is noted that *overturning responses of blocks with multiple rocking points are equivalent to more slender blocks with simple basal contact conditions*. In other words, when the contact occurs at several points of the base, the equivalent perfect block with two contact/impact points at A and B is more slender. In addition it has been noticed experimentally that the block's motion may be very sensitive to initial data, a very small change in the initial position can cause a big change in the block's response [6, 41]. For all these reasons, getting very accurate prediction with rigid body models is expected to be a tough task in general. Getting general tendencies may be a reasonable and useful goal, instead.

According to [29] the overall deformation effects (waves due to the shocks and travelling inside the block) do not influence the rocking block dynamics when the height/width ratio is small enough (*e.g.* when $\frac{L}{l} \leq 15$ for steel blocks). This would however require some rigorous confirmation, and may be untrue if the experiments are led with a foundation of the same mass as the block (as is the case in [45, 46]). As shown in [32] the impact law we are using can reproduce some wave effects in chains of balls, which are responsible for the dispersion of the energy. It is therefore quite possible that the model is able to encapsulate some vibrational effects in the block as well. But are these vibrational effects those of the real system? We do not tackle this tough issue in this paper. It is however crucial to keep in mind that a model that is obtained within a planar rigid body framework, may only quantitatively approximate and just qualitatively predict a real block's motion. Requiring more is simply hopeless. A typical and very interesting illustration of this is in section 4.3, Table III and figure 4 of [45]. They tested four blocks with $\frac{L}{l} = 4, 5.88, 8.33$ and 2.85 respectively. They calibrated a discrete element model from free-rocking experiments on these four blocks by fitting the equivalent stiffness and damping terms of the DE model. Surprisingly enough the fitting process resulted in a seemingly erratic process where the stiffness and the damping had to be increased or decreased with no obvious logic, and sometimes drastically changed (especially for their specimens 3 and 4). Three dimensional effects may be responsible for this, see also section 6.1.

Another conclusion from the above developments is that adding Coulomb's friction within the kinematic framework cannot help solving the problem of rocking. The law of section 2.3.4 is the *only one* that models rocking motion, and this explain why the rocking motion community has been using the angular velocity restitution coefficient in the past 50 years: there is no other model that is available. At the present time, friction is therefore introduced in the block dynamics only outside the impacts, as for instance in [16]. Friction at the impacts is not modeled, except when the contacts are compliant so that the rigid body framework is lost. It is known however that stick/slip behaviour during the impacts may influence significantly the shock dynamics [10, 35, 61]. It is apparent from the above results and comments that introducing a correct model of friction in the block dynamics, *both* at impacts and during contact phases, is a mandatory step. Tackling this objective within the framework of rigid body systems and multiple impacts with friction is done in the sequel of this paper.

3 The extended Darboux-Keller impact dynamics

The simulations which are presented in the next sections are of the event-driven type [2]. As alluded to above, the advantage of this impact dynamics is that its parameters are the energetic coefficients of restitution at A and B , the coefficients of friction at A and B , and the elasticity coefficient ($\eta = 1$ for linear elasticity, $\eta = \frac{3}{2}$ for Hertz contact). These parameters are determined from material properties and/or independent experiments. Then the numerical integration is processed. In order not to confuse the kinematic models and the energetic ones,

the energetic restitution coefficients will be denoted as $e_{n,i}^*$, $i = 1, 2$. It is known, indeed, that the kinematic and the energetic coefficients may not be equal one to each other, even in single impacts [35, 61].

The impact model proposed in [31, 33] is summarized as follows in the frictionless case. The contact stiffnesses are denoted as k_i , the potential energy at contact i is E_i . The matrix W is the jacobian between the generalized velocities \dot{q} and the contact points normal relative velocities.

- Contact parameters: $\gamma_{ij} = \frac{k_i}{k_j}$, $e_{n,j}^*$, $1 \leq i \leq m$, $1 \leq j \leq m$, η ($= 1$ or $= \frac{3}{2}$, or other values).
- Dynamical equation:

$$M \frac{d\dot{q}}{dP_i} = W \frac{dP}{dP_i} \text{ if } E_{ji}(P_j, P_i) \leq 1 \text{ for all } j \neq i \quad (37)$$

with the distributing law:

$$\frac{dP_j}{dP_i} = \gamma_{ji}^{\frac{1}{\eta+1}} (E_{ji}(P_j, P_i))^{\frac{\eta}{\eta+1}} \quad (38)$$

$$E_{ji} = \frac{E_j(P_j)}{E_i(P_i)}, \quad 1 \leq i \leq m, \quad 1 \leq j \leq m \quad (39)$$

$$E_j(P_j) = \int_0^{P_j(t)} \mathbf{w}_j^T \dot{q} dP_j, \quad W_{r,j} = \int_0^{P_j(t_c)} \mathbf{w}_j^T \dot{q} dP_j, \quad W_{c,j} = \int_{P_j(t_c)}^{P_j(t_f)} \mathbf{w}_j^T \dot{q} dP_j \quad (40)$$

and the time t_c at the contact j is calculated from $\dot{\delta}_j(t_c) = 0$, while t_f is calculated from the energy constraint $W_{r,j} = -(e_{n,j}^*)^2 W_{c,j}$. Coulomb's friction can be easily added in the impact model, at the force (or infinitesimal impulse) level. In this work we use an enhanced model with a static μ_s and a dynamic μ friction coefficients, see figure 6. This impact model is therefore really a rigid body model with one restitution coefficient and one (or two) friction coefficient *per* contact. More details on the implementation may be found in [31, 33, 34], and the code which has been used for the simulations is given in section A (a similar event-driven code is also available in the SICONOS platform [57]). For the dynamics outside the impacts the LCP in (4) is used to integrate the system, and either an explicit Euler or a Runge-Kutta algorithms are implemented. This is not the optimal way to integrate such complementarity systems [2] but proves to be sufficient for such a simple application. It is noteworthy that the numerical scheme that is employed next is of the *event driven* type (see [2] for a definition), and that all the stick/slip and contact/detachment conditions are carefully taken care of. The main novelties of this impact law are the insertion of Coulomb's friction during the impacts, and the use of energetic restitution coefficients in a multiple impact framework.

From now on, the model in (37) through (40) which was proposed in [31] will be referred to as the LZB model.

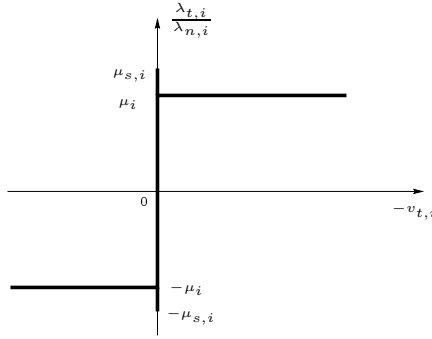


Figure 6: The friction model.

4 The frictionless case

In this section some numerical results are presented for the frictionless case. Some of these allow us to illustrate the fact that the trajectories in simple blocks impacting at one corner, may be discontinuous with respect to the initial data, something that is known from mathematical analysis [7, 43]. This property is, *per se*, of no interest to us. However as we shall see later, it is linked to the kinetic angle between the two constraint surfaces $\Sigma_1 = \{q \in \mathbb{R}^3 \mid f_1(q) = 0\}$ and $\Sigma_2 = \{q \in \mathbb{R}^3 \mid f_2(q) = 0\}$ at $\theta = 0$. The kinetic angle will in turn allow us to determine some general patterns in the block's motion at impacts. In the next simulations the parameters are: $g = 0$ (no gravity), $\mu_1 = \mu_2 = 0$ (no friction), $e_{n,1}^* = e_{n,2}^* = 0$, $m = 2$ kg. The initial data is $q^T(0) = (\frac{l}{2} \cos(\theta_0) - \frac{l}{2} \sin(\theta_0), \frac{l}{2} \sin(\theta_0) + \frac{l}{2} \cos(\theta_0) + 0.1, \theta_0)$, and $\dot{q}^T(0) = (0 \ -1 \ 0)$, *i.e.* the block is sent on the obstacle with a translational vertical motion, and hits it at one corner, except if $\theta_0 = 0$ where both A and B hit the ground at the same time. This corresponds to planar blocks sliding on a horizontal air cushion table. The results are depicted in figures 7 to 9, for three kinetic angle values: $\theta_{12} < \frac{\pi}{2}$, $\theta_{12} = \frac{\pi}{2}$ and $\theta_{12} > \frac{\pi}{2}$. The abscissa in figures 7 (b) (c), 8 (b) (c) and 9 (b) (c) is the initial angle $\theta(0)$. Figures 7 (a), 8 (a) and 9 (a) depict the admissible domain in the (θ, y) plane.

The following comments arise from figures 7 to 9:

- The sign of the final value of $\dot{\theta}$ changes when θ_0 passes through the critical angle θ_c (figures 7 (c), 8 (c) and 9 (c)). It is noteworthy that for $|\theta_0| > \theta_c$ slender blocks become flat and flat blocks become slender.
- For $\theta_0 = \pm\theta_c$ the final kinetic energy is zero, as expected for the double-impact with zero restitution.
- For $\theta_0 \in (-\theta_c, \theta_c)$ the final kinetic energy is very small, however it varies with two maximum values, indicating that the block does not come to rest for all values of the initial angle smaller than θ_c . These regions correspond to half-rocking motion with two impacts. As θ_{12} passes through $\frac{\pi}{2}$, the region where the final $\dot{\theta}$ is zero passes from a large region (see figure 7 (c) for flat blocks) to one point (see figures 7 (c) and 9 (c) for slender blocks).

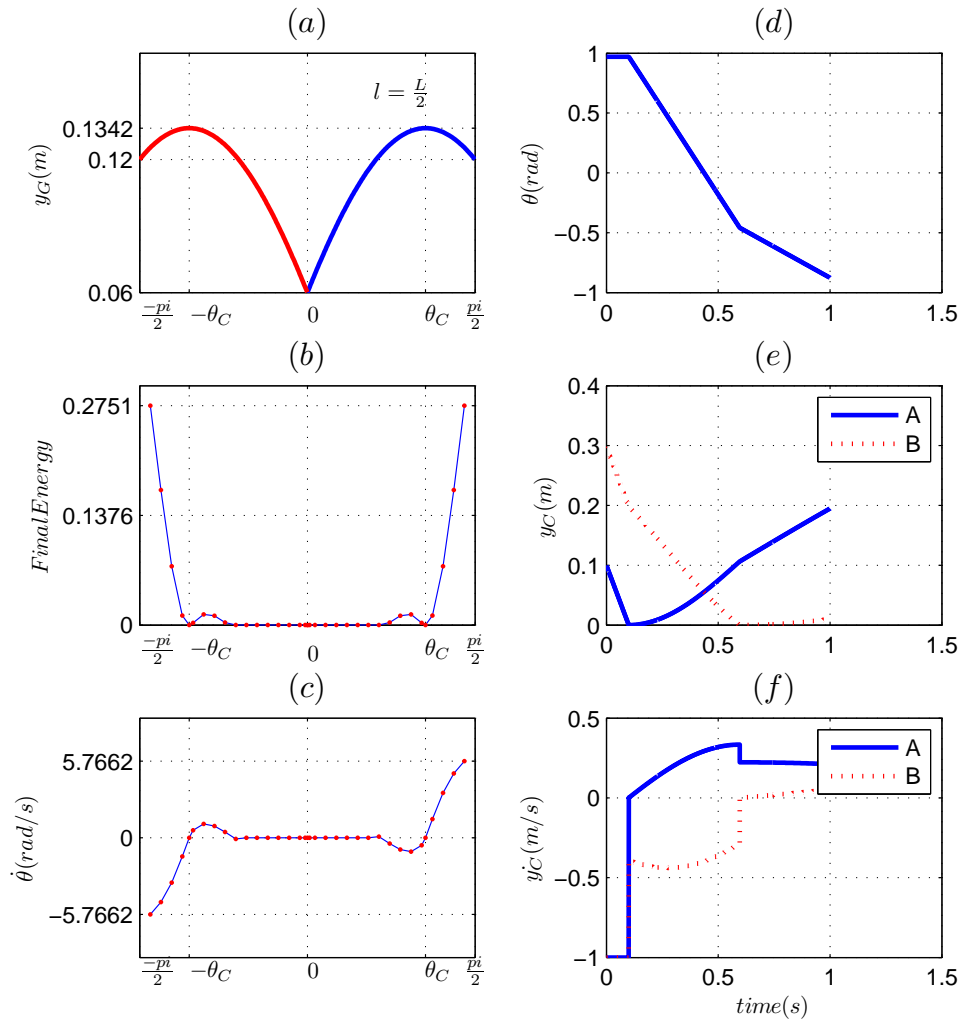


Figure 7: Admissible domain, final energy, final $\dot{\theta}$, angular position, normal position and velocities at A and B, $\theta_{12} < \frac{\pi}{2}$, no gravity.

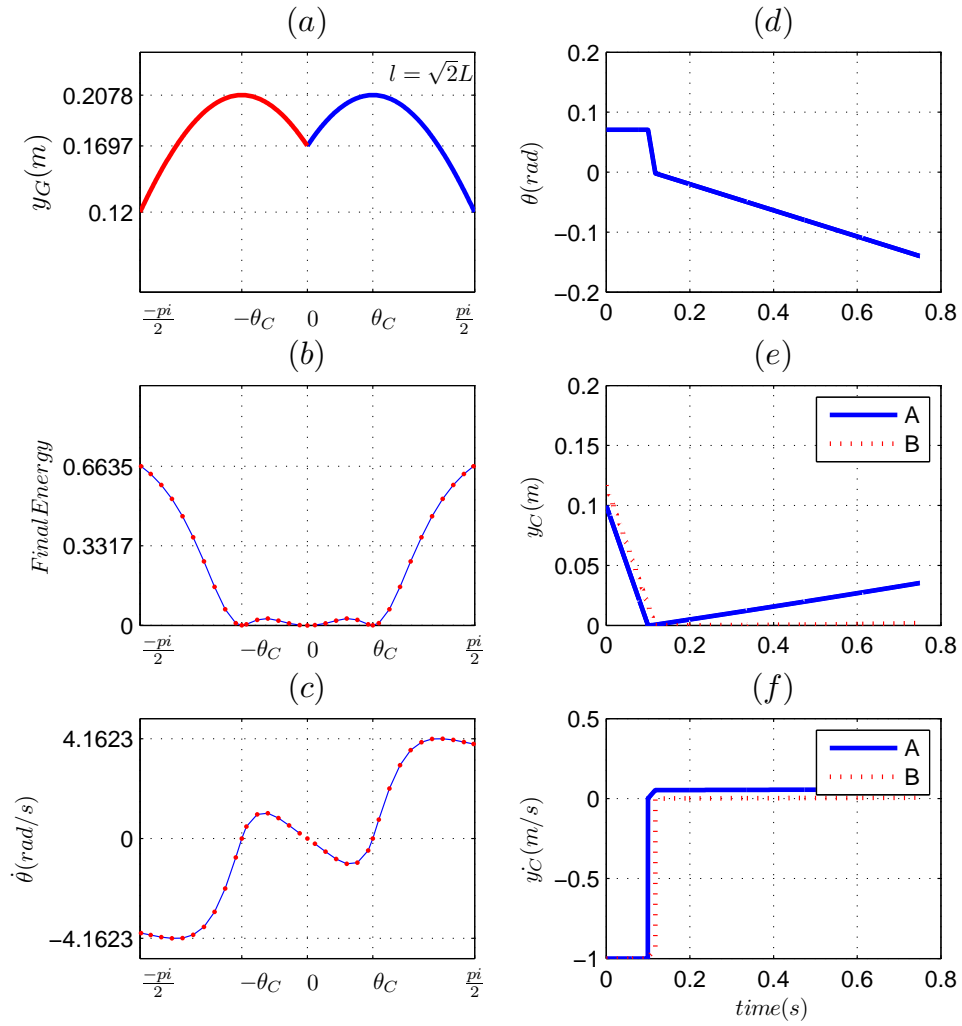


Figure 8: Admissible domain, final energy, final $\dot{\theta}$, angular position, normal position and velocities at A and B, $\theta_{12} = \frac{\pi}{2}$, no gravity.

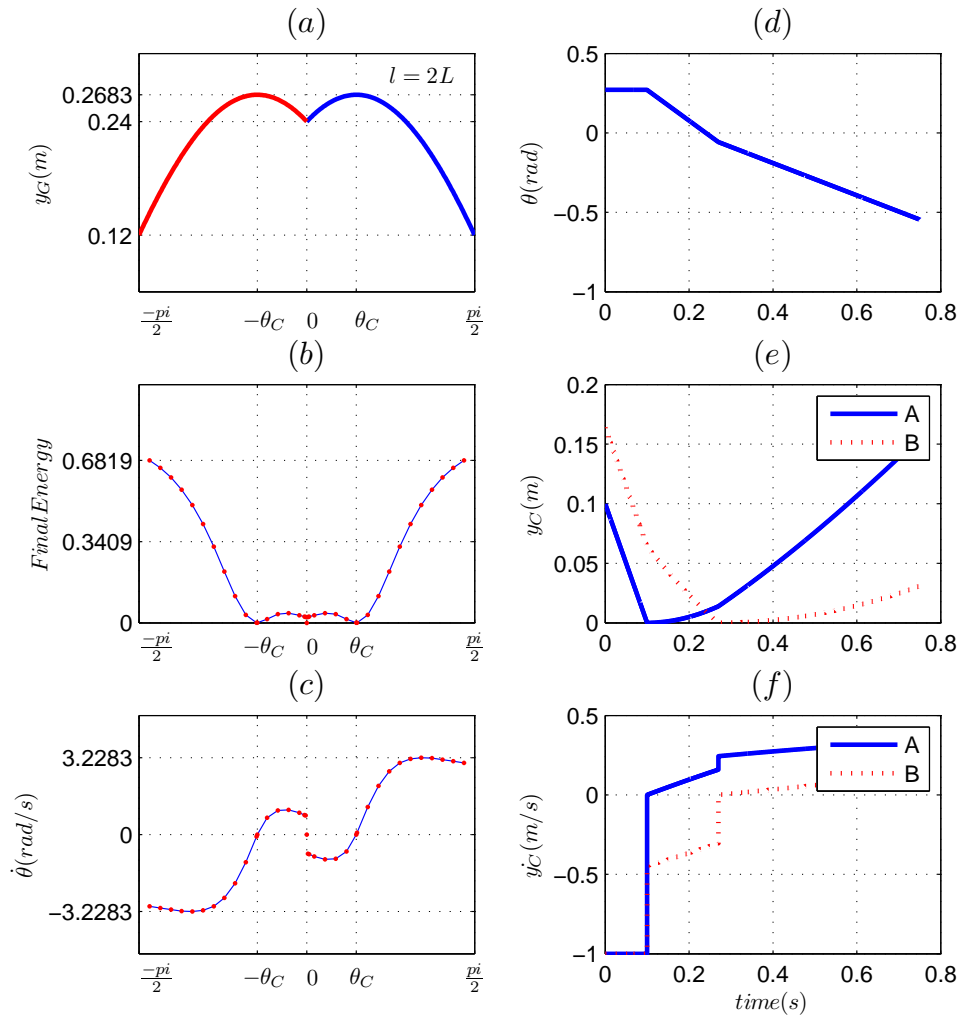


Figure 9: Admissible domain, final energy, final $\dot{\theta}$, angular position, normal position and velocities at A and B, $\theta_{12} > \frac{\pi}{2}$, no gravity.

- For $|\theta_0| > \theta_c$ the final kinetic energy is positive and increases with $|\theta_0|$. The block overturns as expected for such initial orientation.
- There is a jump in the curve $\dot{\theta}(\theta_0)$ at $\theta_0 = 0$, for $\theta_{12} > \frac{\pi}{2}$ (see figure 8 (c)). This illustrates the well-known fact that trajectories may be discontinuous with respect to initial data for such kinetic angles [43]. Comparing figures 7 (b), 8 (b) and 9 (b), one sees that the zero final energy region vanishes when θ_{12} passes through $\frac{\pi}{2}$, indicating the fact that slender blocks overturn more easily than flat ones.
- From figures 7 (d) (e) (f), 8 (d) (e) (f) and 9 (d) (e) (f), one sees that there are only two impacts.
- It is interesting to note that there is a continuous deformation in the curves (c) from figure 7 (c) to 9 (c).

It is noteworthy that the block detaches from the ground after the impacts, despite $e_{n,1}^* = e_{n,2}^* = 0$. This is due to the transfer of energy between the translational and the angular motions. Let us examine this with the corresponding LCP. Suppose the impact has occurred at A . Starting from (3) and differentiating twice $f_2(q)$ one obtains the complementarity relation just after the impact:

$$0 \leq \lambda_{n,2}(t) \perp \left(\frac{1}{m} + \frac{R^2}{I_G} \sin^2(\alpha - \theta(t)) \right) \lambda_{n,2}(t) + \dot{\theta}^2(t) R \cos(\alpha - \theta(t)) \quad (-g) \geq 0 \quad (41)$$

where $R = \frac{\sqrt{I^2 + L^2}}{2}$, α is the angle such that $f_2(q) = y - R \cos(\alpha - \theta)$. In the system's configuration of interest one has $\alpha > \theta(t)$ so that $\cos(\alpha - \theta(t)) > 0$. The LCP matrix is $1 + \frac{R^2}{I_G} \sin^2(\alpha - \theta(t)) > 0$ so the LCP always has a unique solution, and since $\dot{\theta}^2(t) R \cos(\alpha - \theta(t)) \geq 0$ this solution is $\lambda_{n,2}(t) = 0$. The normal acceleration of the point A is therefore given by $\frac{d^2 f_2}{dt^2}(t) = \dot{\theta}^2(t) R \cos(\alpha - \theta(t))$ and detachment occurs whenever $\dot{\theta}(t) \neq 0$ and $\cos(\alpha - \theta(t)) > 0$. We have added the gravity term in (41) to indicate that when gravity is present (the block falls down vertically) then detachment may no longer occur after an impact. The simulations with gravity are presented in figures 10 to 12.

- The major discrepancy with the no-gravity case is that the block comes to rest for all $|\theta(0)| \leq \theta_C$ as is visible on figures 10 (b), 11 (b) and 12 (b). This is logical in view of the LCP (41) solutions with gravity. One may see the falling block as a generalized bouncing ball where several impacts occur before the stabilisation on the ground, instead of a single impact. Flat blocks possess a larger region of initial orientations that yield stabilisation, as expected (compare figures 10 (b) (c) and 12 (b) (c)).
- The exchange of energy between A and B is more significant for slender blocks (figure 12 ((d) (e) (f))) than for flat blocks (figure 10 ((d) (e) (f))).
- The overturning issue for angles $|\theta_0| < \theta_C$ is no longer present: all three curves in figures 10 (b), 11 (b) and 12 (b) possess a “well” of stabilisation for $|\theta_0| < \theta_C$. This indicates that overturning will be possible only if, under the same initial conditions, gravity is compensated for (with a base excitation, for instance).

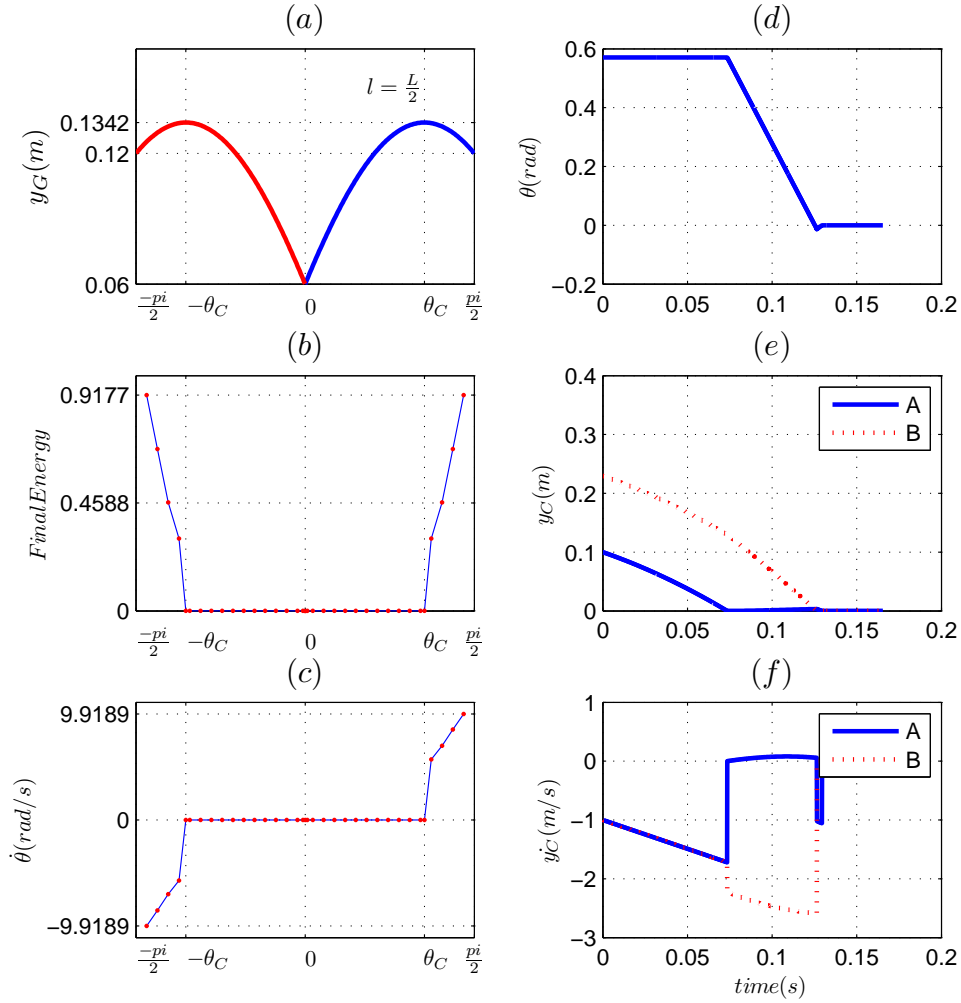


Figure 10: Admissible domain, final energy, final $\dot{\theta}$, angular position, normal position and velocities at A and B, $\theta_{12} < \frac{\pi}{2}$, with gravity.

Remark 11. *When $\mu_1 = \mu_2 = 0$ the gravity center position x remains constant. Thus the contact/impact points A and B undergo sliding motions. One expects that friction will introduce sticking phases and this is what will make the overall block trajectory significantly differ from the frictionless case (making it possible, for instance, that a block may rock without sliding, or that it performs a half-rocking motion while G advances in one direction on the ground).*

The frictionless case shows that the kinetic angle is an important parameter of the block that determines some global pattern of its post-impact motion. This will be confirmed in the next section where friction is considered.

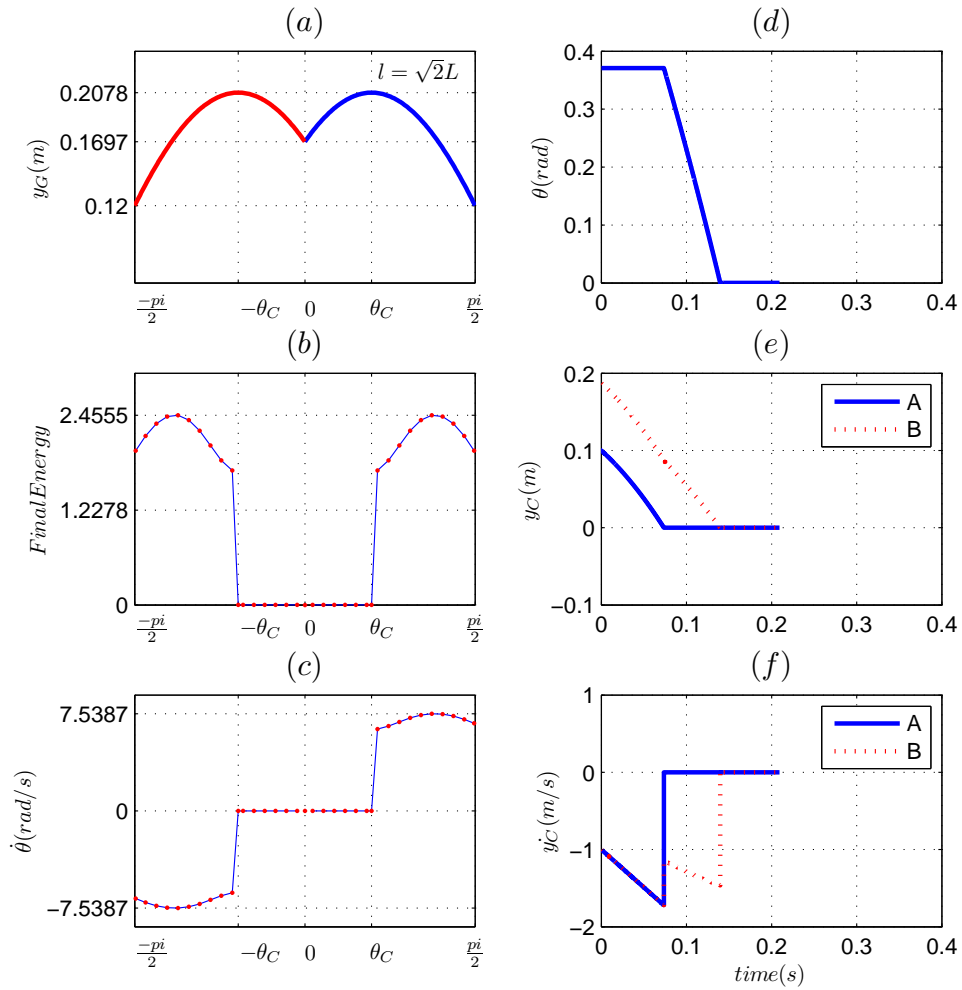


Figure 11: Admissible domain, final energy, final $\dot{\theta}$, angular position, normal position and velocities at A and B, $\theta_{12} = \frac{\pi}{2}$, with gravity.

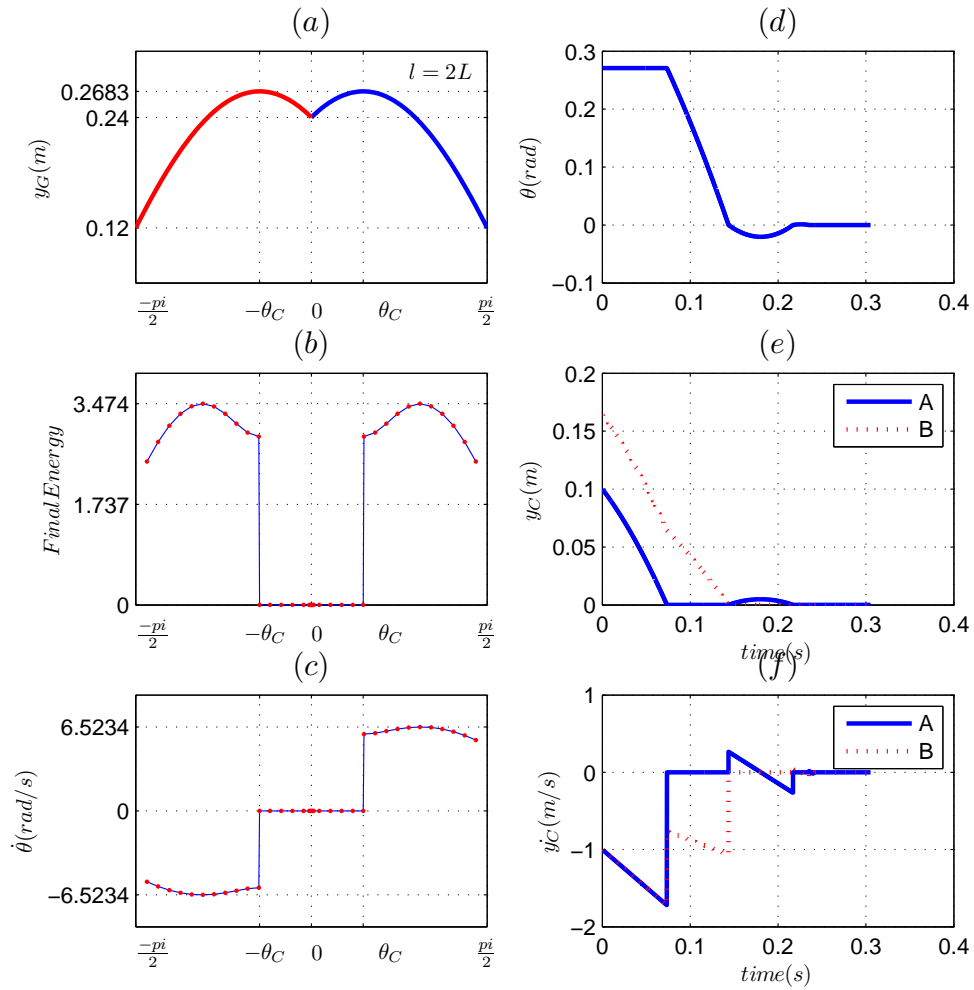


Figure 12: Admissible domain, final energy, final $\dot{\theta}$, angular position, normal position and velocities at A and B, $\theta_{12} > \frac{\pi}{2}$, with gravity.

5 Impacts with Coulomb friction (fixed base)

Let us now turn our attention to the most interesting case of impacts and contact with friction. In our model we allow for a static μ_s and a dynamic μ coefficients of friction. Everyday-life simple experiments show that friction influences a lot the block's motion when it is initialized with contact at a single point, with zero velocity, and let fallen under gravity. Take for instance various glasses with different ratios $\frac{L}{l}$ and let them rock on a table with or without tablecloth: slender glasses behave quite differently from flat ones. A simple STABILO BOSS[©] pen with $\frac{L}{l} \approx 5$ may be used to observe the following: when the pen is released from an initial height of about 20 cm, in a slightly inclined position so that it undergoes a single impact at one corner with the desk, it rebounds very little (two or three cm) but obviously $e_{n,i} > 0$. Now when initialized for rocking (contact at one corner and zero velocity, $\theta < \theta_c$), then it rocks on the desk and stabilizes on it after what looks like an accumulation of impacts (despite there is only a finite number of impacts in reality, but we may expect that a mathematical model will predict such an accumulation, just as it is the case for the bouncing-ball). There may be little sliding at the contact points, or it may stick during the whole rocking motion. Repeating the experiment with a sheet of paper on the desk's surface (hence modifying both $e_{n,i}$ and μ) does not change much the behavior. This simple pen experiment seems to tell us that having $e_{n,i} = 0$ may not be necessary to have rocking motion, contrarily to what the model predicts (see section 2.3). The simulations in this section will bring an explanation to this issue: can rocking be modeled with $e_{n,i} > 0$? Surprisingly enough the conclusion will be that sustained rocking motion implies that $e_{n,1} > e_{\min}$ because too small restitution implies that the block comes to rest after few impacts (typically two or three).

Remark 12. *Obviously such qualitative observations cannot justify a mathematical model. Rigorous comparisons with experimental data have to be performed from the quantitative point of view (as done in [32, 34, 71]). They however prove that a good model should at least be able to reproduce such a variety of motions. The model will be justified later with numerous and detailed comparisons with experimental data found in [45, 46, 17, 29], both for the free-rocking and the base-excitation cases. Therefore our study shows that the proposed model is good both from the qualitative and the quantitative point of views.*

5.1 The role of the kinetic angle

One of the conclusions of section 4 is that the kinetic angle θ_{12} between the two constraints at $\theta = 0$ plays a significant role in the block's motion. We now consider the same three values of θ_{12} as in the foregoing section, *i.e.* the ratios $\frac{L}{l} = 2, \frac{1}{2}$ and $\sqrt{2}$. Gravity is considered in these simulations, $m = 0.02$ kg, and the base is still supposed to be fixed.

The following comments arise from figures 13, 14, 15 and 16:

- $e_{n,1}^* = e_{n,2}^* = 0$: When $\theta_{12} < \frac{\pi}{2}$, point A never rebounds, B hits the ground once and the block is at rest. When $\theta_{12} > \frac{\pi}{2}$, A always rebounds a little, the rebound at A is bigger for larger μ , the block is at rest after

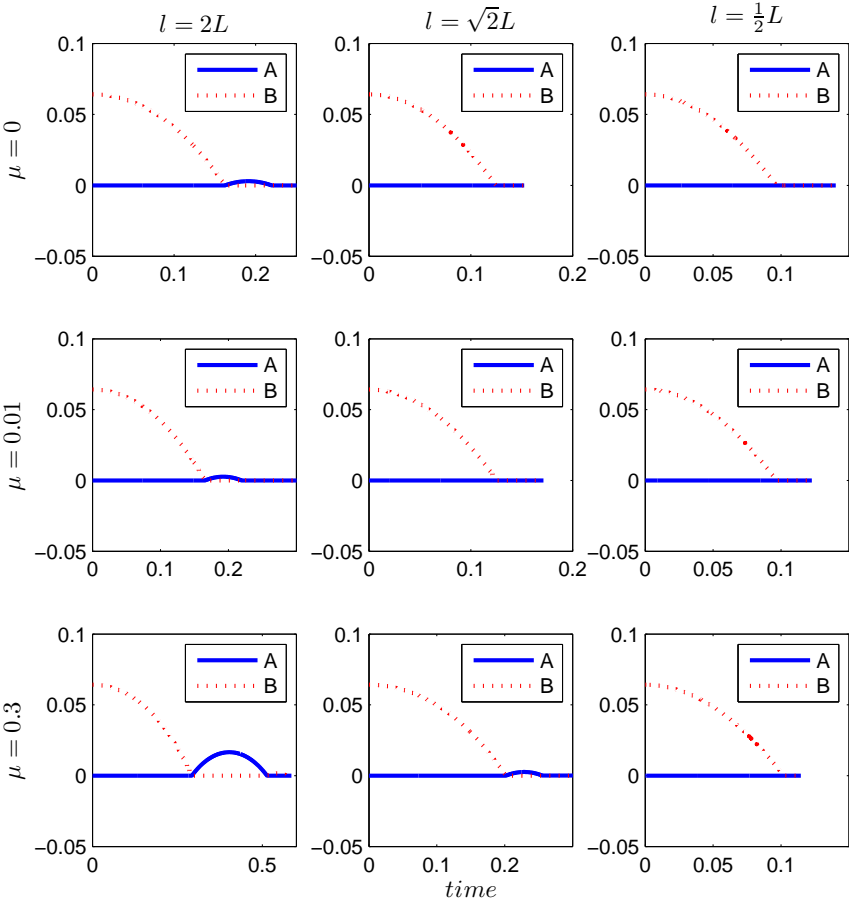


Figure 13: Trajectory at A and B , with $e_{n,1}^* = e_{n,2}^* = 0$, varying μ .

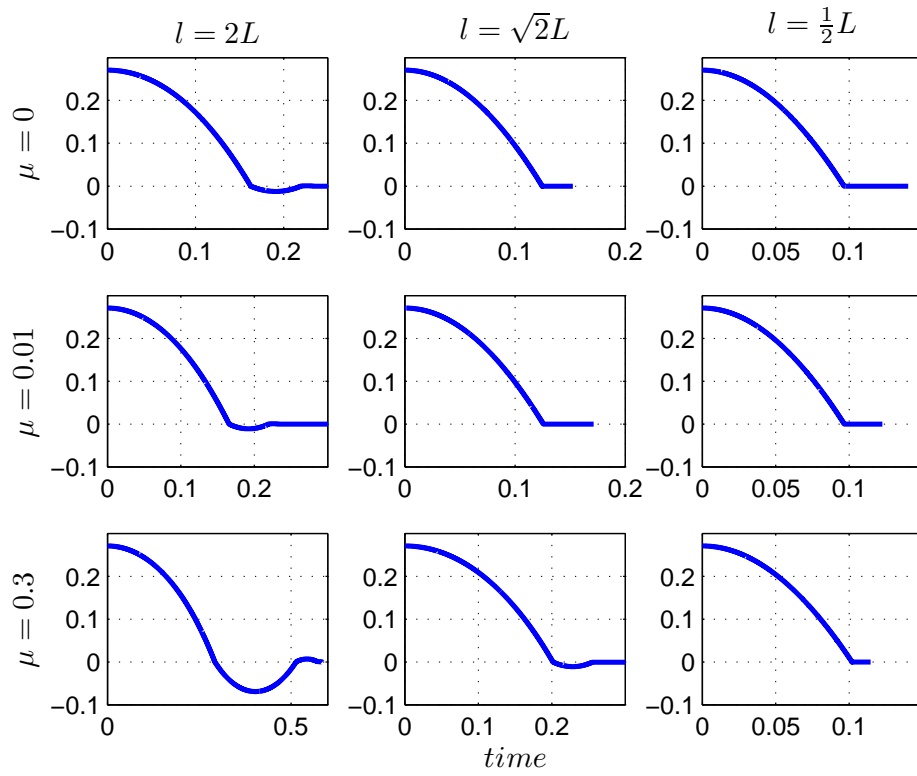


Figure 14: $\theta(t)$ with $e_{n,1}^* = e_{n,2}^* = 0$, varying μ .

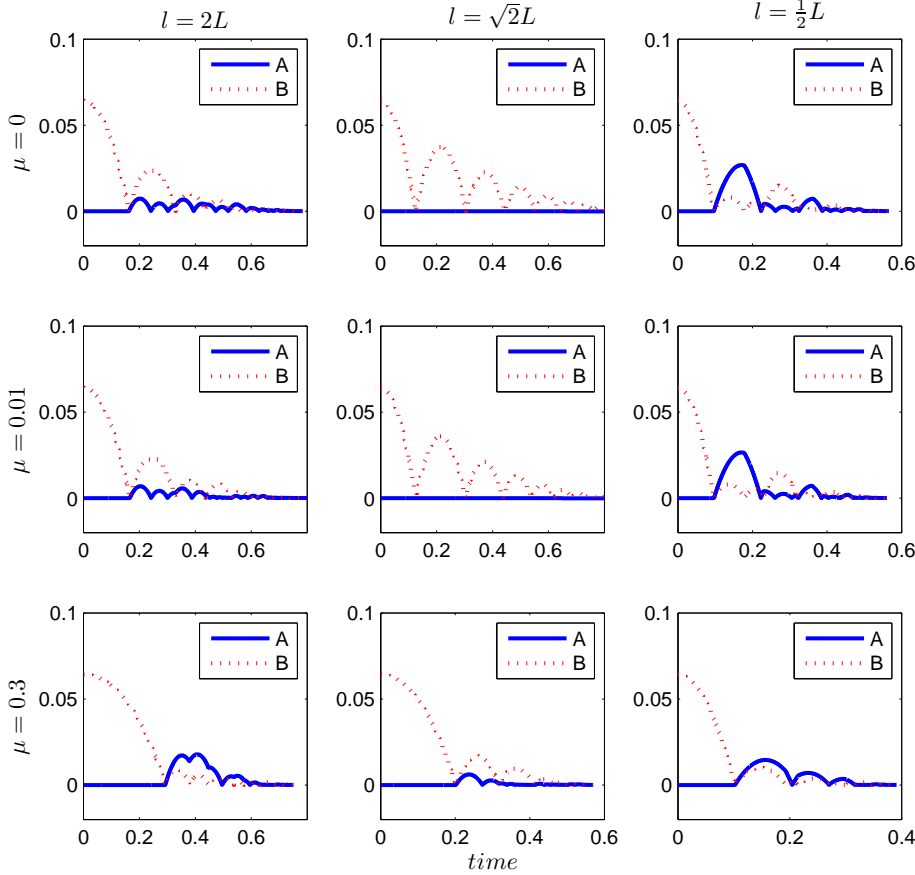


Figure 15: Trajectory at A and B, with $e_{n,1}^* = e_{n,2}^* = 0.8$, varying μ .

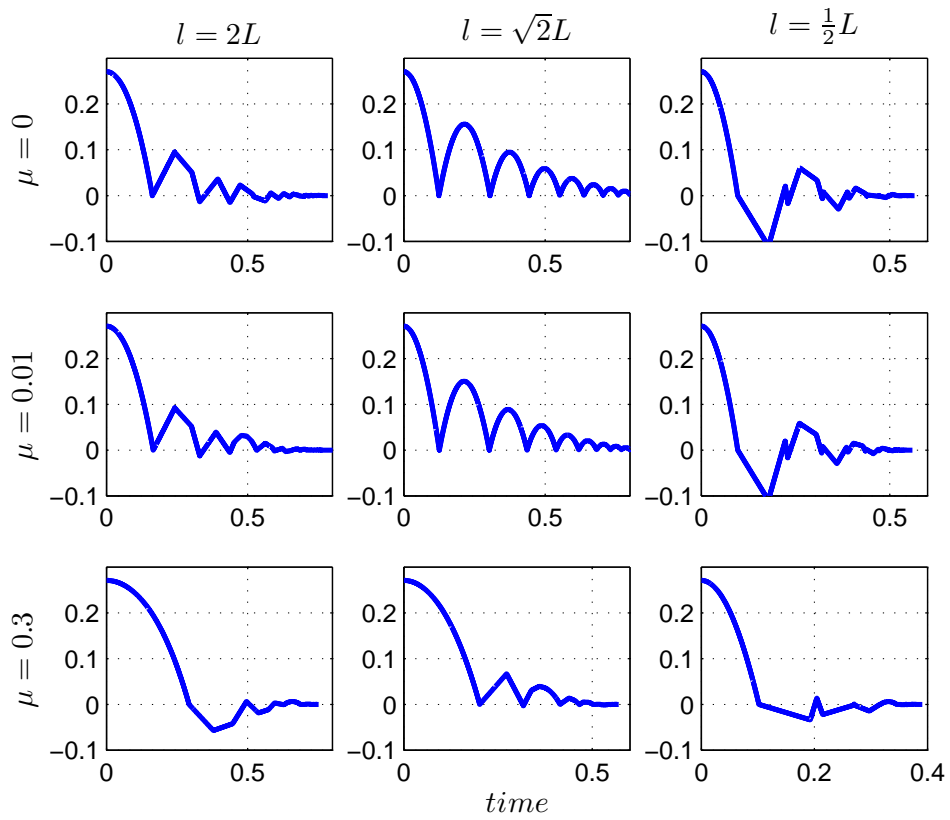


Figure 16: $\theta(t)$ with $e_{n,1}^* = e_{n,2}^* = 0.8$, varying μ .

one impact at B followed by one impact at A . The case $\theta_{12} = \frac{\pi}{2}$ makes a transition between both cases.

- $e_{n,1}^* = e_{n,2}^* = 0.8$: When $\theta_{12} = \frac{\pi}{2}$ and μ is small or zero, A does not detach from the ground, and B undergoes a series of impacts (half-rocking motion, with no exchange of energy from B to A); A detaches and impacts also (*i.e.* part of the energy is exchanged between A and B) when μ is large. When $\theta_{12} < \frac{\pi}{2}$ and μ is small, there is a strong exchange of energy from B to A at the first impact, and from A to B at the second impact; then the energy seems to be balanced between the two contact points; for large μ both contact points take similar energies. When $\theta_{12} > \frac{\pi}{2}$ and μ is small, the first rebound at B is much larger than the ones at A , indicating that the energy exchange between B and A exists but is small; when μ gets larger a much larger part of the energy transfers from B to A at the first impact, and subsequently the energy is more dispersed at the two contact points. Obviously $\theta_{12} = \frac{\pi}{2}$ makes a transition between two different mechanisms of energy dispersion in the block.
- The energy dispersion is such that rocking or half-rocking seldom appear (just as a pathological case for $\theta_{12} = \frac{\pi}{2}$ in figure 15) for the chosen parameters values. It is apparent from figure 15 that the energy dispersion may be a complex nonlinear phenomenon, even for such a simple system as the planar block with two contact points and a fixed base.
- The nonsmoothness of the $\theta(t)$ curve in figure 16 stems from the fact that the block is airborne and impacts while “rotating”.

Remark 13. Consider as in section 2.3 the issue that $e_{n,1}^* = e_{n,2}^* = 0$ is a necessary choice to model perfect rocking motion, *i.e.* rocking where the corner that hits the ground sticks on it after the impact. Perfect rocking is an idealisation and rocking usually is only approximately performed: rebounds and slip occur at the impacting corner before it sticks. Experimental results in the literature report rocking motions with $e_{n,i}^* = 0.9$ [6, 29, 48], which seems to be in complete contradiction with the developments of section 2.3. One can try to use a kinematic restitution model to simulate approximate rocking with $e_{n,i} > 0$. The major issue is then to correctly handle Coulomb’s friction during the rebound phase, in particular at the impacts. The Darboux-Keller approach with energetic restitution coefficients allows one to correctly model impacts with friction. We may infer that the energetic law is useful to predict whether some particular motion will occur for a certain range of parameters and initial conditions, and that the kinematic law may be useful if fast simulation and time-stepping algorithms are needed.

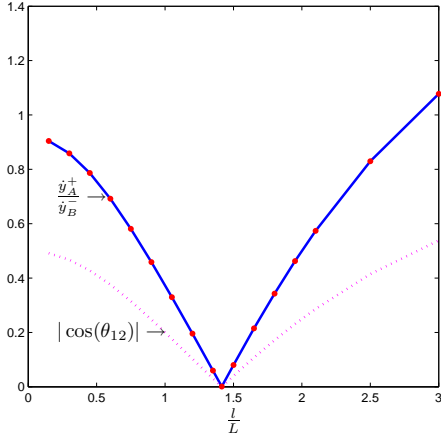
Let us now investigate more deeply the kinetic angle influence by studying the ratio of the vertical velocities $d \triangleq \frac{\dot{y}_A(t^+)}{\dot{y}_B(t^-)}$ after an impact at B while the block rotates without slip around A . This ratio provides an estimation on how much “energy” is transferred from B to A , which may be thought of as a form of energy dispersion in the block. It is noteworthy that the first impact is the only 2-impact, since the rebound phase that may follow it involves simple impacts only. Here we study the dependence of d on the aspect ratio, the friction and the restitution, *i.e.* $d(e_n^*, \frac{l}{L}, \mu, \mu_s)$. In order to separate the effect of dissipation

from the other effects we first focus on $d(1, \frac{l}{L}, \mu, \mu_s)$ in figures 17 through 19. In figure 17 the curves $(\frac{l}{L}, d(1, \frac{l}{L}, \mu, \mu_s))$ are depicted for various values of μ and μ_s . The dashed line on each figure represents the value of $\cos(\theta_{12})$. The initial data are zero velocity and $\theta(0) = 0.12$ rad, and $m = 2$ kg. In all simulations $L = 0.24$ m and l is varied. Some comments arise:

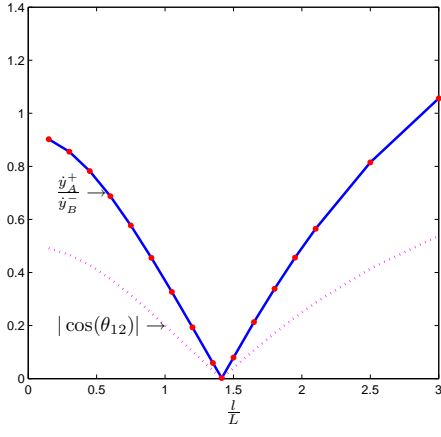
- The $(\frac{l}{L}, d(1, \frac{l}{L}, \mu, \mu_s))$ -curves all possess the same V-shape, independently of the friction value.
- The minimum is attained at $\theta_{12} = \frac{\pi}{2}$ for $\mu = \mu_s = 0$, figure 17. Then, in proportion as friction increases, the minimum point moves to the left until it reaches a stationary point, see figures 17 (b) to 17 (f). In other words there is a “critical” kinetic angle that moves from $\frac{\pi}{2}$ to $\approx \frac{\pi}{2.5}$ (≈ 70 degrees) for $\frac{l}{L} \approx \frac{\sqrt{2}}{2}$. The stationarity is explained by the fact that once μ and μ_s are large enough, the contact/impact points always stick (no slip modes exist) and increasing the friction does not change the dynamics.
- One sees in figure 18 that in the frictionless case there is a simple and remarkable relation between $d(1, \frac{l}{L}, 0, 0)$ and $\cos(\theta_{12})$. This is however lost when friction is present.
- The $\theta(t)$ response is depicted on figure 19 for fixed friction $\mu = 0.6$, $\mu_s = 1$ (hence stick always occurs) and varying aspect ratio $\frac{l}{L}$, so that one can visualize the block’s motion that occurs after the first 2-impact. After the first impact the block becomes airborne before it collides again with the ground.
- When friction is present but small enough, there exist slip and stick phases of motion. This creates some unstable behaviours as seen on figures 17 (c) and 17 (d) with a jump in $d(1, \frac{l}{L}, \mu, \mu_s)$ at some $\frac{l}{L}$. This jump shrinks when friction is zero and when friction is large enough. In the first case it shrinks in the asymptotic part on the right of the curve, in the second case it shrinks in the critical minimum point.

Remark 14. *The papers [14] and [33, 71] deal with the dynamics of a dimer that bounces on a vibrating table, with friction. In both papers it has been shown that the dimer’s motion also possesses a critical aspect ratio that determines two different types of dynamical behaviours (see figure 11 in [71] and figure a (a) in [14]). Though the kinetic angles are not used in these papers, these aspect ratios correspond to some critical kinetic angles of the dimer’s constraints as we saw in remark 2 for the planar block. The results in this section show that the free-rocking motion of a planar block also exhibits some critical kinetic angles.*

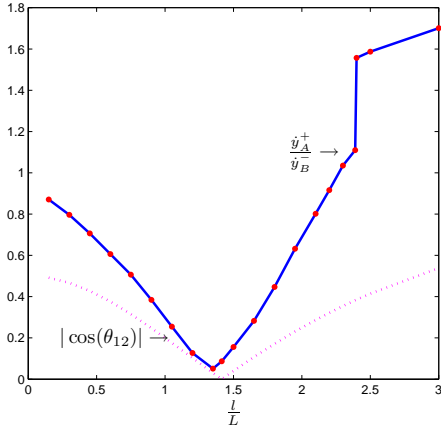
In figure 20 the dispersion factor d is depicted as a function of $\frac{l}{L}$, with $\mu = 0.3$ and $\mu_s = 0.5$, for three different values of e_n^* . It is remarkable that the normal dissipation has no effect on the global shape of the curve, and that the minimum is independent of e_n^* . This leads one to infer that only the aspect ratio and the stick/slip phenomena may play a role. The figure 21 depicts the horizontal velocity of the impacting point A for various aspect ratios, before and after the impact. One sees from figure 21 (b) that there are three distinct regions in the $(\frac{l}{L}, d)$ curves for the tangential behaviour *during the impact*:



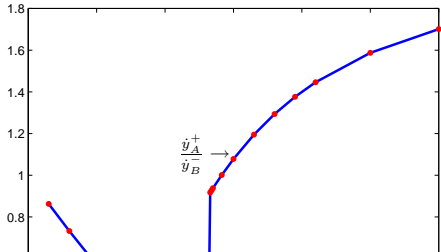
(a) $\mu = \mu_s = 0, e_n^* = 1.$

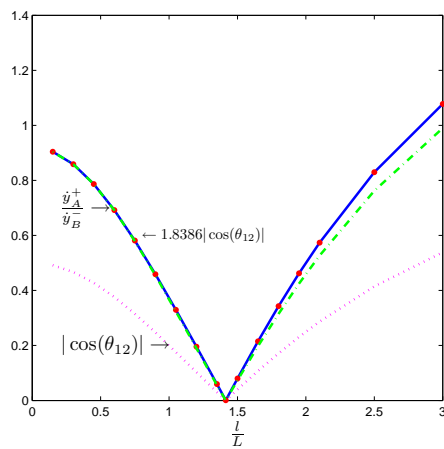


(b) $\mu = 0.01, \mu_s = 0.02, e_n^* = 1.$

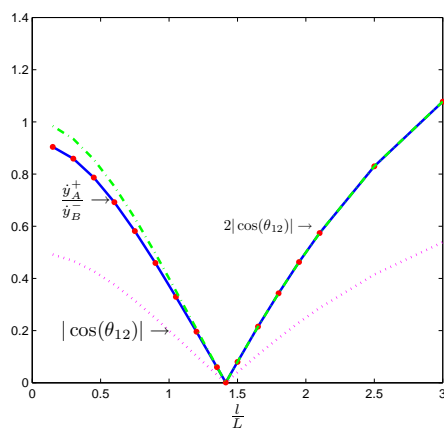


(c) $\mu = 0.15, \mu_s = 0.3, e_n^* = 1.$



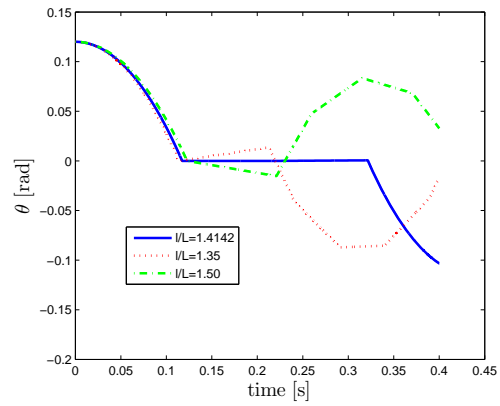


(a)

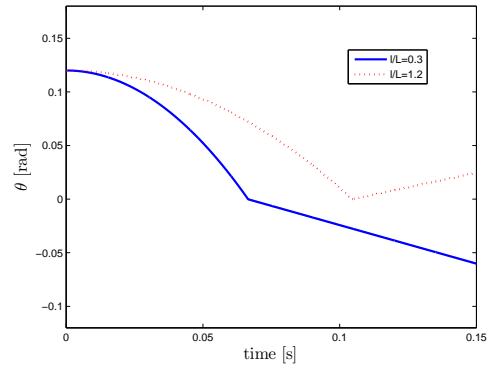


(b)

Figure 18: Dispersion with $\mu = \mu_s = 0$, $e_n^* = 1$.



(a)



(b)

Figure 19: $\theta(t)$ response, $\mu = 0.6$, $\mu_s = 1$.

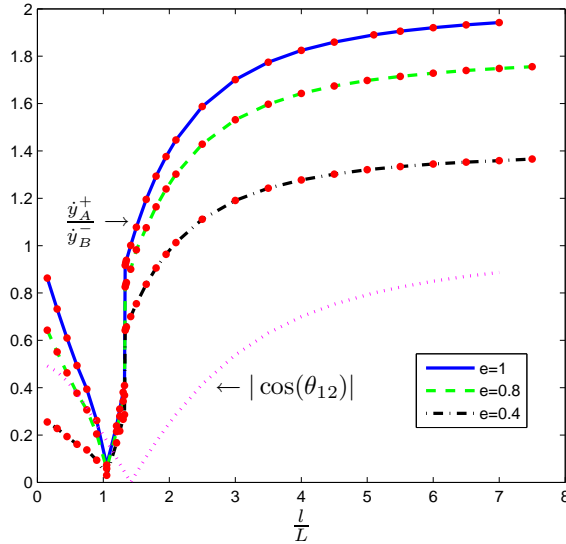


Figure 20: Dispersion d with varying e_n^* .

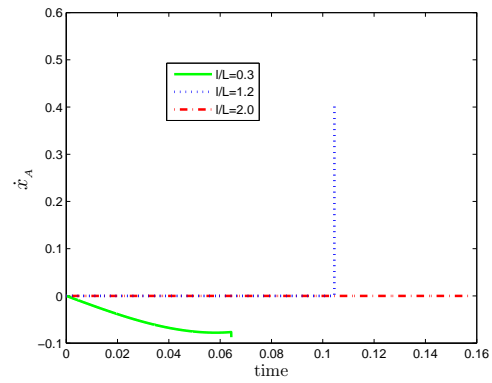
- slip with tangential velocity reversal for flat blocks,
- slip with unidirectional tangential velocity for moderately slender blocks,
- stick for slender blocks.

The Darboux-Keller approach allows one to compute the velocities evolution during the impact, where the time-scale is the contact forces impulse (in case of a multiple impact this is the impulse at the so-called primary contact point, see [31] for details).

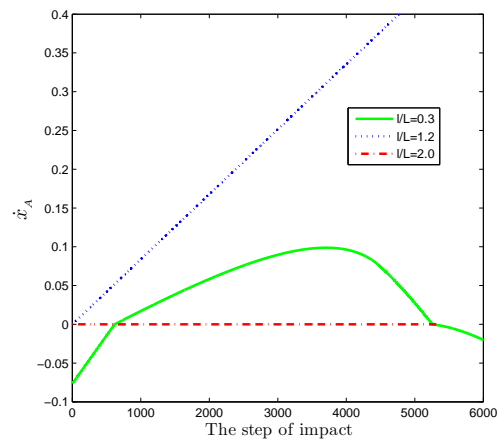
In figure 22 are reported the values of d computed from the fitted parameters found in section 6 where experimental results from [46, 29, 17] are used. The fitted parameters are used to compute d from the simulations. Since there is a good matching with the experimental results one may consider that the computed d matches with the experimental ones, though they are not directly available from measurements. Unfortunately only few data are available, in particular we have no results for flat blocks.

5.2 Rocking motions

In this section it is proved that the LZB model allows one to simulate an interesting set of different dynamical behaviours of the planar block. Let us now examine Figures 23 to 28. The simulations are done for $\frac{l}{L} = 5$. From figures 23 (a) to 24 it is apparent that if friction is large enough, $e_n^* = 0.9$ yields some kind of “macroscopic” rocking, where each phase of rocking motion starts with a phase of impacts with stick/slip motion, before the impacting corner stabilizes on the ground. Decreasing e_n^* to 0.3 also decreases the impacting phase duration and magnitude, as shown in figures 25 to 26. The importance of having a high

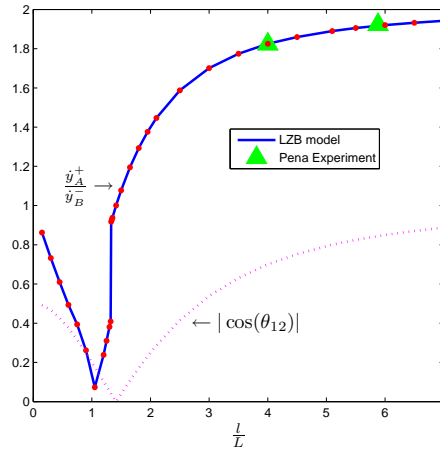


(a) Velocities before the impact

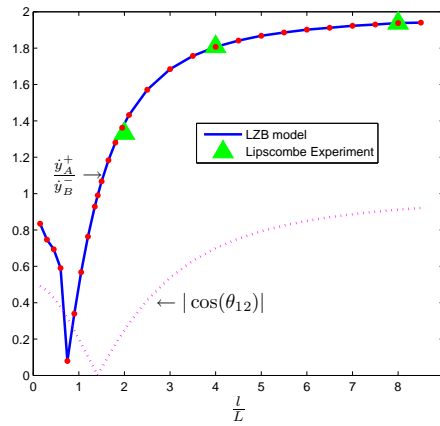


(b) Velocities during the impact

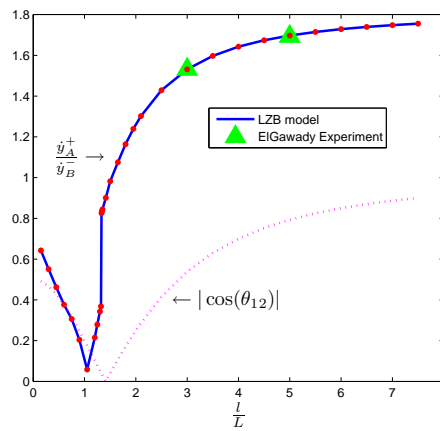
Figure 21: Horizontal velocity at A.



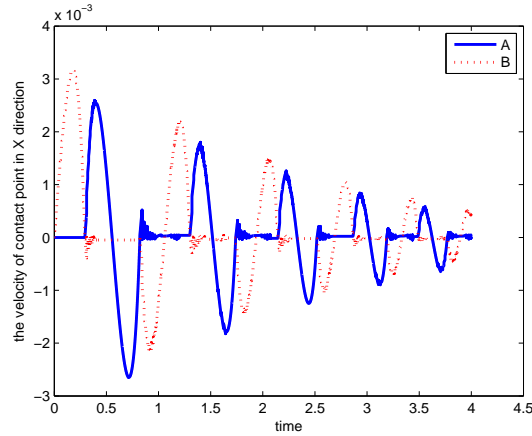
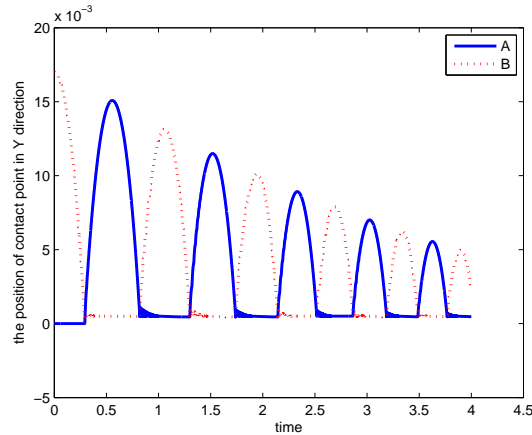
(a) From the experimental data in [46] (fitted parameters).



(b) From the experimental data in [29] (fitted parameters).



(c) From the experimental data in [17] (fitted parameters).

(a) Horizontal velocity of A and B .(b) Vertical position of A and B .Figure 23: $e_{n,1}^* = e_{n,2}^* = 0.9$, $\mu_1 = \mu_2 = 0.3$, $\mu_{s,1} = \mu_{s,2} = 0.5$.

enough friction is illustrated in figures 27 (a) to 28. In figure 27 (b) one sees that the impacting corner does not stabilize quickly enough on the ground, so the contact point does not stick (compare figures 23 (a), 25 (a) with figure 27 (a)). The result is that the block has a global motion that is no longer of the rocking type as is apparent in figures 24 and 26, but of the “forward” type as in figure 28: the block’s center of mass advances on the ground. This leads us to propose that a block’s motion may be named of the rocking type if its mass center trajectory has the shape as in figures 24 and 26. A criterion based on some distance with respect to the ideal rocking may then be used. Notice that in figure 27 (a) the two curves for A and B are identical, so the dashed curve for B is not visible.

Let us now turn our attention to figures 29 and 30. The figure 29 depicts the values of r which are computed from figures 23 (a) and 23 (b). As noted above rocking occurs with impact phases each time a corner hits the ground. The

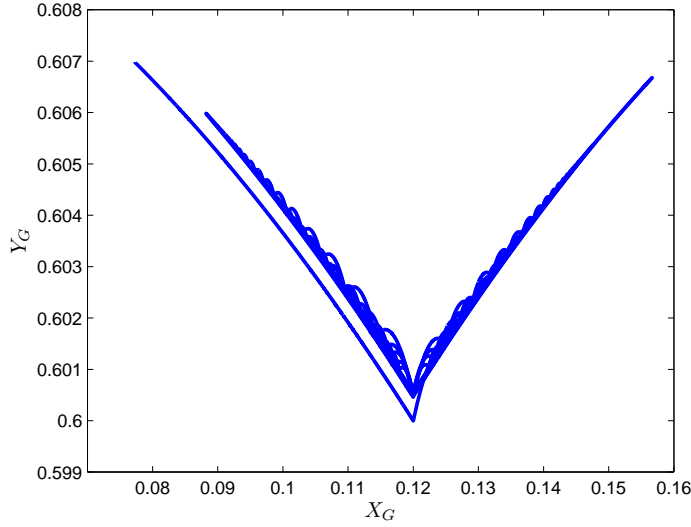
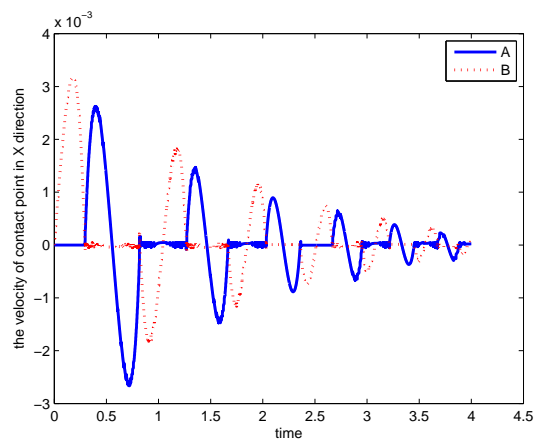
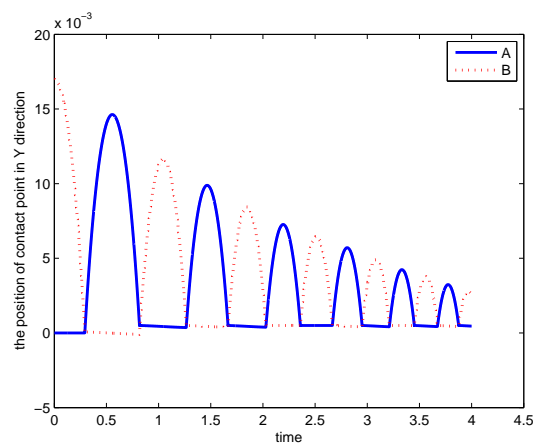


Figure 24: Trajectory of the mass center, with $e_{n,1}^* = e_{n,2}^* = 0.9$, $\mu_1 = \mu_2 = 0.3$, $\mu_{s,1} = \mu_{s,2} = 0.5$.

restitution r is computed with the values of $\dot{\theta}(t^+)$ and $\dot{\theta}(t^-)$ at the first impact. From figure 29 it follows that r is not constant from one impact to the next, however the variation is quite small within $[0.8907, 0.8903]$ and the variations may be attributed to numerical approximations. Figure 30 reports the evolution of r with e_n^* , where an averaged value of r is computed for each rocking motion. For $\frac{L}{l} = 5$, the value of r predicted by the moment of momentum conservation (see the table 1 in section 2.7) is equal to $r = -0.942$. This value coincides with the value of r in figure 30 for $e_n^* = 0$. r decreases when e_n^* increases, which may at first sight look counter-intuitive. The largest relative error for $e_n^* = 0.9$ (which is a common value reported in experimental results [29, 45]) is of 6%. In view of the dynamics of figures 23 and 25 (b) the result is easily explained: the impacting phase vanishes as e_n^* decreases so that the dynamics tends to that of the ideal rocking motion with maximum dissipation, where the impacting corner perfectly sticks after the shock. When $e_{n,1}^* = e_{n,2}^* = 0.9$ the impacting phase with stick/slip dissipates energy. In fact one may conclude that the energy is either dissipated in one shot if $e_{n,1}^* = e_{n,2}^* = 0$, or after an impacting transient if $e_{n,1}^* = e_{n,2}^* = 0.9$. This might explain why a kinematical restitution law with $e_{n,1} = 0$ is sufficient if one is interested only in a crude approximation of the block's motion, with a correct estimation of the energy dissipation with a coefficient $e_{n,21} = -r$. The underlying assumption is then that rocking *does* occur. A major issue, which can be solved only numerically in view of the complexity of the phenomena and of the number of parameters, is to determine the conditions under which rocking occurs. Later in this paper we shall focus on the *overturning* issue in a dynamical situation.

(a) Horizontal velocity of A and B .(b) Vertical position of A and B .Figure 25: $e_{n,1}^* = e_{n,2}^* = 0.3$, $\mu_1 = \mu_2 = 0.3$, $\mu_{s,1} = \mu_{s,2} = 0.5$.

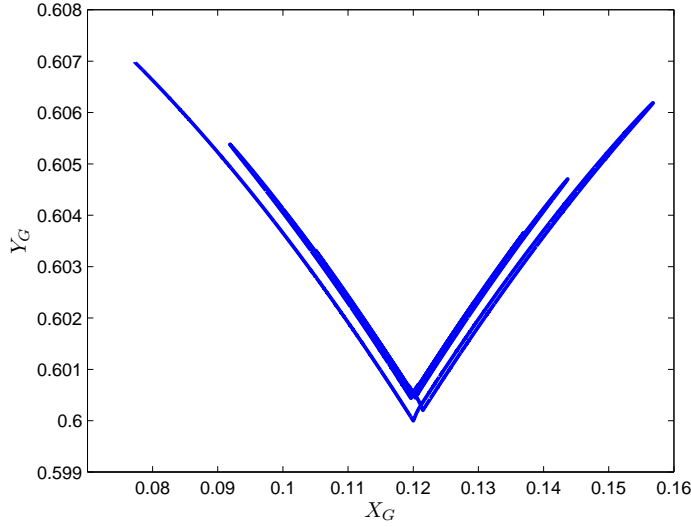


Figure 26: Trajectory of the mass center, with $e_{n,1}^* = e_{n,2}^* = 0.3$, $\mu_1 = \mu_2 = 0.3$, $\mu_{s,1} = \mu_{s,2} = 0.5$.

5.3 Conclusions

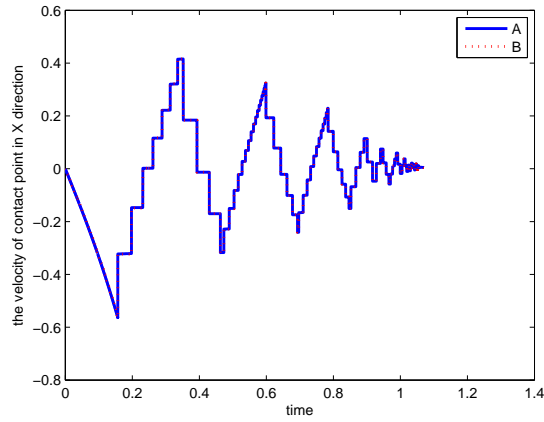
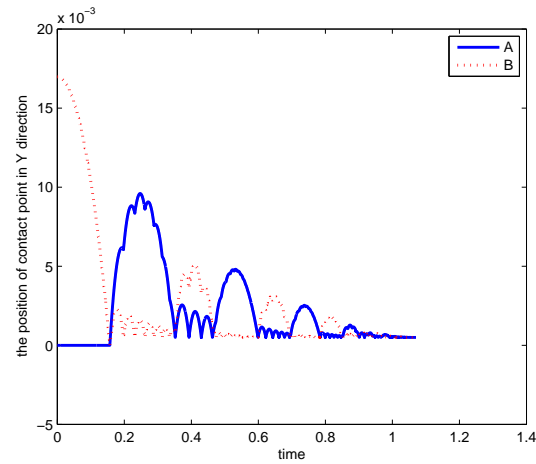
The numerical results of sections 4 and 5 prove that the LZB model is able to reproduce a rich set of dynamical behaviours, with a limited set of parameters *per* contact.

These simulation results also prove that the *kinetic angle* between the two constraint surfaces at a 2-impact, is a fundamental parameter which allows one to characterize the energy dispersion at the contact/impact points. A critical value of the kinetic angle (evolving from $\frac{\pi}{2}$ for $\frac{l}{L} = \sqrt{2}$ in the frictionless case to $\frac{\pi}{2.55}$ for $\frac{l}{L} = \frac{\sqrt{2}}{2}$ for high enough friction) is exhibited. This value allows one to split the planar blocks into two classes: flat and slender blocks, depending on $\frac{l}{L}$.

Despite the role of the kinetic angle for frictionless constraints has been identified since a long time in the literature on multiple impacts (in relation with the property of continuous dependence on initial conditions), its role when multi-valued Coulomb's friction is considered is less studied. This work and the study on the dimer's dynamics prove that even in the presence of friction some critical kinetic angles (equivalently, some critical aspect ratios) do exist. They may be quite useful to split the blocks into different classes which share the same dynamical properties.

6 Comparisons with free-rocking experimental data

In this section it is proved that the LZB model is easily fitted to provide correct predictions of free-rocking motions, with fixed base. Three different sets of experimental results are used, from [46], [29] and [17]. The comparisons with

(a) Horizontal velocity of A and B .(b) Vertical position of A and B .Figure 27: $e_{n,1}^* = e_{n,2}^* = 0.9$, $\mu_1 = \mu_2 = 0.01$, $\mu_{s,1} = \mu_{s,2} = 0.02$.

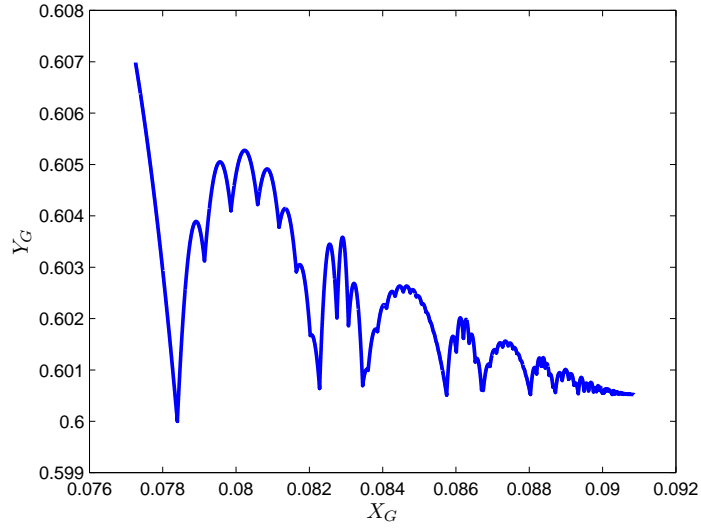


Figure 28: Trajectory of the mass center, with $e_{n,1}^* = e_{n,2}^* = 0.9$, $\mu_1 = \mu_2 = 0.01$, $\mu_{s,1} = \mu_{s,2} = 0.02$.

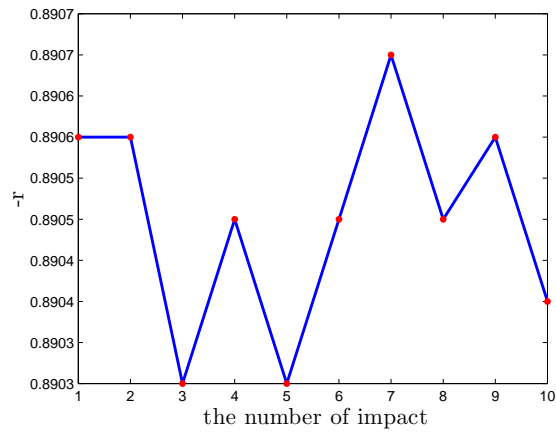


Figure 29: r as a function of the impact number, $e_{n,1}^* = e_{n,2}^* = 0.9$, $\mu_1 = \mu_2 = 0.3$, $\mu_{s,1} = \mu_{s,2} = 0.5$.

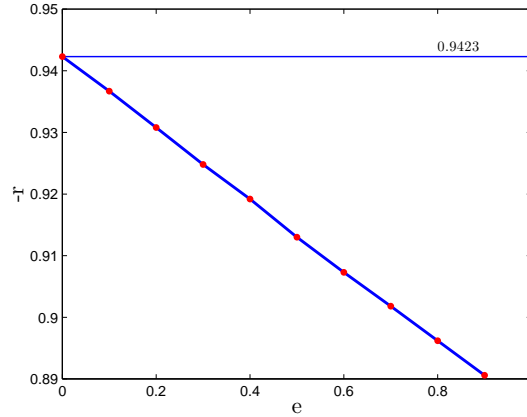


Figure 30: r as a function of e_n^* , $\mu_1 = \mu_2 = 0.3$, $\mu_{s,1} = \mu_{s,2} = 0.5$.

the data in [45, 46] are done from the accurate experimental data (not available in the papers but provided to us by the authors), whereas those with the data in [29] and [17] are made only from the figures available in the papers and are therefore less accurate and more qualitative.

6.1 Experimental data in Pena et al [46]

Experimental data led on blue granite stone blocks are reported in [46]. In this section we provide detailed comparisons between the numerical simulations obtained with the LZB model of section 3 and the experimental data of [46]³ The tests concern four specimens of blocks with ratios $\frac{l}{L} = \frac{1}{0.25} = 4$ and thickness $d = 0.754\text{m}$ (specimen 1), $\frac{1}{0.17} = 5.88$ and thickness $d = 0.502\text{m}$, (specimen 2), $\frac{1}{0.12} = 8.33$ and thickness $d = 0.375\text{m}$ (specimen 3), $\frac{0.457}{0.16} = 2.85$ and thickness $d = 0.750\text{m}$ (specimen 4), where l and L are in meters. Specimen 3 is the most slender one with the smallest thickness, and is of the *tower* type. Specimen 4 is the less slender one with the largest thickness and is of the *slice* type.

6.1.1 The $\theta(t)$ response

Let us now study the $\theta(t)$ response of the blocks. The results are depicted in figures 31, 32, 35, 37 for specimens 1, 2, 3 and 4 respectively. The corresponding responses $y_A(t)$ and $y_B(t)$ are in figures 33 and 34. The fitted parameters are $e_{n,i}^* = 0.999$ for specimen 2 in figure 32, and $e_{n,i}^* = 0.97$ for the first 10 impacts and $e_{n,i}^* = 0.88$ for the last impacts, for specimen 1 in figure 31. For specimen 4 the fitted values are $e_{n,i}^* = 0.99$ for the first 4 impacts, $e_{n,i}^* = 0.84$ between impact 5 and impact 8, and $e_{n,i}^* = 0.99$ for the last impacts. The fitted dimensions are $\frac{l}{L} = \frac{1}{0.23} \approx 4.35$ for specimen 1 and $\frac{l}{L} = \frac{1}{0.155} = 6.45$ for specimen 2, $\frac{l}{L} = \frac{0.457}{0.10} = 4.57$ for specimen 4. The results for specimen 3 are depicted in

³All the data corresponding to the comparisons presented in this section have been made available to us by Dr F. Pena from UNAM, Mexico. We have therefore been able to make accurate comparisons between the numerical and the experimental data.

| | 1 | 2 | 3 | 4 |
|------------------------------|--------|--------|--------------|--------|
| Geometric width | 0.24 | 0.16 | 0.11 | 0.15 |
| Experimental width | 0.2394 | 0.1645 | 0.1552 (3D) | 0.1255 |
| Width in simulations of [46] | 0.2468 | 0.1696 | 0.1196 | 0.1464 |
| Width in LZB model | 0.23 | 0.155 | 3D we do not | 0.10 |

Table 2: The various widths.

figures 35 and 36. In figure 35 the magnitudes of the oscillations are correctly predicted with the same restitution as for the fitted values of specimens 1 and 2, *i.e.* $e_{n,i}^* = 0.999$, however there is a shift in the oscillations pseudo-period. The parameters are varied in figure 36 with a smaller restitution coefficient and width, but this does not change much the result (see the comments below). The results for specimen 4 are in figure 37. In this case we had to switch e_n^* twice to obtain a good matching. In Tables 3 to 8 are reported some data on the impact times and the maximal amplitudes that correspond to the $\theta(t)$ responses for specimens 1, 2 and 4. All these results show that the LZB model has very good prediction capabilities. The large errors for specimen 4 in Table 8 are due to some imperfect measurement data at the peaks and should not be considered as significant results. This is visible in the figures 38 where few peaks are zoomed. Such issues are common in experimental data and do not call into question neither the experimental data from [45, 46] nor our comparison results.

Uncertainties in e_n^* It happens that the rocking motion is highly sensitive to parameters variations, which renders the calibration of the parameters a delicate process. In figure 40 (a) is depicted the $\theta(t)$ response for specimen 2, with $e_{n,i}^* = 0.95$, which represents a variation of 4.9% with respect to the fitted value $e_{n,i}^* = 0.999$ in figure 32. This $e_{n,i}^*$ value produces an error of 3% in the prediction of r , see figure 42 and the table 9. The same is done in figure 40 (b) with $e_{n,i}^* = 0.99$, which represents a variation of 1% with respect to the fitted value. It is apparent that a very small variation on $e_{n,i}^*$ produces a large mismatch in the $\theta(t)$ response. This means that the relative errors on the computed values of r as in figure 42 cannot be used as a criteria to decide whether or not a model is good, because very small variations on the restitution produce unacceptable errors in the time response.

Uncertainties in the width L The sensitivity of the $\theta(t)$ response w.r.t. variations in $\frac{l}{L}$ is shown in figure 41 (a) for specimen 2, and in figure 41 (b) for specimen 4. The values for $e_{n,i}^*$ are the fitted ones. It follows that the uncertainty in the width L affects mainly the pseudo frequency of the oscillations and has little effect on the magnitudes. This is in contrast with uncertainties on $e_{n,i}^*$ which affect both the frequency and the magnitude, see figure 40 (a). The various widths which enter the study are recapitulated in Table 2. The geometric widths are those measured on the blocks. The experimental widths are obtained from an estimation process, see section 4.1 in [45]. The other two sets of widths are obtained by the fitting the parameters.

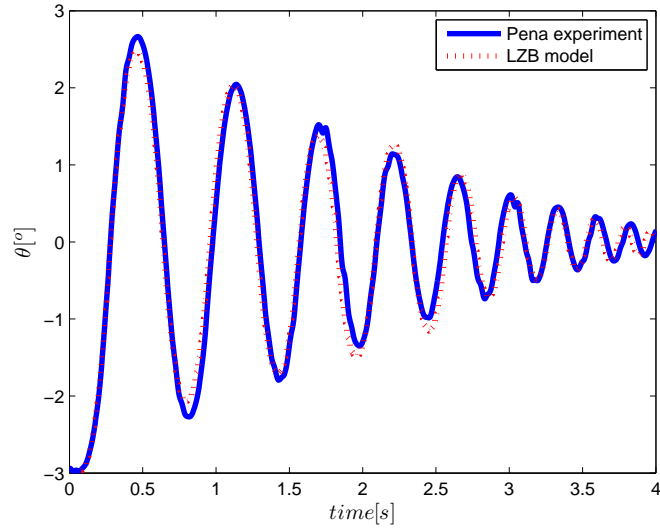


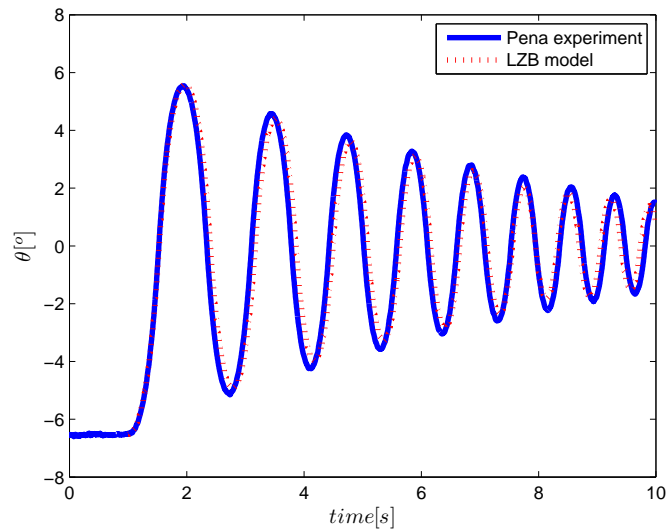
Figure 31: Numerical vs experimental values of $\theta(t)$, specimen 1. $e_n^* = 0.97$ and 0.88 , $l = 1\text{m}$, $L = 0.23\text{m}$.

| Impact no | Experiment IT (s) | Numerical IT (s) | Absolute error | Relative error in % |
|-----------|-------------------|------------------|----------------|---------------------|
| 1 | 0.279 | 0.279 | 0 | 0 |
| 2 | 0.647 | 0.637 | 0.01 | 1.5 |
| 3 | 0.977 | 0.958 | 0.019 | 1.94 |
| 4 | 1.293 | 1.278 | 0.015 | 1.16 |
| 5 | 1.578 | 1.567 | 0.011 | 0.70 |
| 6 | 1.855 | 1.825 | 0.03 | 1.62 |
| 7 | 2.097 | 2.092 | 0.005 | 0.24 |
| 8 | 2.336 | 2.334 | 0.002 | 0.09 |
| 9 | 2.570 | 2.545 | 0.025 | 0.97 |
| 10 | 2.745 | 2.770 | 0.025 | 0.97 |
| 11 | 2.928 | 2.956 | 0.028 | 0.96 |
| 12 | 3.104 | 3.114 | 0.01 | 0.32 |
| 13 | 3.256 | 3.262 | 0.006 | 0.18 |
| 14 | 3.406 | 3.399 | 0.007 | 0.20 |
| 15 | 3.538 | 3.526 | 0.012 | 0.34 |
| 16 | 3.665 | 3.641 | 0.024 | 0.65 |

Table 3: The data of figure 31, specimen 1, impact times (IT).

| Peak no | Experiment MA | Numerical MA | absolute error | Relative error in % |
|---------|---------------|--------------|----------------|---------------------|
| 1 | -2.968 | -2.968 | 0 | 0 |
| 2 | 2.666 | 2.472 | 0.194 | 7.28 |
| 3 | -2.271 | -2.076 | 0.195 | 8.59 |
| 4 | 2.045 | 2.032 | 0.013 | 0.64 |
| 5 | -1.794 | -1.711 | 0.083 | 4.63 |
| 6 | 1.521 | 1.381 | 0.14 | 9.21 |
| 7 | -1.352 | -1.497 | 0.145 | 10.72 |
| 8 | 1.267 | 1.142 | 0.125 | 9.87 |
| 9 | -0.986 | -1.158 | 0.172 | 17.44 |
| 10 | 0.846 | 0.885 | 0.039 | 4.6 |
| 11 | -0.738 | -0.716 | 0.022 | 2.98 |
| 12 | 0.613 | 0.575 | 0.038 | 6.20 |
| 13 | -0.504 | -0.491 | 0.013 | 2.58 |
| 14 | 0.452 | 0.419 | 0.033 | 7.30 |
| 15 | -0.363 | -0.358 | 0.005 | 1.38 |
| 16 | 0.325 | 0.297 | 0.028 | 8.62 |

Table 4: The data of figure 31, specimen 1, maximum amplitudes (MA).

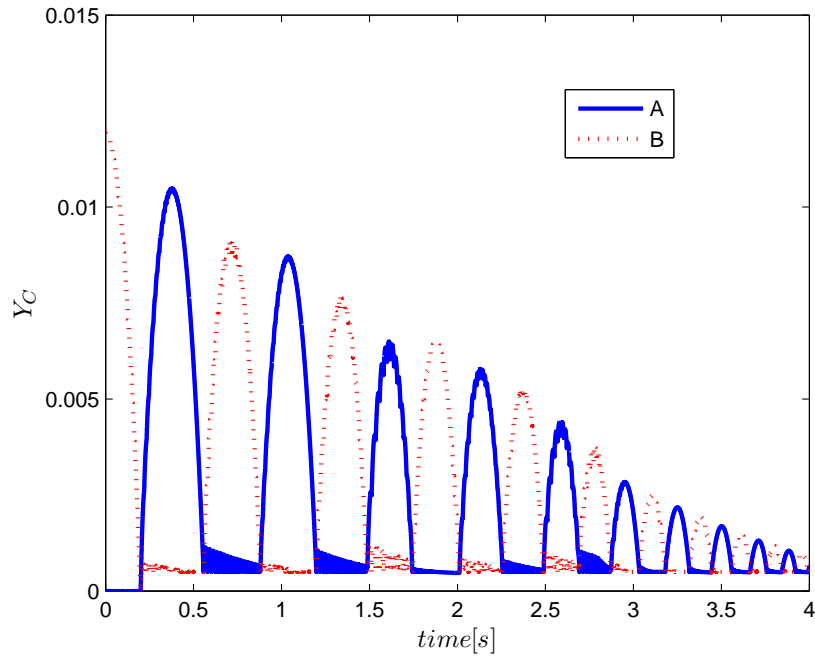
Figure 32: Numerical vs experimental values of $\theta(t)$, specimen 2. $e_n^* = 0.999$, $l = 1\text{m}$, $L = 0.155\text{m}$.

| Impact no | Experiment IT (s) | Numerical IT (s) | Absolute error | Relative error in % |
|-----------|-------------------|------------------|----------------|---------------------|
| 1 | 1.525 | 1.531 | -0.006 | 0.39 |
| 2 | 2.347 | 2.442 | -0.095 | 4.05 |
| 3 | 3.108 | 3.171 | -0.063 | 2.03 |
| 4 | 3.785 | 3.861 | -0.076 | 2.01 |
| 5 | 4.431 | 4.493 | -0.062 | 1.40 |
| 6 | 5.019 | 5.082 | -0.063 | 1.26 |
| 7 | 5.585 | 5.632 | -0.047 | 0.84 |
| 8 | 6.105 | 6.158 | -0.053 | 0.87 |
| 9 | 6.605 | 6.657 | -0.052 | 0.79 |
| 10 | 7.075 | 7.119 | -0.044 | 0.62 |
| 11 | 7.525 | 7.555 | -0.03 | 0.40 |
| 12 | 7.952 | 7.947 | 0.005 | 0.06 |
| 13 | 8.362 | 8.323 | 0.039 | 0.47 |
| 14 | 8.745 | 8.695 | 0.05 | 0.57 |
| 15 | 9.123 | 9.061 | 0.062 | 0.68 |
| 16 | 9.477 | 9.408 | 0.069 | 0.73 |

Table 5: The data of figure 32, specimen 2, impact times (IT).

| Peak no | Experiment MA | Numerical MA | absolute error | Relative error in % |
|---------|---------------|--------------|----------------|---------------------|
| 1 | -6.516 | -6.520 | -0.004 | 0.06 |
| 2 | 5.582 | 5.542 | 0.04 | 0.72 |
| 3 | -5.152 | -4.925 | 0.227 | 4.41 |
| 4 | 4.574 | 4.404 | 0.17 | 3.72 |
| 5 | -4.241 | -3.962 | 0.279 | 6.58 |
| 6 | 3.846 | 3.626 | 0.22 | 5.72 |
| 7 | -3.574 | -3.299 | 0.275 | 7.69 |
| 8 | 3.280 | 3.111 | 0.169 | 5.15 |
| 9 | -3.046 | -2.843 | 0.203 | 6.66 |
| 10 | 2.801 | 2.605 | 0.196 | 7.00 |
| 11 | -2.593 | -2.342 | 0.251 | 9.68 |
| 12 | 2.384 | 2.013 | 0.371 | 15.56 |
| 13 | -2.237 | -1.825 | 0.412 | 18.42 |
| 14 | 2.031 | 1.841 | 0.19 | 9.35 |
| 15 | -1.926 | -1.768 | 0.158 | 8.20 |
| 16 | 1.758 | 1.631 | 0.127 | 7.22 |

Table 6: The data of figure 32, specimen 2, maximum amplitudes (MA).

Figure 33: Numerical values of $y_C(t)$, specimen 1.

| Impact no | Experiment IT (s) | Numerical IT (s) | Absolute error | Relative error in % |
|-----------|-------------------|------------------|----------------|---------------------|
| 1 | 0.199s | 0.195s | 0.004 | 2.01 |
| 2 | 0.403 | 0.406 | -0.003 | 0.74 |
| 3 | 0.592 | 0.599 | 0.007 | 1.18 |
| 4 | 0.764 | 0.776 | -0.012 | 1.55 |
| 5 | 0.925 | 0.937 | -0.012 | 1.30 |
| 6 | 1.070 | 1.081 | -0.011 | 1.03 |
| 7 | 1.208 | 1.213 | -0.005 | 0.41 |
| 8 | 1.333 | 1.335 | -0.002 | 0.15 |
| 9 | 1.449 | 1.446 | 0.003 | 0.21 |
| 10 | 1.556 | 1.548 | 0.008 | 0.51 |
| 11 | 1.659 | 1.643 | 0.016 | 0.96 |
| 12 | 1.751 | 1.741 | 0.01 | 0.57 |
| 13 | 1.841 | 1.831 | 0.01 | 0.54 |
| 14 | 1.921 | 1.924 | -0.003 | 0.16 |

Table 7: The data of figure 37, specimen 4, impact times (IT).

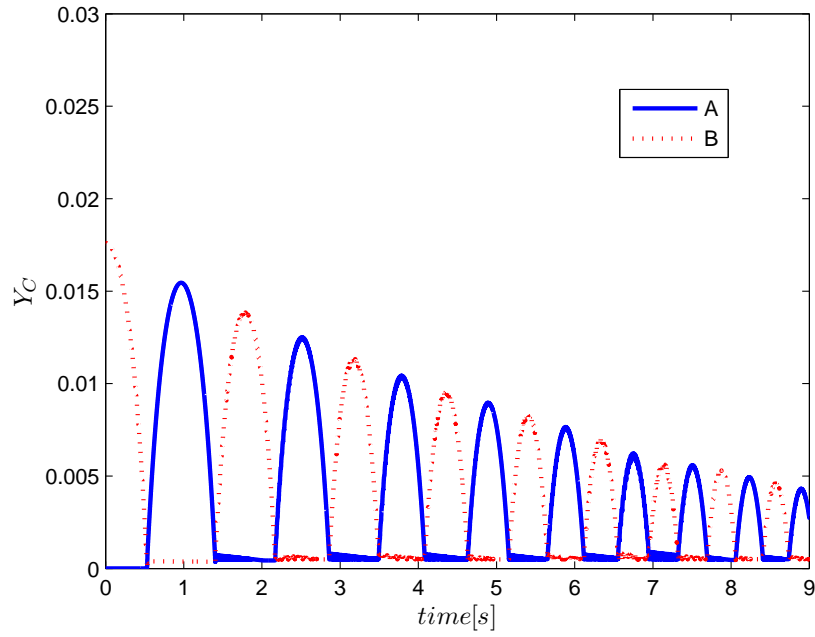


Figure 34: Numerical values of $y_C(t)$, specimen 2.

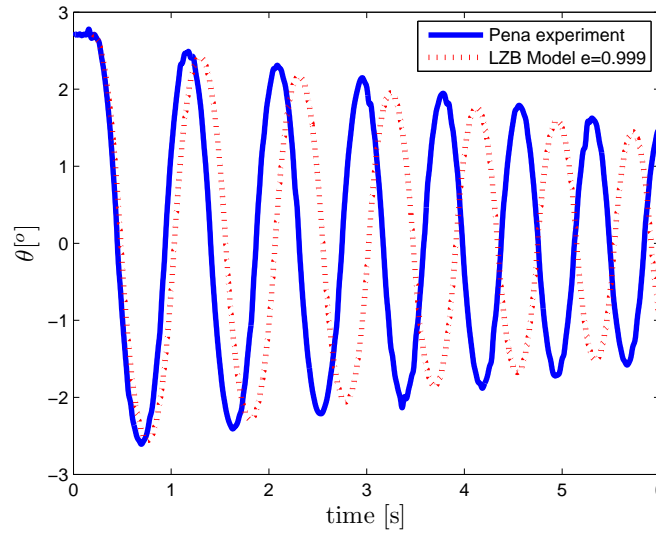


Figure 35: Numerical vs experimental values of $\theta(t)$, specimen 3, $e_{n,i}^* = 0.999$, $l = 1\text{m}$, $L = 0.12\text{m}$.

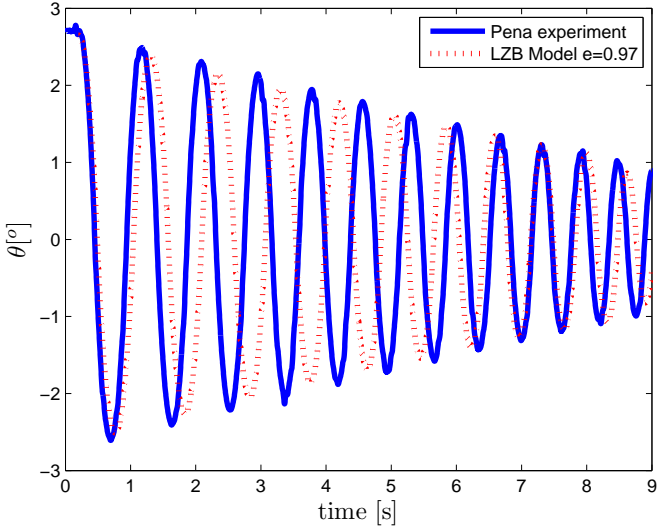


Figure 36: Numerical vs experimental values of $\theta(t)$, specimen 3, $e_{n,i}^* = 0.97$, $l = 1\text{m}$, $L = 0.115\text{m}$.

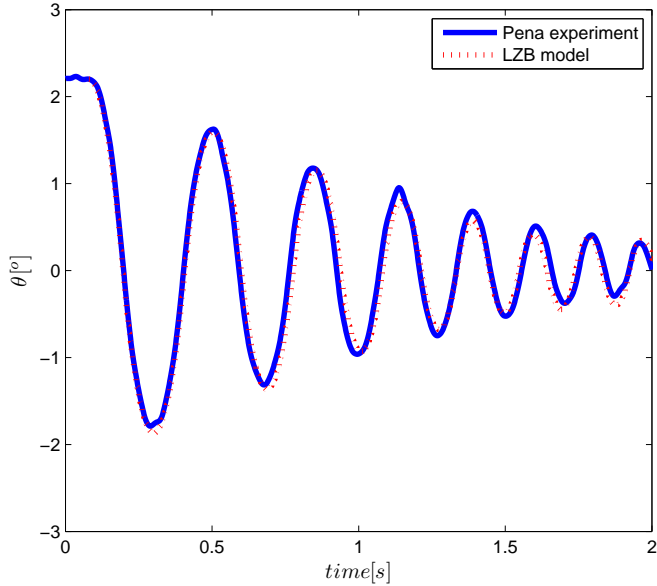
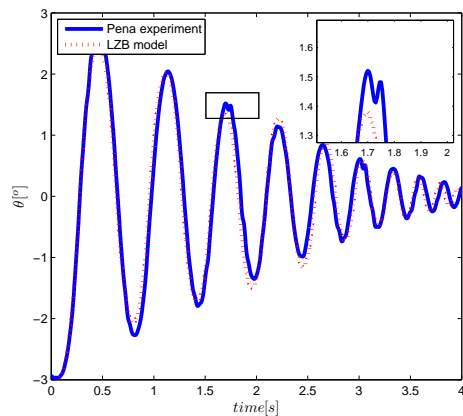
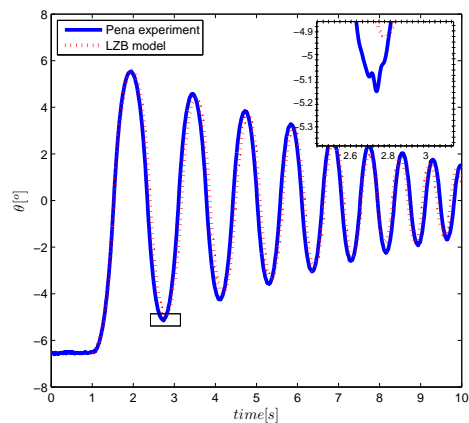


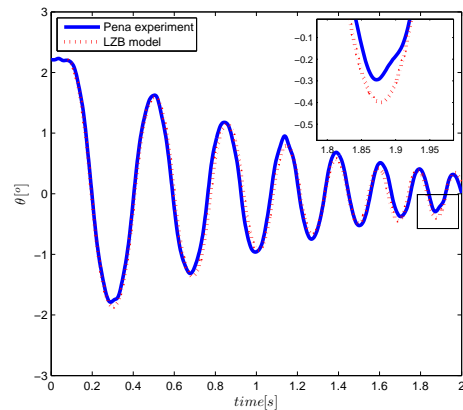
Figure 37: Numerical vs experimental values of $\theta(t)$, specimen 4, $e_{n,i}^* = 0.99$, and 0.84 , $l = 0.457\text{m}$, $L = 0.10\text{m}$.



(a) Specimen 1



(b) Specimen 2



(c) Specimen 4

Figure 38: Zooms on the $\theta(t)$ response.

| Peak no | Experiment MA | Numerical MA | absolute error | Relative error in % |
|---------|---------------|--------------|----------------|---------------------|
| 1 | 2.201 | 2.200 | 0.001 | 0.04 |
| 2 | -1.789 | -1.869 | -0.08 | 4.47 |
| 3 | 1.626 | 1.594 | 0.032 | 1.97 |
| 4 | -1.315 | -1.363 | -0.048 | 3.65 |
| 5 | 1.178 | 1.155 | 0.023 | 1.95 |
| 6 | -0.962 | -0.932 | 0.03 | 3.12 |
| 7 | 0.953 | 0.794 | 0.159 | 16.68 |
| 8 | -0.749 | -0.675 | 0.074 | 9.88 |
| 9 | 0.682 | 0.572 | 0.11 | 16.13 |
| 10 | -0.525 | -0.485 | 0.04 | 7.62 |
| 11 | 0.512 | 0.421 | 0.091 | 17.77 |
| 12 | -0.376 | -0.447 | -0.071 | 18.88 |
| 13 | 0.408 | 0.385 | 0.023 | 5.63 |
| 14 | -0.295 | -0.399 | -0.104 | 35.25 |

Table 8: The data of figure 37, specimen 4, maximum amplitudes (MA).

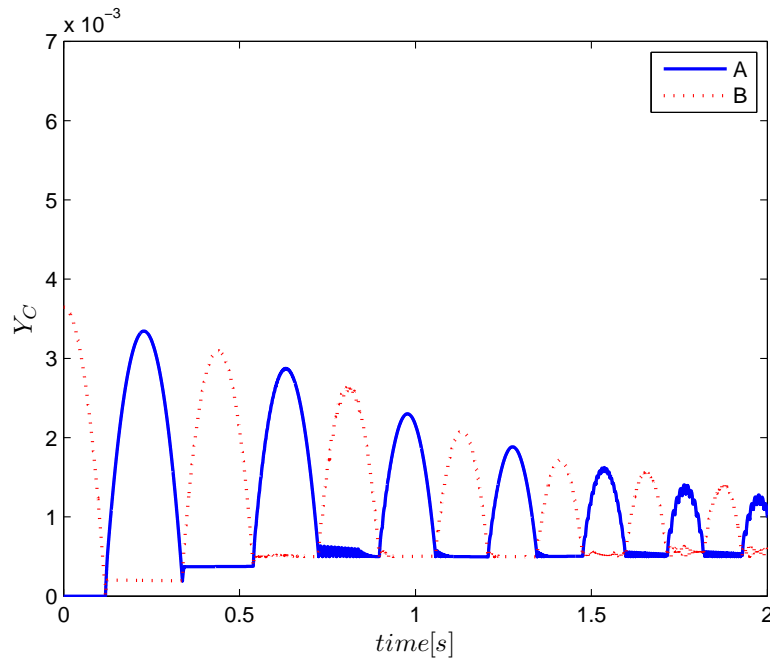
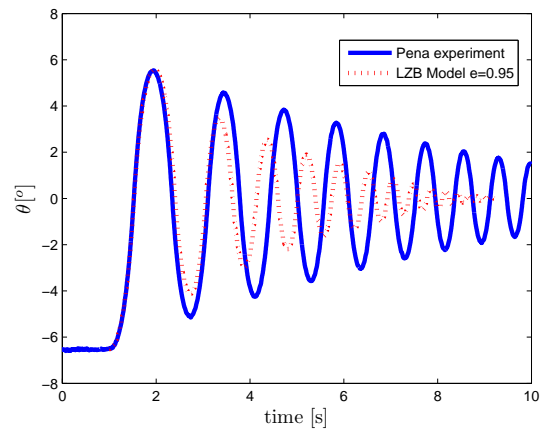
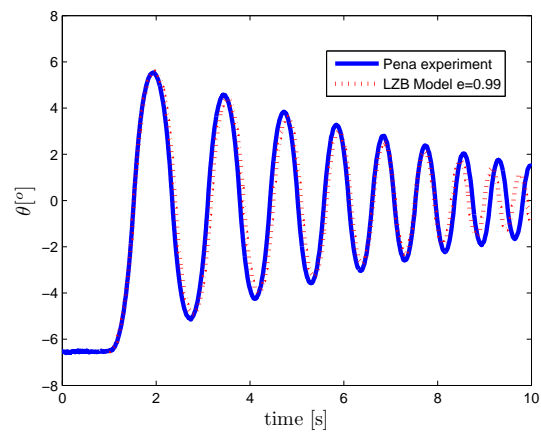
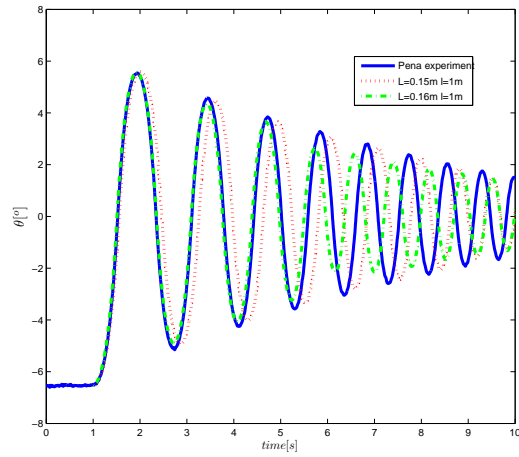
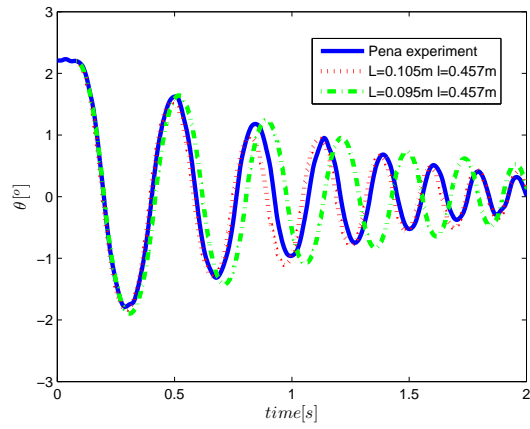


Figure 39: Numerical values of $y_C(t)$, specimen 4.

(a) $e_{n,i}^* = 0.95$ (b) $e_{n,i}^* = 0.99$ Figure 40: Sensitivity of the $\theta(t)$ response w.r.t. variations in $e_{n,i}^*$ (specimen 2).



(a) Specimen 2



(b) Specimen 4

Figure 41: Sensitivity of the $\theta(t)$ response w.r.t. variations in L .

6.1.2 The angular velocity restitution coefficient

We deal here with the free rocking block experiments reported in section 4 of [46]. Let us start with Table 3 in [46] where experimentally measured values of a kinematic angular restitution coefficient, denoted as μ in [46] and next as r_{exp} to avoid confusions, are reported from the free-rocking of the above four specimens of blocks. In [46] r_{exp} is computed indirectly from the averaged values of the expressions:

$$\left(\frac{\cos(\alpha - a_n) - \cos(\alpha)}{\cos(\alpha - a_0) - \cos(\alpha)} \right)^{\frac{1}{2n}} \quad (42)$$

where the a_n are the magnitudes of the block's orientation $\theta(t)$, n is the impact number. This expression is deduced from the energy at the n th impact as a function of the initial energy and r . This is also used in [17] to compute the energy of various rocking blocks (figures 15, 16, 17 in [17]). We shall use this way of computing r in figures 42, 43, 44, 45 and 46. The angular restitution r is calculated directly from the ratios $\frac{\dot{\theta}(t^+)}{\dot{\theta}(t^-)}$ in figures 43 (b), 44 (b), 45 (b). The latter are not available from the experimental data, but only from our numerical simulations with the LZB model in the previous section. However since they are calculated with the fitted parameters the computed values should be close to the experimental ones.

As we have seen above (see figure 29) it may be expected that r varies very little from one impact to the next during a rocking motion. Choosing the parameters indicated in [46] for specimens 1, 2, 3 and doing the same calculations enables us to compute an r_{LZB} (denoted as LZB model in figure 42) that compares with r_{exp} . The results are reported in figure 42 for the three specimens of blocks studied in [46]. The numerical results have been obtained by setting different values for $e_{n,i}^*$, $\mu = 0.3$ and $\mu_s = 0.5$ (the experimental value being $\mu_s = 0.577$) and the masses indicated in [46]: $m \approx 503, 228, 120$ kg respectively⁴. The LZB model provides a good estimation of r_{exp} , the relative errors being reported in the table 9. In figure 46 are depicted the values of r_{exp} and r_{LZB} computed with the parameters fitted so that the experimental and numerical $\theta(t)$ curves match⁵: the values for r_{LZB} and r_{exp} are almost equal. In figures 43 (a), 44 and 45 are depicted the values of r_{LZB} and r_{exp} with the fitted parameters. It is seen that r is almost constant from one impact to the next. The first values of r_{exp} and r_{LZB} may be smaller than the other ones: this is explained by the absence of a rebound phase after the first impact, see figure 34, 39. In figures 43 (b), 44 (b), 45 (b) are depicted the values of $-r = \frac{\dot{\theta}(t^+)}{\dot{\theta}(t^-)}$, which differ from those of figures 43 (a), 44 and 45 which are computed as in [46]: they are less "smooth", in the sense that r varies more with some peaks. The variations however remain small for specimens 1 and 2 (less than 2%) and are more important for specimen 4 (about 6%), which is explained by the more important change in the fitted values for $e_{n,i}^*$ for specimen 4, where it had to be switched twice in figure 37.

⁴The masses are estimated from the density and the dimensions in [46], hence prone to some uncertainties.

⁵We call the fitted parameters the parameters used in figures 31, 32 and 37.

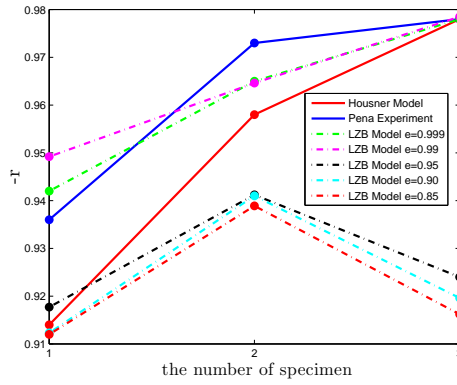
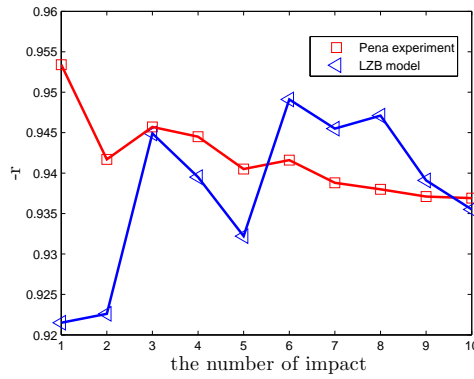
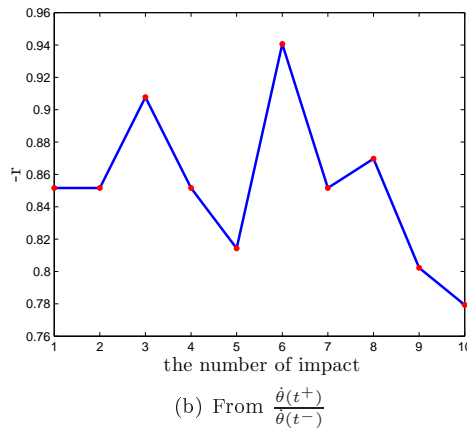


Figure 42: Numerical vs experimental values of the angular restitution coefficient.



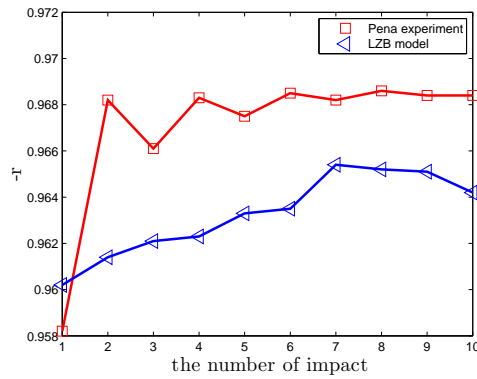
(a) From the estimation process.



(b) From $\frac{\dot{\theta}(t^+)}{\dot{\theta}(t^-)}$

Figure 43: Numerical and experimental values of the angular restitution coefficient (specimen 1 with fitted parameters).

| $e_{n,i}^*$ | 0.999 | 0.99 | 0.95 | 0.90 | 0.85 |
|---|---------|---------|--------|--------|--------|
| $\frac{r_{\text{exp}} - r_{\text{LZB}}}{r_{\text{exp}}}$ (specimen 1) | -0.64 % | -1.41 % | 1.96 % | 2.53 % | 2.56 % |
| $\frac{r_{\text{exp}} - r_{\text{LZB}}}{r_{\text{exp}}}$ (specimen 2) | 0.81 % | 0.86 % | 3.27 % | 3.29 % | 3.50 % |
| $\frac{r_{\text{exp}} - r_{\text{LZB}}}{r_{\text{exp}}}$ (specimen 3) | -0.07 % | -0.05 % | 5.52 % | 5.97 % | 6.31 % |
| $\frac{r_{\text{exp}} - r_{\text{LZB}}}{r_{\text{exp}}}$ (specimen 4) | -3.00 | -2.5 | -0.20 | 3.1 | 3.45 |

Table 9: Relative errors on r .

(a) From the estimation process.

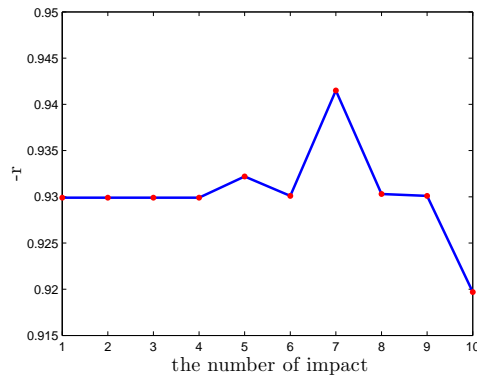
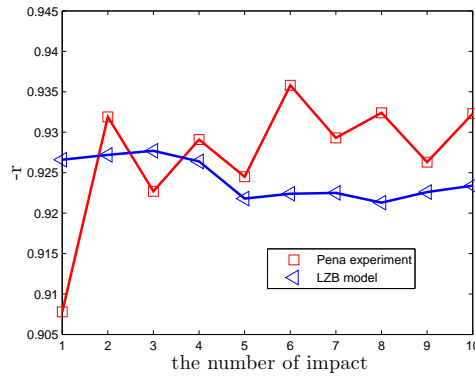
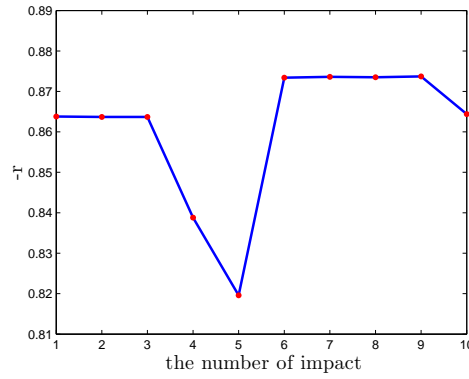
(b) From $\frac{\dot{\theta}(t^+)}{\dot{\theta}(t^-)}$

Figure 44: Numerical and experimental values of the angular restitution coefficient (specimen 2 with fitted parameters).



(a) From the estimation process.



(b) From $\frac{\dot{\theta}(t^+)}{\dot{\theta}(t^-)}$

Figure 45: Numerical and experimental values of the angular restitution coefficient (specimen 4 with fitted parameters).

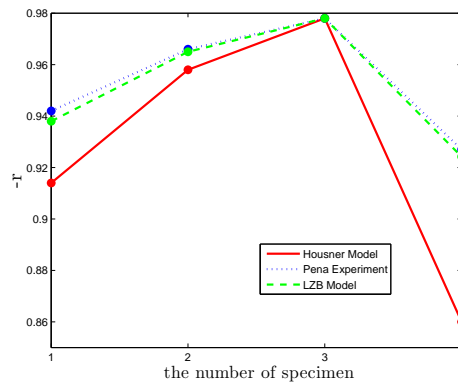


Figure 46: Numerical vs experimental values of the angular restitution coefficient (fitted parameters).

6.1.3 Comments

Some comments arise:

- The values for e_n^* (0.999 or 0.99) are large values, since other works on single granite/granite impacts without friction report values of the restitution coefficient ≈ 0.86 [24]. However it is also known from many experimental results that the restitution coefficient usually tends to 1 when the initial relative velocity tends to zero, see *e.g.* [60]. In the presented results the normal relative velocity is very small (about 0.02 m/s). This may explain this high value for e_n^* . This reinforces once again the apparent paradox that the kinematic model tends to represent rocking with $e_n = 0$, see remark 5. Recall that for specimen 2 the planar rocking assumption is well respected, where no three dimensional effects could be noticed experimentally in [46].
- The decrease of the fitted value for e_n^* for specimen 1 may be explained by some damage that has occurred on the contact points after the tenth impact ($t \approx 2.7s$), implying more dissipation. Indeed it is indicated in section 7 of [45, 46] that specimen 1 was damaged after the first tests. Since these experimental data are not ours we are unable to more accurately determine the source of this necessary variation of e_n^* . The same process of decreasing e_n^* has been necessary for specimen 4 in figure 37, which is of the slice type. It is possible that the line contact assumption is not perfectly satisfied experimentally due to the large thickness. Only a study on the impact force shape on the contact surface could bring an answer. But this is outside the scope of this study.
- The results in figures 41 are important because they directly relate to the uncertainty on the values of the width L (equivalently $\frac{l}{L}$ or the angle α) that may occur due to impact line or surface effects. These effects are in turn linked to the definition of the distance between the block and the ground, *i.e.* to the definition of the unilateral constraints, which are an essential ingredient in such a rigid body approach. This leads us to define different kinds of widths: the *geometric width* and the *effective width*. The geometric width is the block's width when the block is rectangular, *i.e.* L in figure 1. The effective width corresponds to the position of some equivalent contact points such that a block with a concave base would behave as the block with a line base. The geometric widths of the above four blocks are those reported in Table 2 of [46] and are 0.25 m, 0.17 m, 0.12 m and 0.16 m for specimens 1, 2, 3 and 4 respectively. The effective widths that we found by fitting the parameters are 0.23 m, 0.155 m, 0.115 m, and 0.10 m respectively. These widths can be equivalently expressed in terms of the critical angle α . One then finds the geometric values of α as ??, ??, ??, ?? for specimens 1, 2, 3, 4, and the effective values are ??, ??, ??, ?? . These values are to be compared with those given in Table 3 in [46] and [45]. In [46] the experimental value of the angle α is obtained from a minimization process whose entries are the times of the maximum amplitudes and the maximum amplitudes. The results are 0.235, 0.163, 0.154, 0.268 for specimens 1, 2, 3 and 4 respectively.

If however the rebound phases do not finish before the impact occurs at the other corner (like in figures 33 and 34 for specimens 1 and 2) then the line effect is irrelevant.

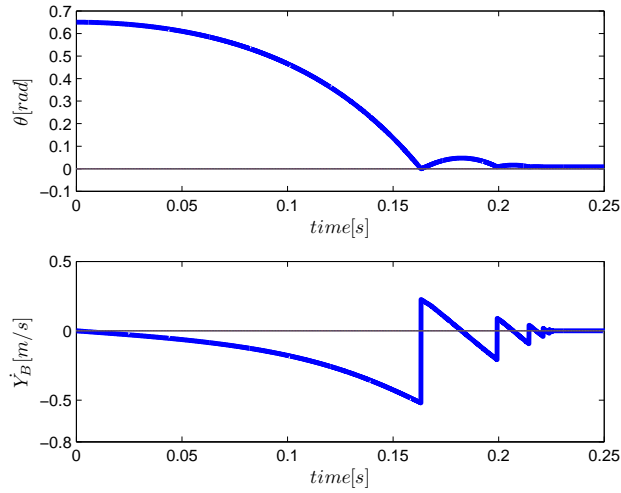
- It is somewhat surprising that there may be rocking without 2-impacts, if the rebound phases do not vanish like in figures 33 and 34.
- In all the simulated cases the friction coefficients (during and outside impacts) are such that the contact points are almost always sticking. This is in accordance with the experiments of [46] where no sliding was observed during the rocking motions. Therefore the energy loss may be tuned only with $e_{n,i}^*$. The important phenomenon is not the stick/slip behaviour but the existence of the rebound phases before the impacting corner stabilizes on the ground.
- It has been shown in [46] that specimen 3 that is of the tower-block type is prone to significant three dimensional effects like torsional effects and friction at the base. This explains why our planar model could not satisfactorily reproduce the experimental $\theta(t)$ response (figures 35 and 36).
- The fact that r is constant during the rocking motion means that a kinematic law like the one in section 2.3.4 (entry (3,3) in the table 1 of section 2.7) can be used, provided that $e_{n,21}(= -r)$ can be chosen within the required interval. However an important part of the dynamics like the rebound phases after the first impact, may be missed in many instances of slender blocks. We infer that this kinematic law does represent the rocking motion only when there is perfect sticking at impacts and outside impacts, and when the rebound phases vanish (such cases exist, see [29] with $\frac{l}{L} = 8$). We reiterate also that such a law does not permit to *predict* that such a particular motion will occur, it can just be fitted *a posteriori*.

6.2 Experimental data of Lipscombe et al [29]

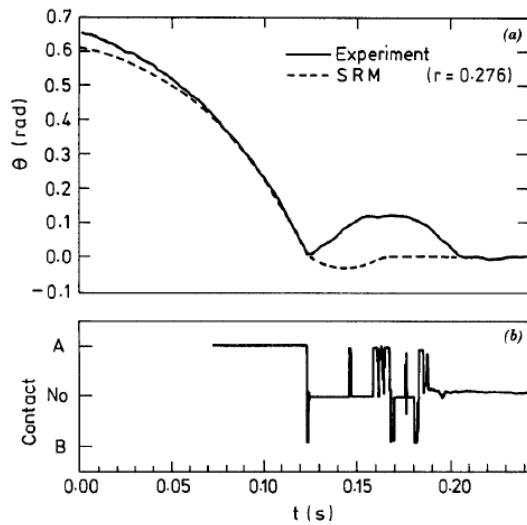
Other experimental data obtained with steel blocks/steel foundation are reported in [29], for $\frac{l}{L} = 1$ (specimen 1), 2 (specimen 2), 4 (specimen 3) and 8 (specimen 4). Figures 5, 6 and 7 in [29] show that “macroscopic” rocking occurs for $\frac{l}{L} = 2, 4$ and 8. However “perfect” rocking where the contact points stick after the shock, is obtained only for $\frac{l}{L} = 8$. For the other two values, the system becomes airborne after the first impact at B , then undergoes several impacts at B while still airborne. For $\frac{l}{L} = 4$ this sequence of impacts at B while airborne becomes much smaller, then disappears for $\frac{l}{L} = 8$. From a qualitative point of view, this indicates that perfect rocking occurs only for large enough $\frac{l}{L}$. This also confirms that the impact phases which are visible for instance in figures 23 (b), 33 and 34 do exist experimentally. Thanks to the small size of the blocks, values of $e_{n,i}^*$ have been measured and found to be close to 0.9 in [29]. However these values were measured in figure 11 of [29] for relative approach velocities within [0.1, 0.4] m/s, which may be too large values for rocking motions, especially when the energy has dissipated sufficiently. Thus we have to fit e_n^* once again. The fitted values are $e_n^* = 0.5$ for specimen 1, $e_n^* = 0.9$ for specimen 2, $e_n^* = 0.98$ for specimens 3 and 4. The numerical results are depicted in figures 47 (a), 48 (a), 49 (a) and 50 (a). The friction coefficients are $\mu = 0.16$ and $\mu_s = 1.3$

for the first three blocks, and $\mu = 0.13$ and $\mu_s = 0.28$ for the most slender block. The dashed curves in figures 47 (b), 50(b) and 49 (b) correspond to the simulations made in [29] with the so-called SRM (Simple Rocking Model). The SRM uses the Housner's angular velocity coefficient of restitution as in (26). Some comments arise:

- The qualitative behaviour of the four blocks dynamics is well reproduced.
 - Specimen 1 does not rock but performs half-rocking with two impacts before coming to rest, see figure 47. This is the only example of flat block we were able to find in the literature, with experimental data.
 - The rebounds phase occurs during the whole motion for specimen 1, then its duration decreases for specimens 2 and 3 until it vanishes for specimen 4, see figures 48, 49 and 50.
 - The impacts during the rebounds phases are well reproduced. For specimen 1 there is a first impact at B followed by rebound of B , then A detaches also from the ground and the block is airborne during a certain time. Then a series of impacts at B occurs again before complete rest (figures 47 (a) and 47 (b)). For specimen 2 the impacts at B are equally distributed during the rocking phase (figures 48 (a) and 48 (b)). For specimen 3 the rebound phase at B becomes shorter with more impacts concentrated on the right of the first impact time (figures 49 (a) and 49 (b)). For specimen 4 the rebound phases reduces to the first impact at B (figures 50 (a) and 50 (b)).
 - The possibility of predicting airborne phases is quite important in many applications and is one source of strong limitation of the basic Housner's approach with angular velocity restitution [66].
- The fitted values for e_n^* are in agreement with the experimental values provided in [29] which are close to 0.9, except for specimen 1 where a large discrepancy exists.
- Due to the lack of accuracy on the data provided in the upper parts of figures 5, 6, 7 in [29] which concern the long term $\theta(t)$ responses, it was impossible to get a matching between numerical and experimental data as good as the one in section 6.1 for the evolution of $\theta(t)$ over a long period. Consider for instance the upper figure 7 of [29], that is reproduced in figure 51 (a) for convenience. An initial angle $\theta(0) \approx 0.125$ rad is depicted, however this is larger than the critical angle α calculated from the dimensions which are given on page 1391 of [29]. There is consequently a strong mismatch between the data and the presented experimental results in that paper, which we cannot understand without having access to more informations. To be more concrete, we have even been unable to correctly simulate the block's motion before the first impact for specimens 2, 3 and 4 which rock, despite the dynamics on this period is simply that of an inverted pendulum. So the subsequent $\theta(t)$ responses were nonsense. The same is for the upper part of figure 6 in [29] which is reproduced in figure 51 (b). The simulations reported in [29] are the dashed curve of figure 51 (b) that is not initialized as the experimental system, indicating that there may have been significant uncertainties during the experiments. The fact



(a) simulation, $e_{n,i}^* = 0.5$, $l = 0.0458\text{m}$, $L = 0.0458\text{m}$.



● FIG. 4. Block with $h/b = 1$

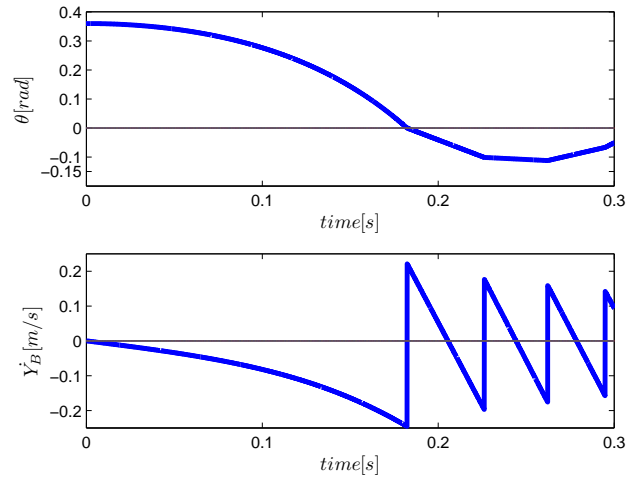
(b) figure 4 in [29].

Figure 47: Responses for specimen 1, $\frac{h}{L} = 1$.

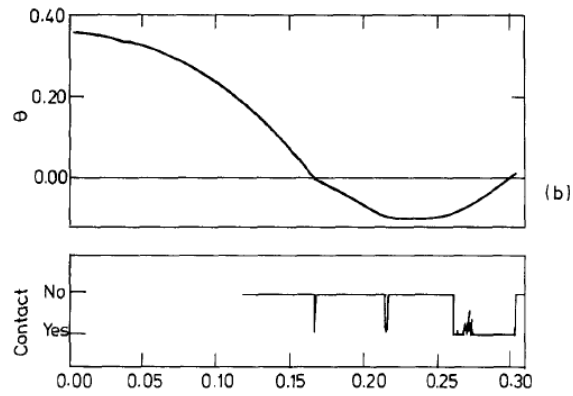
that we are able to qualitatively reproduce important phenomena is to be considered as the best results we could get.

6.3 Experimental data of Elgawady et al [17]

Experimental results led on different types of blocks impacting three types of grounds are reported in [17]. The comparisons are made with the concrete base

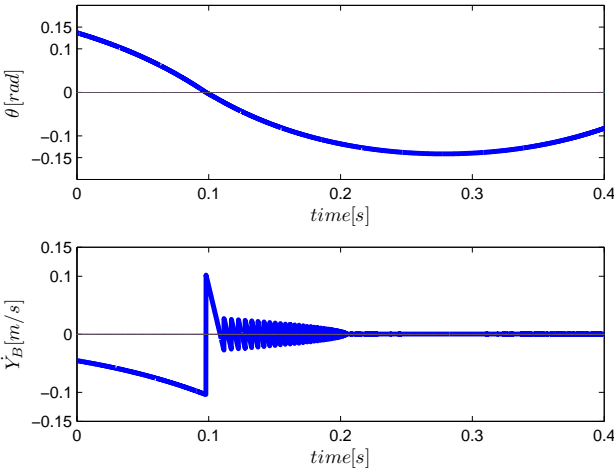


(a) simulation, $e_{n,i}^* = 0.9$, $l = 0.0916\text{m}$, $L = 0.0458\text{m}$.

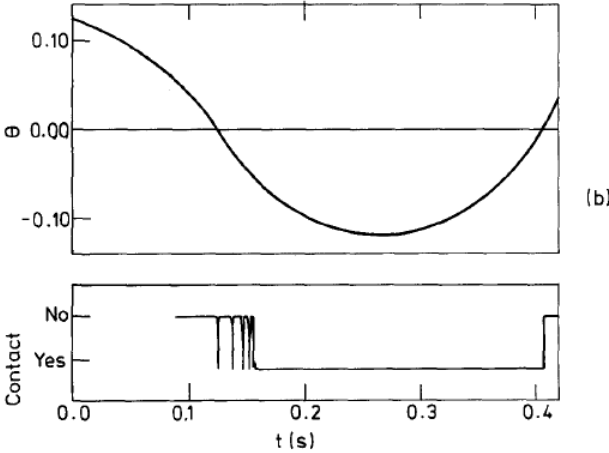


(b) figure 5 in [29].

Figure 48: Responses for specimen 2, $\frac{l}{L} = 2$.

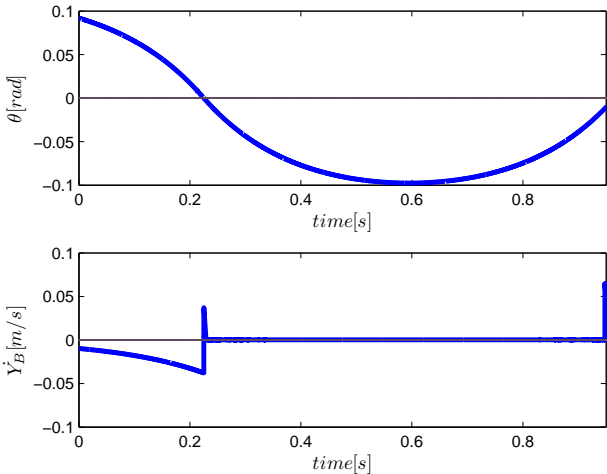


(a) simulation, $e_{n,i}^* = 0.98$, $l = 0.2032\text{m}$, $L = 0.0508\text{m}$.

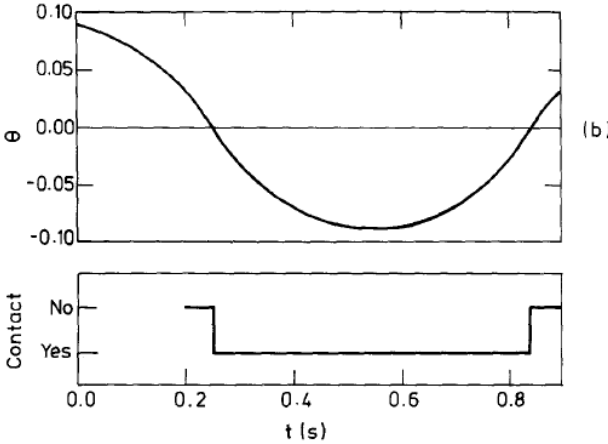


(b) figure 6 in [29].

Figure 49: Responses for specimen 3, $\frac{l}{L} = 4$.

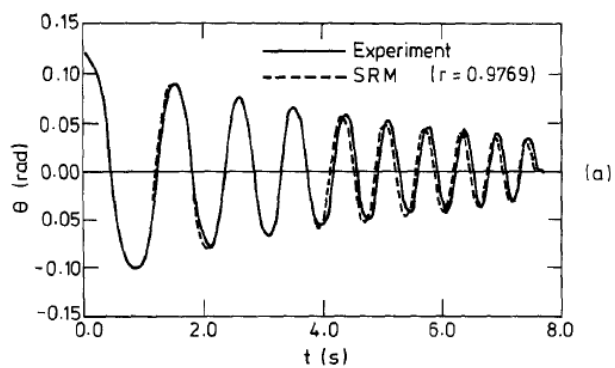


(a) simulation, $e_{n,i}^* = 0.98$, $l = 0.4064\text{m}$, $L = 0.0508\text{m}$.

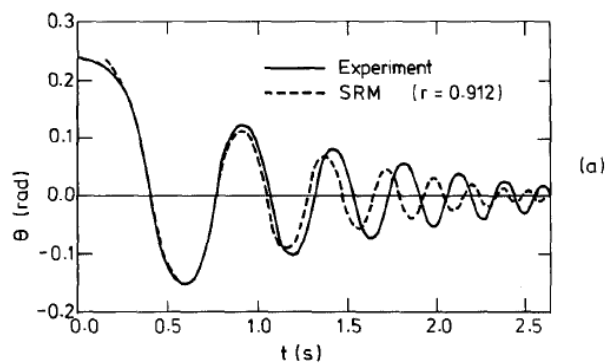


(b) figure 7 in [29].

Figure 50: Responses for specimen 4, $\frac{l}{L} = 8$.



(a) Figure 7 in [29]



(b) Figure 6 in [29].

Figure 51: Responses for specimens 4 and 3 in [29].

material AR3-C and AR5-C (see Table I in [17]). The friction coefficients are $\mu = 0.3$ and $\mu_s = 0.577$ (same choice as in section 6.1 which guarantee no sliding during the impacts and outside the impacts). The specimen AR3-C has $\frac{l}{L} = 3$ and the specimen AR5-C has $\frac{l}{L} = 5$, so they are slender blocks. The values used in the simulations are indicated in the figures. The responses are given for $\Phi(t) = \frac{\theta(t)}{\alpha}$. The results are depicted in figures 52 to 55. It is important to note that contrarily to the experiments in [46] that were led with blocks free to slide on the base, in [17] a special mechanism with rollers and pin joints fixed to the base has been implemented on the blocks to prevent sliding. This mechanism also secures that there are no three dimensional effects. In figures 56 (a) (b) and 56 (c) (d) are depicted the values of r obtained from the simulations. In tables 10 to 16 are reported some data obtained from the corresponding figures in [17]. They are of course approximated values. Some comments arise:

- The results have been obtained with $e_{n,i}^* = 0.8$. The matching between the experimental and the numerical results is quite good, except for AR5-C with initial angle $\theta(0) = 0.5$ rad in figure 52. For this specimen and initial angle, the LZB predicts too large magnitudes (see table 10), and too low frequency of the oscillations. We have not been able to understand the reason why.
- It is noteworthy that two different initial angles $\theta(0)$ are tested, and that the same parameters (restitution and friction) have been used for both. This confirms that the LZB model, despite it is a rigid body approach, supersedes kinematic laws where the parameters usually depend on the initial data. The approximated numerical values that correspond to each figure 52 to 55 are reported in the tables 10, 11, 12 and 13, respectively, for the maximum magnitudes.
- The matching for the pseudo-frequency of the oscillations is quite good except for the specimen AR5-C with $\theta(0) = 0.5$ rad. In particular one sees that the stabilisation times are well predicted by the LZB model in each case. The matching for the oscillations magnitudes is good in all cases. The results are reported in tables 14, 15 and 16 with the impact times. For specimen AR5-C in figure 52 the LZB model predicts 11 impacts before $t = 4$ s, and the experiments indicate 14 impacts; for specimen AR3-C in figure 53 the LZB model predicts 11 impacts before $t = 2$ s, and the experiments indicate 12 impacts; for specimen AR5-C in figure 54 the LZB model predicts 14 impacts before $t = 3$ s, and the experiments indicate 14 impacts; for specimen AR5-C in figure 52 the LZB model predicts 10 impacts before $t = 1.4$ s, and the experiments indicate 11 impacts.
- From figures 56 (a) (b) and 56 (c) (d) it follows that r is almost constant along the rocking oscillations, as noticed previously with other test cases. This confirms that if one knows in advance that rocking occurs, then the kinematic restitution law of section 2.3.4 can be used. The averaged numerical values for the specimen AR5-C are computed as $r = 0.8921$ (figure 56 (a)) and $r = 0.8916$ (figure 56 (c)). The averaged values for the specimen AR3-C are $r = 0.7294$ (figures 56 (b) and 56 (d)). The ratios $\frac{r}{r_H}$ where r_H is the Housner angular restitution coefficient in (26) are $\frac{r}{r_H} = 0.9467$ and $\frac{r}{r_H} = 0.9462$ for specimen AR5-C, and $\frac{r}{r_H} = 0.8581$

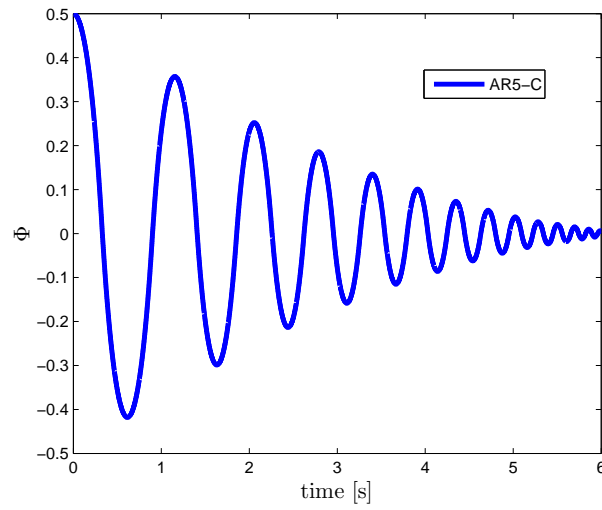
| Peak number | LZB model | Experiments |
|-------------|-----------|-------------|
| 1 | -0.42 | -0.38 |
| 2 | 0.35 | 0.30 |
| 3 | -0.30 | -0.25 |
| 4 | 0.25 | 0.20 |
| 5 | -0.20 | -0.16 |
| 6 | 0.19 | 0.12 |
| 7 | -0.16 | -0.11 |
| 8 | 0.12 | 0.9 |

Table 10: Peak magnitudes, figure 52.

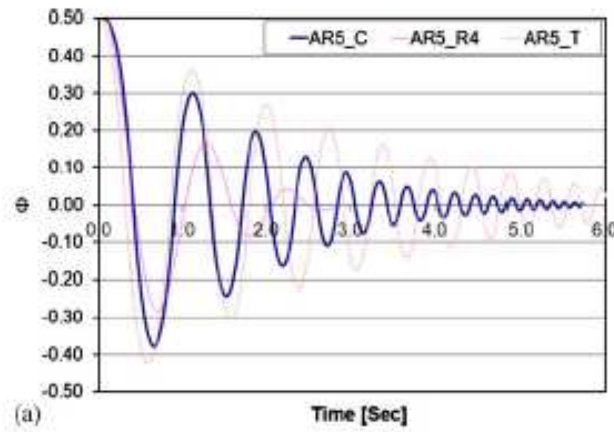
for specimen AR3-C ⁶. In Table II in [17] it is reported the values 0.975 for specimen AR5-C and 0.981 for specimen AR3-C. We infer that the experimental and LZB numerical values are in good matching, in view of the fact that the experimental values are prone to uncertainties and are themselves averaged values over several sets of experiments.

- The figure 57 is a copy of figure 18 (b) in [17]. It compares the results obtained with the kinematic law using the angular restitution coefficient r in (26) (denoted as SRM), with the results obtained with $0.975r$ (denoted as $r = 0.975r_H$), and the experimental results for specimen AR5-C (same experimental results as in figure 52 (b)). The Housner coefficient provides very bad results, and the corrected Housner coefficient is better with comparable results to those of figure 52 with the LZB model. In view of the fact that when perfect sticking occurs r is almost constant along the $\theta(t)$ response, this result is expected. It is however noteworthy that we also could not match the experiments reported in figure 52 (b).
- It follows from the kinematic law analysis that the Housner coefficient of restitution $|r_H| = \frac{2l^2 - L^2}{2L^2 + 2l^2}$ is not the most dissipative one in case of slender blocks with $l \geq \sqrt{2}L$, see section 2.3.4 and entry (3,3) in the table of section 2.7. Interestingly it has been shown in [17] on a test case with $\frac{l}{L} = 5$, named AR5-R4 in Table I in [17], that r_H does not dissipate enough energy to correctly predict the AR5-R4 block's rocking motion, see figure 18 (a) and figure 19 (b) in [17]. This specimen is a masonry block impacting a rubber surface. The most dissipative kinematic coefficient is equal to $e_{n,21} = |r| = \frac{l^2 - 2L^2}{4L^2 + l^2} = 0.7931$ with $\frac{l}{L} = 5$, whereas $r_H = 0.9423$ (see figure 30). Therefore $r = 0.84166r_H$, that is strictly larger than the value chosen in [17] $r = 0.815r_H$ for the computations of figure 18 (a) and 19 (b) in that paper. Relying on the data in figure 30 it follows that the minimum value of r which the LZB model is able to predict with the chosen friction is $r = 0.89$. It is inferred that the energy dissipated by the rubber, associated to an hysteretic deformation, cannot be handled by our impact model.

⁶ $r_H = 0.9423$ for specimen AR5-C with $\frac{l}{L} = 5$ and $r_H = 0.8581$ for specimen AR3-C with $\frac{l}{L} = 3$.



(a) simulation, $e_{n,i}^* = 0.8$, $l = 4.9L$, $L = 0.19\text{m}$.

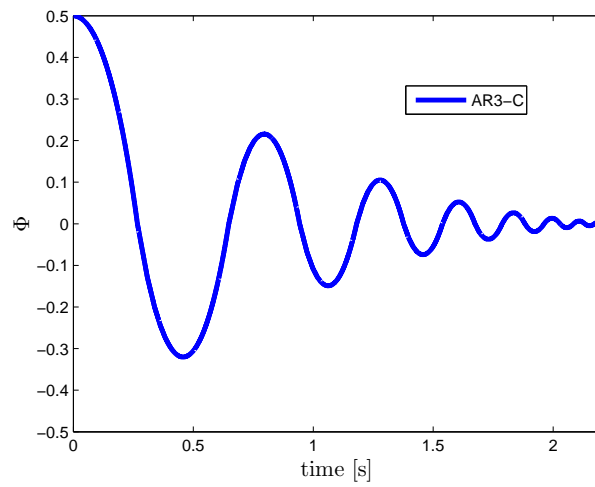


(b) figure 9 (a) in [17].

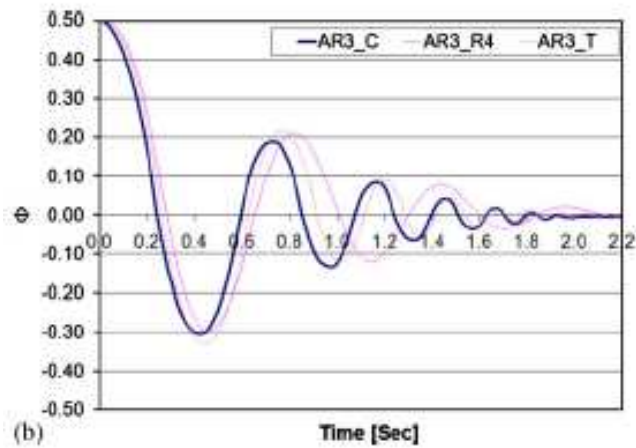
Figure 52: Responses for specimen AR5-C.

| Peak number | LZB model | Experiments |
|-------------|-----------|-------------|
| 1 | -0.31 | -0.30 |
| 2 | 0.20 | 0.19 |
| 3 | -0.15 | -0.13 |
| 4 | 0.10 | 0.08 |
| 5 | -0.08 | -0.07 |
| 6 | 0.05 | 0.045 |

Table 11: Peak magnitudes, figure 53.

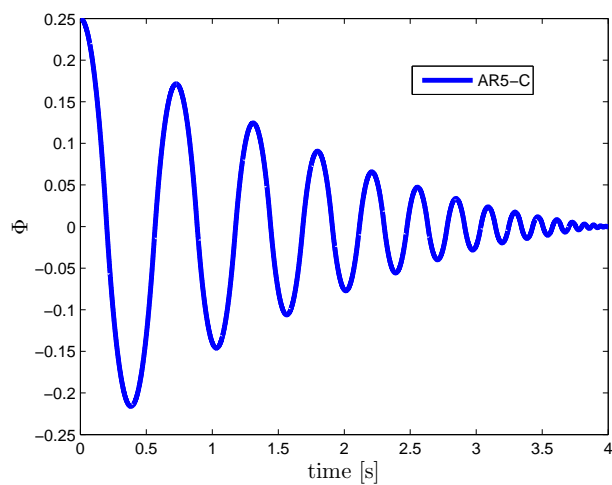


(a) simulation, $e_{n,i}^* = 0.8$, $l = 3L$, $L = 0.19$ m.

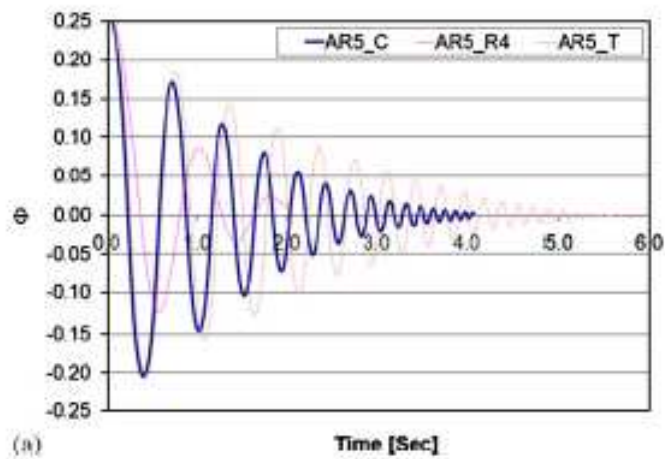


(b) figure 9 (b) in [17].

Figure 53: Responses for specimen AR3-C.

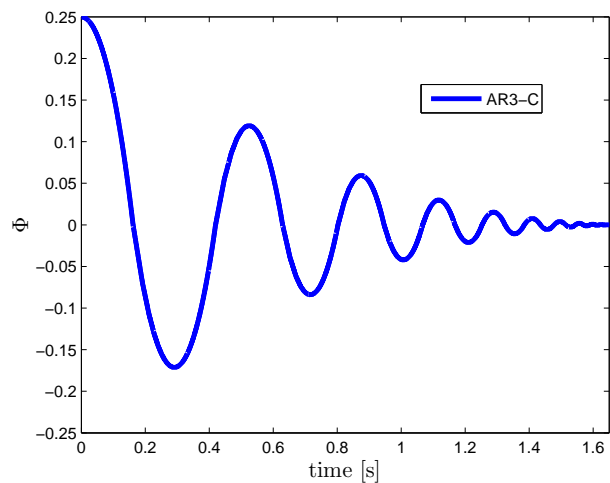


(a) simulation, $e_{n,i}^* = 0.8$, $l = 4.9L$, $L = 0.19\text{m}$.

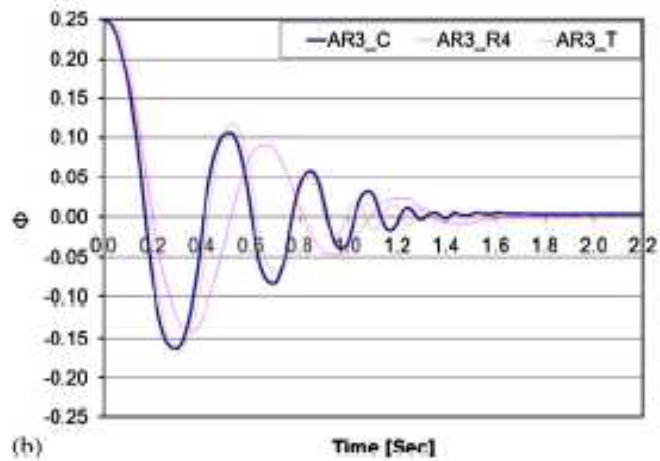


(b) figure 10 (a) in [17].

Figure 54: Responses for specimen AR5-C.

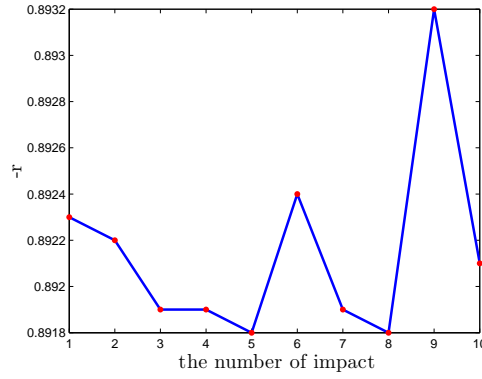


(a) simulation, $c_{n,i}^* = 0.8$, $l = 3L$, $L = 0.19\text{m}$.

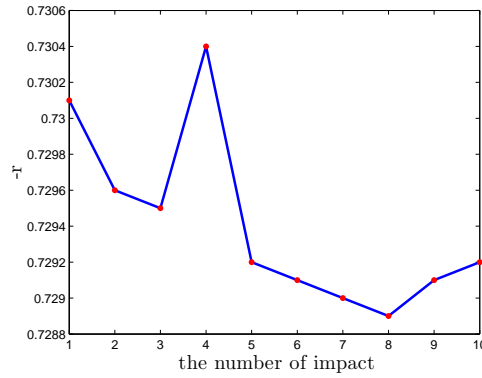


(b) figure 10 (b) in [17].

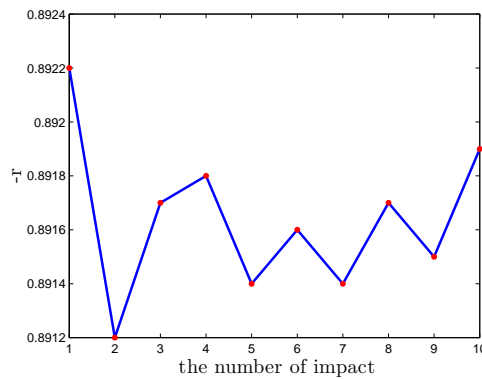
Figure 55: Responses for specimen AR3-C.



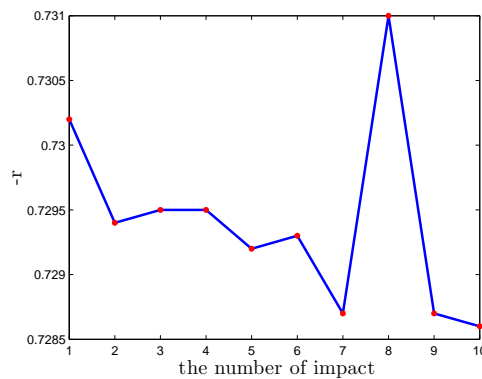
(a) Data from figure 52 (a)



(b) Data from figure 53 (a)



(c) Data from figure 54 (a)



(d) Data from figure 55 (a)

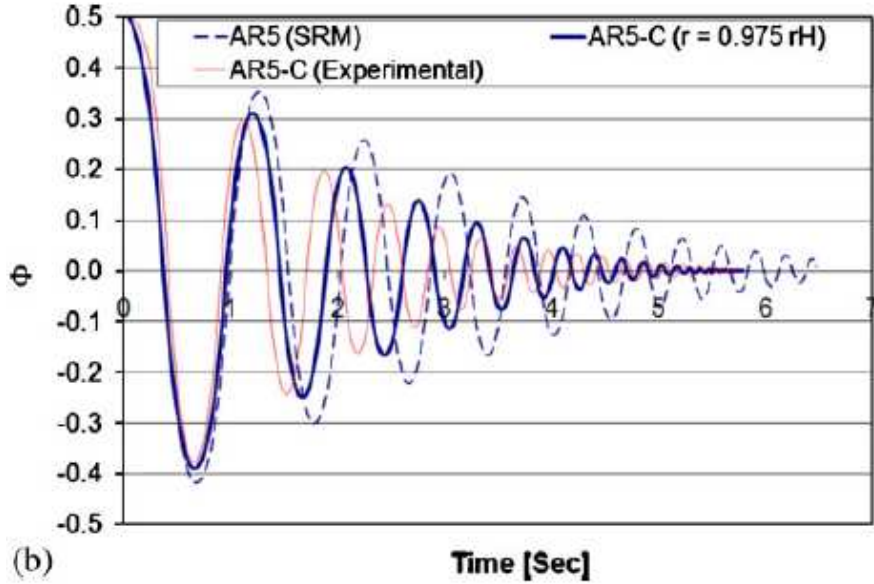


Figure 57: Comparison between experimental and numerical results with kinematic law (Housner angular restitution) (figure 18 (b) in [17]).

| Peak number | LZB model | Experiments |
|-------------|-----------|-------------|
| 1 | -0.21 | -0.21 |
| 2 | 0.17 | 0.17 |
| 3 | -0.15 | -0.15 |
| 4 | 0.13 | 0.11 |
| 5 | -0.10 | -0.10 |
| 6 | 0.08 | 0.075 |
| 7 | -0.075 | -0.07 |
| 8 | 0.06 | 0.055 |
| 9 | -0.05 | -0.05 |
| 10 | 0.045 | 0.045 |

Table 12: Peak magnitudes, figure 54.

6.4 Conclusions

The above results show that the LZB model is rich enough to reproduce a variety of block's motions. For the purely planar block we have shown that the kinetic angle θ_{12} between the two unilateral constraints plays a significant role in the block's dynamics, both in the frictionless and the frictional cases. This was expected in view of some previous mathematical results on the discontinuity of the trajectories w.r.t. the initial conditions. It seems that the blocks may be classified as follows:

| Peak number | LZB model | Experiments |
|-------------|-----------|-------------|
| 1 | -0.17 | -0.16 |
| 2 | 0.12 | 0.11 |
| 3 | -0.08 | -0.08 |
| 4 | 0.06 | 0.06 |
| 5 | -0.04 | -0.04 |
| 6 | 0.025 | 0.025 |

Table 13: Peak magnitudes, figure 55.

| Impact number | LZB model | Experiments |
|---------------|-----------|-------------|
| 1 | 0.27s | 0.25s |
| 2 | 0.65s | 0.60s |
| 3 | 0.95s | 0.85s |
| 4 | 1.2s | 1.1s |
| 5 | 1.4s | 1.25s |

Table 14: Impact times, figure 53.

| Impact number | LZB model | Experiments |
|---------------|-----------|-------------|
| 1 | 0.20s | 0.30s |
| 2 | 0.60s | 0.50s |
| 3 | 0.80s | 0.85s |
| 4 | 1.20s | 1.20s |
| 5 | 1.40s | 1.50s |
| 6 | 1.65s | 1.60s |
| 7 | 1.9s | 1.9s |
| 8 | 2.1s | 2.0s |
| 9 | 2.25s | 2.2s |

Table 15: Impact times, figure 54.

| Impact number | LZB model | Experiments |
|---------------|-----------|-------------|
| 1 | 0.16s | 0.17s |
| 2 | 0.40s | 0.40s |
| 3 | 0.61s | 0.60s |
| 4 | 0.80s | 0.75s |
| 5 | 0.95s | 0.90s |
| 6 | 1.05s | 1.05s |

Table 16: Impact times, figure 55.

- blocks which rock:
 - two dimensional blocks, (*i.e.* blocks for which the dynamics is planar.
 - three dimensional blocks, (*i.e.* blocks for which the dynamics obviously involves frictional or impact effects due to the thickness.
- blocks which do not rock:
 - because of low friction (slip dominates stick).
 - because of low aspect ratio $\frac{1}{L}$.

In this work we have shown the importance of the kinetic angle θ_{12} between the two constraint surfaces, which allows one to roughly split the planar blocks into two classes: slender blocks with $\theta_{12} > \frac{\pi}{2}$, flat blocks with $\theta_{12} < \frac{\pi}{2}$. In three dimensions, there are four unilateral constraints $f_1(q) \geq 0$, $f_2(q) \geq 0$, $f_3(q) \geq 0$, $f_4(q) \geq 0$, and six kinetic angles θ_{12} , θ_{13} , θ_{14} , θ_{23} , θ_{24} , θ_{34} . For instance a tower block like specimen 3 of [46] has all angles $\theta_{ij} > \frac{\pi}{2}$. A slice block like specimen 4 of [46] clearly has some of its kinetic angles (those corresponding to the “thickness” direction) $< \frac{\pi}{2}$ while the “planar” ones may be larger or smaller than $\frac{\pi}{2}$. An open research direction may be the classification of blocks depending on their kinetic angles.

As already noted above, in some instances a kinematic law of restitution can be used to model the block’s motion (rocking, half-rocking). However the problem is that such a model is unable to *predict* the real motion, it can only be used if one knows *a priori* that the motion is of the rocking type or else. The classical model for blocks is that of Housner, which is able to reproduce the motion only if rocking occurs. The LZB model which we use in this paper uses one restitution coefficient *per contact*. The advantage is that if rocking does occur (with perfectly sticking contact points), then our model predicts it and provides as good results as the (enhanced) angular velocity restitution model. But it is much more rich and can reproduce a variety of motions that are not accessible to the simple rocking model.

7 Impacts with Coulomb friction (harmonic base excitation)

We now consider that the ground is an excited base, with horizontal motion of the form $\mathbf{A} \sin(\omega t)$. The major issues are to determine the conditions of the onset of rocking, and of the overturning phenomenon (so that this can be avoided in practice). In this section we provide comparisons with experimental data (corroborating the above good results for free-rocking), and then an analysis of the onset of rocking and of the overturning is presented.

7.1 Comparisons with experiments in [46]

Some experiments with horizontal base excitation have been given in [46]⁷. The parameters $e_{n,i}^*$ and μ , μ_s in the LZB model are those obtained from the free-rocking fitting process of section 6.1. The free-rocking experiments may thus be

⁷Once again we use here some data provided to us by Dr F. Pena from UNAM, Mexico.

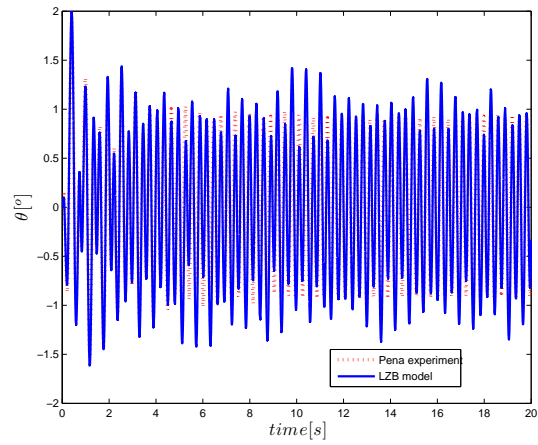
considered as a simple process for parameters fitting. The results are reported in figure 58. It is seen that the LZB model has the tendency to underestimate the peaks magnitudes, however the frequency of the response is very well predicted. As shown in Figure 12 in [46] through repeatability tests, the amplitude of the rocking angle $\theta(t)$ may vary from one experiment to the other, which may explain that the LZB model does not predict the same amplitude as in the experimental figures.

7.2 Study of the onset of rocking

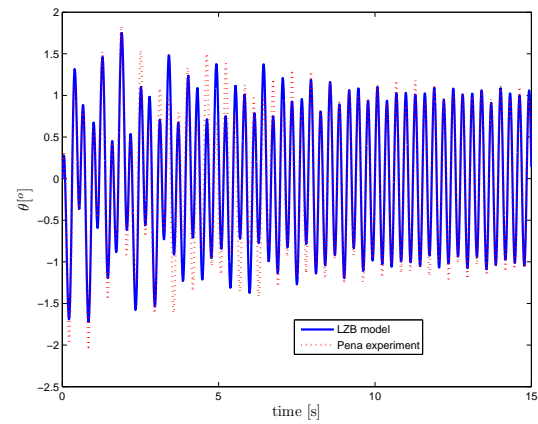
In this section we continue the study of section 5.1: can we exhibit some critical kinetic angles for the onset of rocking motion and for the onset of the overturning phenomenon? To start with the onset of rocking motion in the (\mathbf{A}, ω) plane is depicted in figure 59 with the experimental data taken from Table 4 in [46]. They concern specimen 2 with $l = 1\text{m}$, $L = 0.17\text{m}$, $d = 0.502\text{m}$, $m = 228\text{ kg}$. A good matching is found between the numerical and the experimental results. Notice that it is considered that rocking is initiated if the block not only starts to rock on the base, but if this rocking motion is persistent in time (*i.e.* the mere detachment of one contact point is not sufficient to decide for rocking). The tendency is that rocking starts to occur for large \mathbf{A} when ω is small, and for small \mathbf{A} when ω is large. This tendency is also in agreement with the experimental data of figure 14 in [66].

Let us now consider figure 60, which depicts the onset of rocking as a function of the aspect ratio $\frac{l}{L}$ and the amplitude \mathbf{A} , for a fixed frequency $\frac{\omega}{2\pi} = 3.3\text{ hz}$. The points on the curve represent the lower limit of the necessary \mathbf{A} for onset of rocking, *i.e.* rocking occurs for magnitudes just larger. In figures 61 and 62 are depicted the trajectories $\theta(t)$ and the relative tangential velocity $\dot{x}_{rel}(t)$ at point A (or at point B since they are equal due to the block's rigidity). Flat blocks need a large \mathbf{A} to rock, while slender blocks rock for small \mathbf{A} . This seems intuitively clear. It is noteworthy that there exists a transition between all-stick regimes (slender blocks) and all-slip regimes (flat blocks). From figures 61 and 62 one sees that the transition occurs around $\frac{l}{L} = 3$. For $\frac{l}{L} = 3$ the relative velocity is almost always non zero, while for $\frac{l}{L} = 3.5$ it is almost always zero.

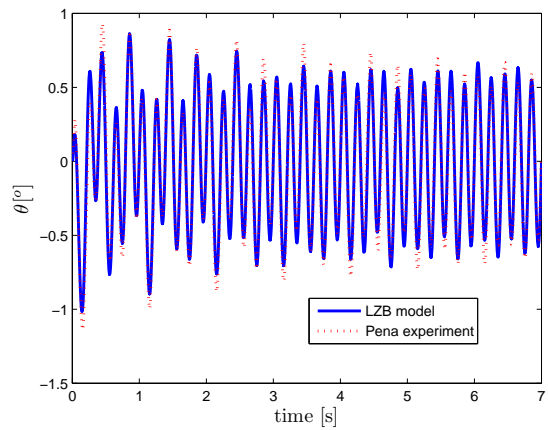
The figure 63 depicts the onset of rocking for base amplitude 5mm. The friction parameters are varied. For high enough friction the onset of rocking occurs almost independently of the friction, corroborating previous results [53]. For small enough friction however, there exists a minimum aspect ratio $\frac{l}{L}$ under which the onset of rocking starts to depend a lot on friction. When the friction is high enough the contacts statuses are mostly stick, therefore the value μ does not count whereas μ_s plays a role. Some interesting figures are reported in Tables 17 and 18. The parameters are $e_{n,i} = ??$, $\mu = ??$, $\mu_s = ??$, $m = ??$. These figures show that the product Af^2 that determines the onset of rocking, is almost constant for a given aspect ratio $\frac{l}{L}$. This is not surprising since Af^2 is directly related to the maximal acceleration of the base. Therefore the onset of rocking for a given aspect ratio, depends essentially on the maximal acceleration of the base. It is noteworthy that previous works report a criterion for the onset of rocking without sliding [27, 55, 49], which in fact reduces to a static equilibrium criterion $\mu_s \geq \frac{l}{L}$ (see *e.g.* equation (32) in [27]). The results obtained here do not make the sticking assumption, and some slipping phases are possible. Clearly this changes a lot the onset of rocking conditions, in which



(a) Frequency $\frac{\omega}{2\pi} = 3.3$ hz, amplitude $\mathbf{A} = 6$ mm (specimen 1)



(b) Frequency $\frac{\omega}{2\pi} = 3.3$ hz, amplitude $\mathbf{A} = 8$ mm (specimen 2)



(c) Frequency $\frac{\omega}{2\pi} = 3.3$ hz, amplitude $\mathbf{A} = 5$ mm (specimen 2)

Figure 58: $\theta(t)$ responses with base excitation.

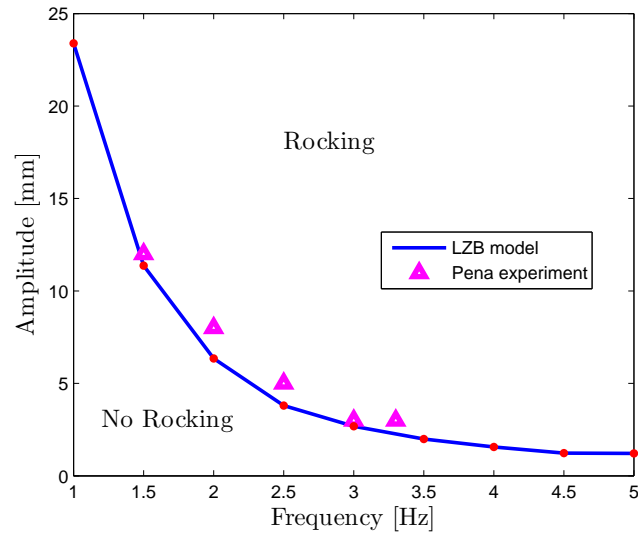


Figure 59: Onset of rocking for specimen 2.

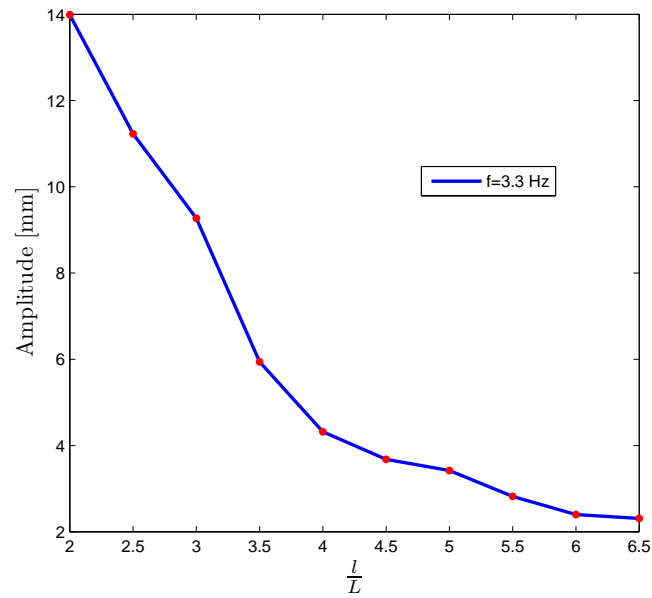


Figure 60: Onset of rocking, $L = 0.17\text{m}$, $\mu = 0.3$, $\mu_s = 0.577$.

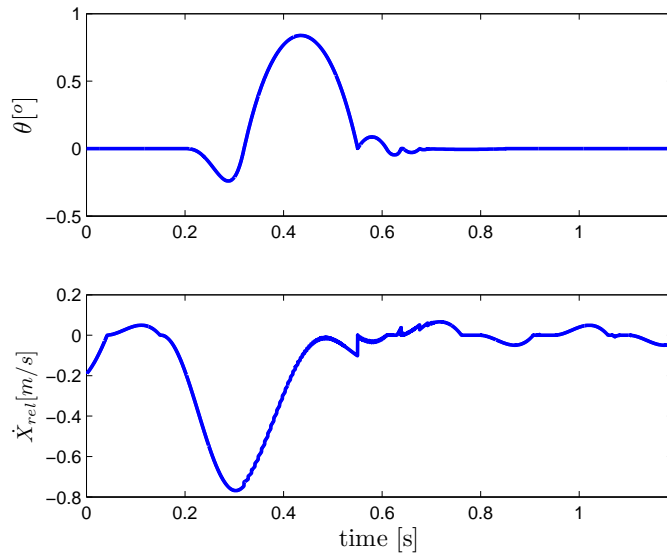


Figure 61: Responses $\theta(t)$ and relative tangential velocity, $\frac{l}{L} = 3$, $\mu = 0.3$, $\mu_s = 0.577$.

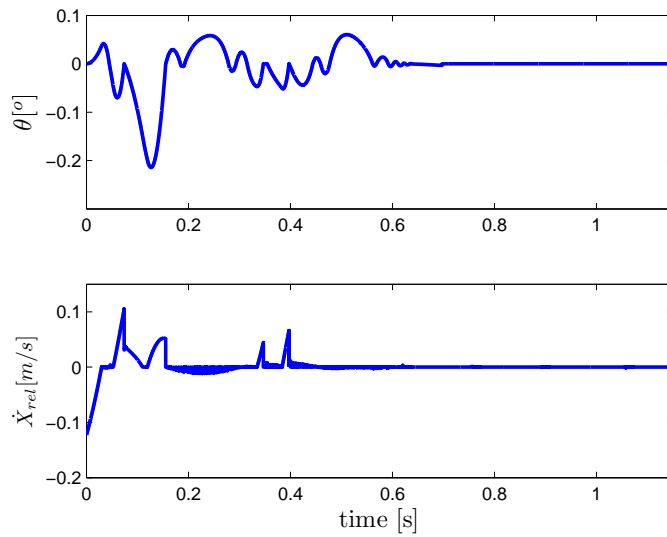


Figure 62: Responses $\theta(t)$ and relative tangential velocity, $\frac{l}{L} = 3.5$, $\mu = 0.3$, $\mu_s = 0.577$.

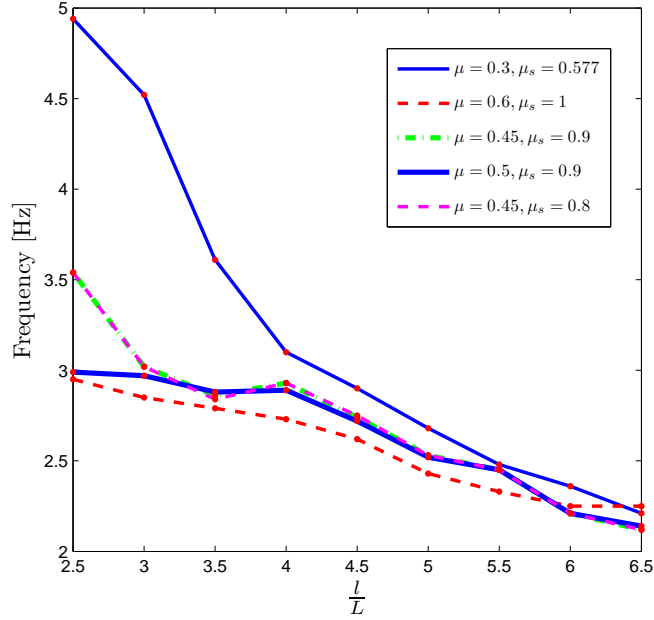


Figure 63: The onset of rocking with varying friction parameters.

| $\frac{l}{L}$ | 2.0 | 2.5 | 3.0 | 3.5 | 4.0 | 4.5 | 5.0 |
|--------------------------------|------------|----------|----------|---------|---------|---------|---------|
| f_1 ($A_1 = 3\text{mm}$) | 7.08 | 6.51 | 5.91 | 4.68 | 4.05 | 3.71 | 3.49 |
| A_2 ($f_2 = 3.3\text{Hz}$) | 13.99 | 11.23 | 9.27 | 5.94 | 4.32 | 3.68 | 3.42 |
| f_3 ($A_3 = 5\text{mm}$) | no rocking | 4.94 | 4.52 | 3.61 | 3.10 | 2.90 | 2.68 |
| f_4 ($A_4 = 7\text{mm}$) | no rocking | 4.16 | 3.85 | 3.06 | 2.56 | 2.41 | 2.25 |
| A_5 ($f_5 = 5.5\text{Hz}$) | no rocking | 4.93 | 4.09 | 2.57 | 1.94 | 1.58 | 1.42 |
| A_6 ($f_6 = 4\text{Hz}$) | no rocking | 7.58 | 6.32 | 4.07 | 3.01 | 2.64 | 2.17 |
| $A_1 f_1^2$ | 150.3792 | 127.1403 | 104.7843 | 65.7072 | 49.2075 | 41.2923 | 36.5403 |
| $A_2 f_2^2$ | 152.3511 | 122.2947 | 100.9503 | 64.6866 | 47.0448 | 40.0752 | 37.2438 |
| $A_3 f_3^2$ | no rocking | 122.0180 | 102.1520 | 65.1605 | 48.0500 | 42.0500 | 35.9120 |
| $A_4 f_4^2$ | no rocking | 121.1392 | 103.7575 | 65.5452 | 45.8752 | 40.6567 | 35.4375 |
| $A_5 f_5^2$ | no rocking | 123.25 | 102.25 | 64.25 | 48.5 | 39.5 | 35.5 |
| $A_6 f_6^2$ | no rocking | 121.28 | 101.12 | 65.12 | 48.16 | 42.24 | 34.72 |

Table 17: The products Af^2 varying with $\frac{l}{L}$.

the dynamical effects and the stick/slip transitions play a significant role. It is also noteworthy that our results are not based on some model approximations as done sometimes [1] but keep the full non-linearity of the dynamics. The results for $\frac{l}{L} < 2$ are not depicted in figure 63. Indeed for such values of the aspect ratio and for realistic values of friction, the onset of rocking occurs for very large values of the frequency and one may infer that rocking never occurs.

| | | | |
|--------------------------------|---------|---------|---------|
| $\frac{L}{l}$ | 5.5 | 6.0 | 6.5 |
| f_1 ($A_1 = 3\text{mm}$) | 3.35 | 2.96 | 2.80 |
| A_2 ($f_2 = 3.3\text{Hz}$) | 2.82 | 2.40 | 2.31 |
| f_3 ($A_3 = 5\text{mm}$) | 2.48 | 2.36 | 2.21 |
| f_4 ($A_4 = 7\text{mm}$) | 2.07 | 1.90 | 1.83 |
| A_5 ($f_5 = 5.5\text{Hz}$) | 1.20 | 1.13 | 1.02 |
| A_6 ($f_6 = 4\text{Hz}$) | 1.86 | 1.66 | 1.53 |
| $A_1 f_1^2$ | 33.6675 | 26.2848 | 23.5200 |
| $A_2 f_2^2$ | 30.7098 | 26.1360 | 25.1559 |
| $A_3 f_3^2$ | 30.7520 | 27.8480 | 24.4205 |
| $A_4 f_4^2$ | 29.9943 | 25.27 | 23.4423 |
| $A_5 f_5^2$ | 30 | 28.25 | 25.5 |
| $A_6 f_6^2$ | 29.76 | 26.56 | 24.48 |

Table 18: The products Af^2 varying with $\frac{l}{L}$.

7.3 Study of the overturning phenomenon

7.3.1 Harmonic base excitation

Many studies have been devoted to the overturning phenomenon, see *e.g.* [1, 8, 19, 25, 26, 27, 28, 52, 54, 56, 62, 66]. Here we first consider a horizontal harmonic motion of the base of the above form $\mathbf{A} \sin(\omega t)$. It is expected that the overturning phenomenon hardly obeys simple rules, because it is known that the block's dynamics with moving base is an extremely sensitive process with respect to initial data and parameters, especially when restitution is high and stick/slip occurs [25]. In all the figures the curves are numbered starting with the smallest magnitude, or with the smallest frequency. The overturning is the result of an "optimal" exchange of energy between the base and the block, through an increase of the block's oscillation magnitude. This is illustrated in figure 64 (a), where the $\theta(t)$ response is depicted during 6s, with frequency $\frac{\omega}{2\pi} = 3.3\text{Hz}$, $e_{n,i}^* = 0.99$, $\frac{l}{L} = 6$ and $L = 0.155\text{m}$. This figure demonstrates that overturning may occur quickly for $\mathbf{A} = 40, 55, 60, 70, 30, 50\text{mm}$, later for $\mathbf{A} = 25, 35, 45, 65\text{mm}$, and not overturn for $\mathbf{A} = 15\text{mm}$ before 6s. In all cases the block's motion before the overturn is quite similar in frequency and amplitude. This indicates that the overturn is the result of a sudden "break" in the base/block relative motion. Figure 64 (b) shows that decreasing $e_{n,i}^*$, *i.e.* adding normal dissipation at the impacts, decreases significantly the risk of overturning since all amplitudes $\mathbf{A} \leq 40\text{mm}$ yield stable rocking. Figure 64 (c) shows that decreasing \mathbf{A} may yield a stable rocking motion after some transient, as may be expected. In figure 65 the same study is done with varying frequencies and fixed $\mathbf{A} = 3\text{mm}$. Similar conclusions as for the varying amplitude can be drawn, that there is no monotonic variation of the overturning phenomenon as a function of the base frequency. Discontinuities in the dynamical behaviour are common in systems with impact and Coulomb friction. It is expected that more energy dissipation is going to prevent the block from overturning. Dissipation may come from two sources: sliding motions and normal restitution. The friction between the base and the block mainly influences the onset of rocking, for if $\mu = \mu_s = 0$ the block's corners never detach from the base. However when rocking has

been established the most efficient way to “control” the overturning *via* energy dissipation is through the normal restitution.

Two comments are in order:

- In all the simulated cases of figures 64 and 65 there exist rebound phases after each impact at the corners. This means that the period of times with persistent contact between the ground and the block are very short or even vanish. Such bouncing phases tend to vanish when the slenderness increases.
- The base excitation is a persistent one. This means that it is difficult to assert firmly whether a motion is really stable or not, because the mechanism of energy transmission between the base and the block is very complex. For instance we cannot say if the motion with $\mathbf{A} = 40\text{mm}$ in figure 64 (b) is stable or not on a long term. This is why studying overturning with simpler base excitations like one sine period only may be useful.

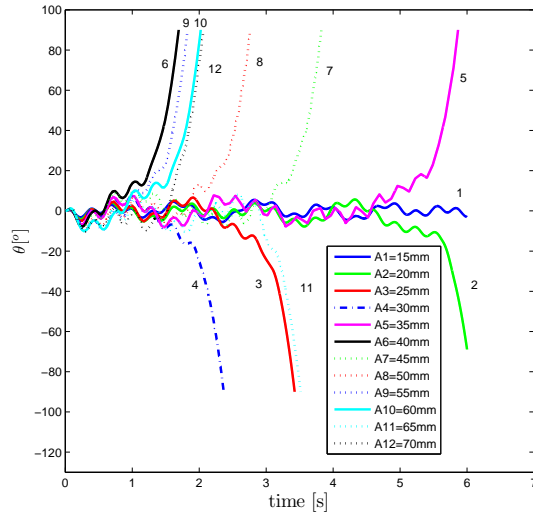
7.3.2 Pulse-type base excitation

We now consider that the base has the pulse-type motion (called one-sine type-A pulse in [26, 36, 70]) with an acceleration equal to:

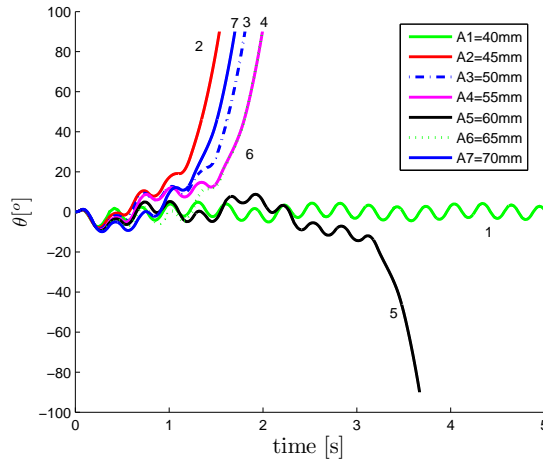
$$\dot{v}_b(t) = \begin{cases} a_p \sin(\omega_p t + \psi) & \text{if } -\frac{\psi}{\omega_p} \leq t \leq \frac{2\pi - \psi}{\omega_p} \\ 0 & \text{otherwise} \end{cases} \quad (43)$$

with $\psi = \arcsin(\frac{\alpha g}{a_p})$, $\alpha = \arctan(\frac{L}{l})$. The advantage of considering such base excitation is that it allows one to clearly separate the motions that overturn and those that do not overturn. Indeed once the base is at rest, the block may only lose energy. If it has not overturned before it starts to lose its energy, it will never overturn. This has been used in [26, 70], where one can find numerical results about the safe and unsafe areas depending on the amplitude and frequency of the base excitation (see for instance figure 6 in [26]). The results are reported in figures 66 to 70. The parameters are chosen as in [36, Figure 5], *i.e.* $l = 1.555$, $L = 0.3971$, $e_n^* = 0.9$, so that $p = \sqrt{\frac{3g}{4R}} = 2.14$ and $\alpha = \arctan(\frac{L}{l}) = 0.25$.

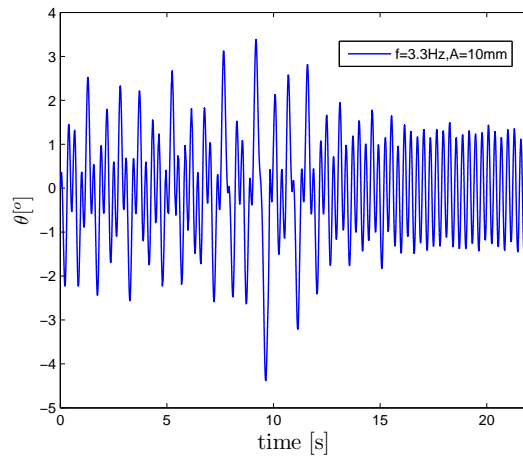
- In figure 66 are depicted various areas in the $(\frac{a_p}{\alpha g}, \frac{\omega_p}{p})$ plane. Qualitatively we recover the same shapes as in [26, Figure 6] or [36, Figures 5, 8, 9]: a big area (above the curve AGH or above the curve $AGJK$) within which overturning occurs with no impact, and a smaller “tongue shaped” area (within $AIDCB$ for $\mu = 0.3$, $\mu_s = 0.8$, different for the other two frictions) where overturning occurs after one or several impacts. There are however major discrepancies with respect to the results in [26, 36, 70]:
 - The models used in [26, 70] are of the Housner type, with basic assumptions like no slipping phases, and a constant angular velocity restitution r . The LZB model includes Coulomb friction and allows for stick/slip behaviour both outside and during the impacts, with a coherent energetical behaviour. Figures 67, 68, 69 (g) (h) (i) show



(a) Overturning amplitudes, $e_{n,i}^* = 0.99$.



(b) Overturning amplitudes, $e_{n,i}^* = 0.8$.



(c) Non-overturning amplitude.

RR n° 7580

Figure 64: The overturning with varying A , $f = 3.3\text{Hz}$.

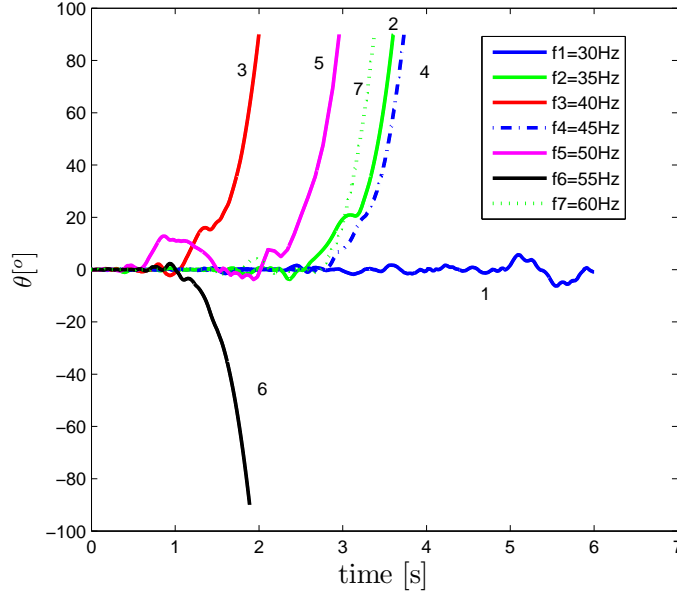


Figure 65: The overturning with varying ω , $\mathbf{A} = 3\text{mm}$.

that there is always an important slipping phase before the block overturns.

- Consider the case $\mu = 0.5$, $\mu_s = 0.8$. The overturn in the area above the line AB and below the line AF , occurs after two impacts (which is new compared to [26, Figure 6] which indicates only one impact). There is a discontinuity between points B and C , because the overturning in the area above CD and below the next curve AFI occurs with one impact only.
- The overturning area with one or two impacts, is larger than the one-impact overturning area in [26, Figure 6].
- As expected the safe area increases when the friction decreases, that indicates that more slip implies less overturn. In the frictionless limit there is no overturn since the block keeps slipping on the base.
- Figures 67 (a) (d) (g) correspond to a point on the line AB in figure 66, figures 67 (b) (e) (h) correspond to a point on the line CD , figures 67 (c) (f) (i) correspond to a point on the line AF . Figures 68 (a) (d) (g) correspond to a point on the line FE in figure 66, figures 68 (b) (e) (h) correspond to a point on the line AG , figures 68 (c) (f) (i) correspond to a point on the line FI . Figures 69 (a) (d) (g) correspond to a point on the line GJ in figure 66, figures 69 (b) (e) (h) correspond to a point on the line JI , figures 69 (c) (f) (i) correspond to a point in the right upper corner of figure 66.

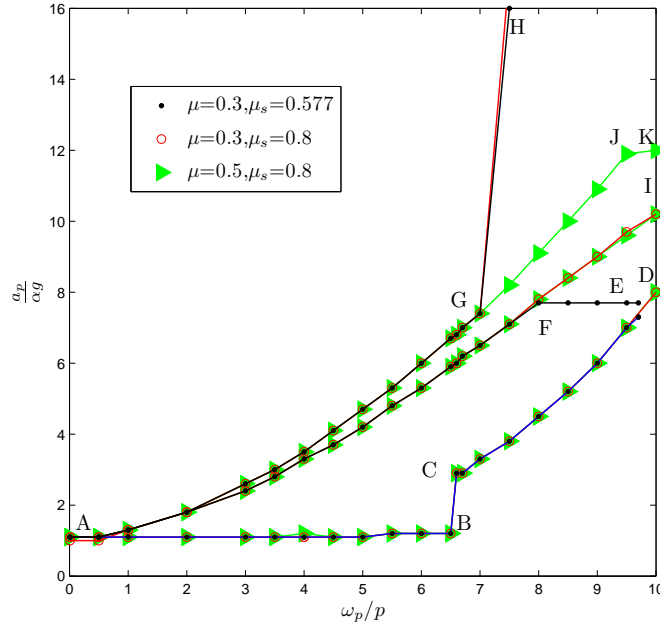


Figure 66: Overturning safe and unsafe areas.

- From figures 67, 68, 69 (g) (h) (i) one sees that the overturning is almost always occurring after a phase of slip, followed by a sticking phase at the point of contact (notice that the vertical scales in figures 67, 68, 69 (g) (h) (i) and in figures 67, 68, 69 (d) (e) (f) are quite different in magnitude).
- There are two impacts before the overturn in figure 67 (a). The first impact, however, has very small magnitude. In figure 70 (a) the first 0.3s of the simulation are zoomed, and the first impact can be seen when $\theta(t)$ crosses the zero value. In figure 70 (b) the first 0.5s of the $\theta(t)$ response of figure 67 (b) are shown and it is seen that there is only one impact before the overturn. Recall that these two cases correspond to points of the lines AB and CD respectively.

The overturning phenomenon is certainly the most complex phenomenon that may occur in the block/ground system. Our numerical results mainly aim at showing that the LZB model with friction, coupled to the complementarity system in (5) outside the impacts, may improve our knowledge about overturning in planar blocks. It is to be considered as a preliminary work because on the first hand three-dimensional effects are likely to play a significant role in most of the experiments with strong base excitation, on the second hand real earthquakes excitations are more complex than those considered here.

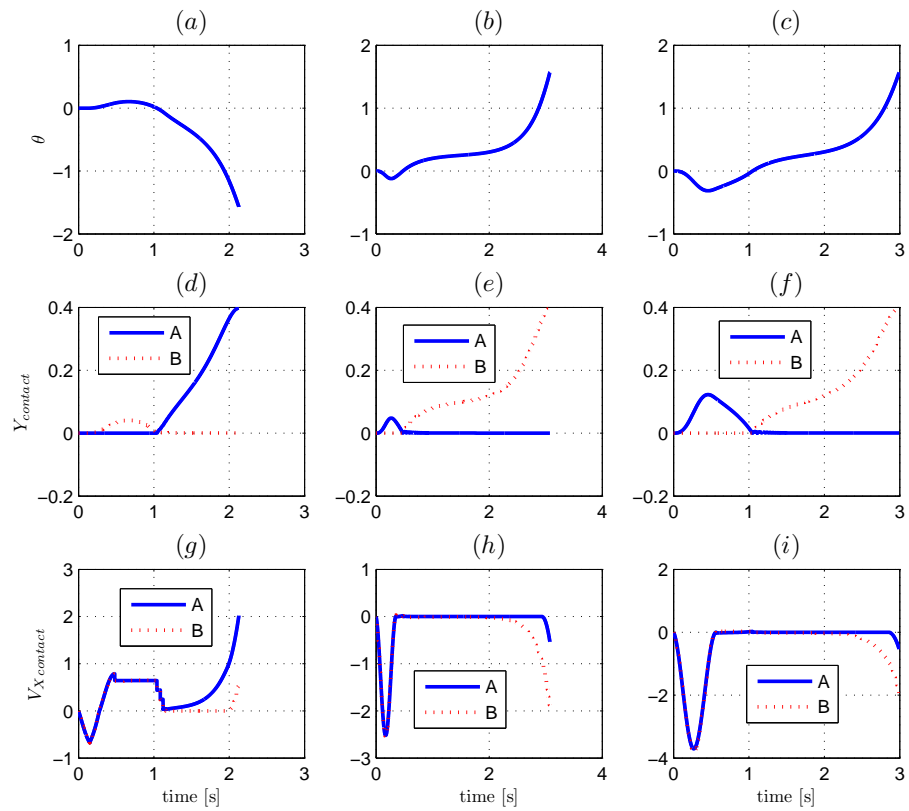


Figure 67: (a) (b) (c): $\theta(t)$, (d) (e) (f) vertical positions and (g) (h) (i) relative horizontal velocities of the contact points.

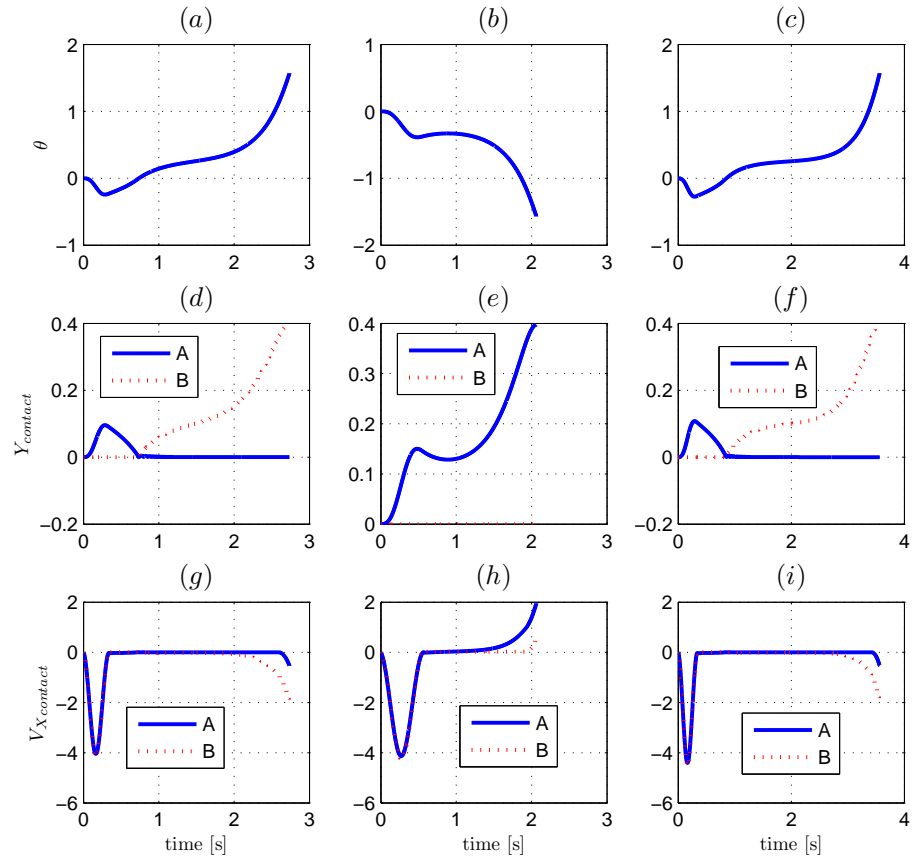


Figure 68: (a) (b) (c): $\theta(t)$, (d) (e) (f) vertical positions and (g) (h) (i) relative horizontal velocities of the contact points..

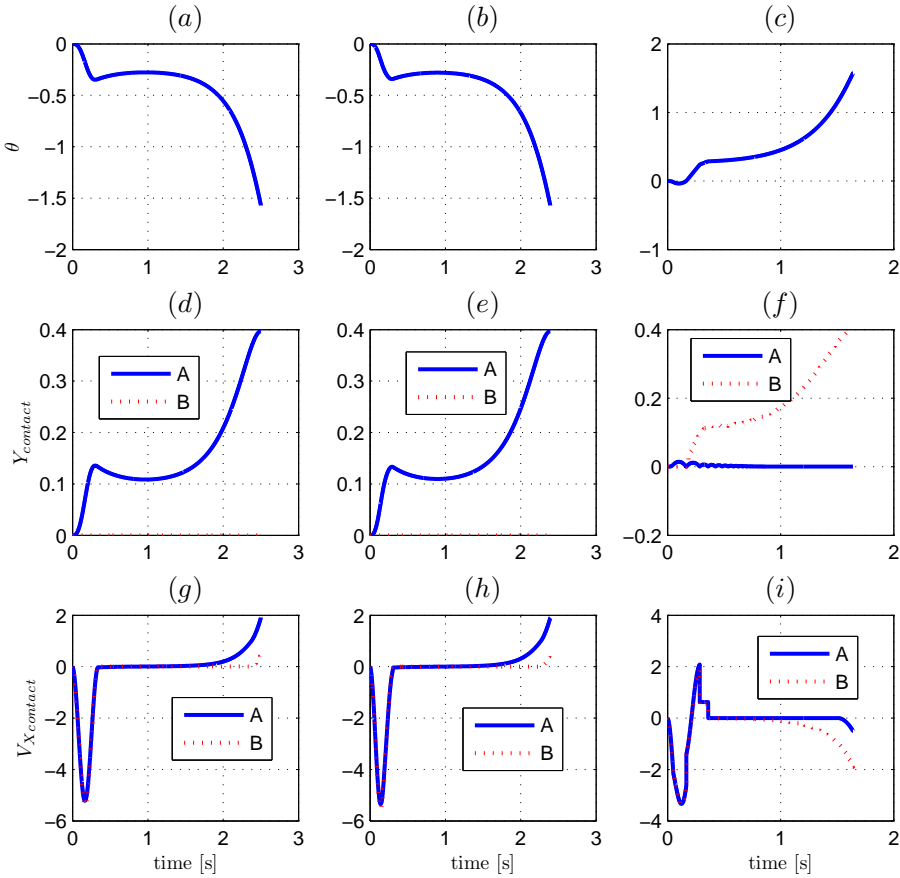


Figure 69: (a) (b) (c): $\theta(t)$, (d) (e) (f) vertical positions and (g) (h) (i) relative horizontal velocities of the contact points..

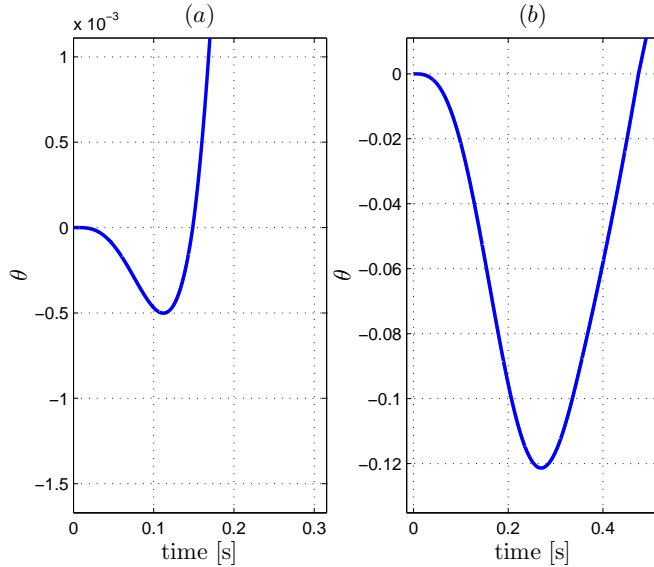


Figure 70: Zooms of figures 67 (a) and (b).

8 Conclusions

This report concerns the dynamics of a planar block subject to a unilateral constraint (the ground), possibly with Coulomb friction outside and during the impacts. It has four main objectives: 1) study a generalized kinematic (Newton's like) restitution law and show that it embeds the classical Hournier's angular velocity restitution law; 2) show that the LZB impact dynamics model recently introduced in [31, 32, 33, 71, 34] can be successfully applied to the block problem through numerous and detailed comparisons with experimental data found elsewhere (free-rocking and with base excitation); 3) show that the kinetic angle between the two constraint surfaces plays a fundamental role in the blocks dynamics and may be used as a macroscopic parameter to predict the block gross motion; 4) show that the LZB model allows to reproduce a large variety of the block's motion. The LZB model is a rigid body model, based on the Darboux-Keller's approach for impact dynamics, with few parameters (one energetical normal restitution and one static and dynamic friction coefficients *per* impact point). Compared to previously used contact/impact models in the rocking block literature, the LZB model allows one to incorporate Coulomb's friction both outside and during the impacts, and is not restricted to being fitted with some *a priori* known motion (like perfect rocking) but permits to *predict* the motion. An event-driven code is implemented and freely available in the open-source software platform SICONOS developed at the INRIA [3, 57], with which all the numerical results shown in this report can be obtained.

Acknowledgements: the authors are very grateful to Dr Fernando Pena (UNAM Mexico) for providing them with detailed figures from the experiments in [46]. These have been valuable for achieving this work.

A The numerical code for the impact dynamics integration

Here is the code that has been used for all the simulations. This is an event-driven simulation code.

References

- [1] H. Al Abadi, N/ Lam, E. Gad, “A simple displacement-based model for predicting seismically induced overturning”, *Journal of Earthquake Engineering*, vol.10, no 6, pp.775-814, 2006.
- [2] V. Acary, B. Brogliato, *Numerical Simulation for Nonsmooth Dynamical Systems*, Springer Verlag Heidelberg, Lecture Notes in Applied and Computational Mechanics, vol.35, 2008.
- [3] V. Acary, F. P erignon, “An introduction to SICONOS”, Technical Report INRIA RT-0340, <http://hal.inria.fr/inria-00162911/fr/>.
- [4] U. Andreaus, P. Casini, “On the rocking-uplifting motion of a rigid block in free and forced motion: influence of sliding and bouncing”, *Acta Mechanica*, vol.138, pp.219-241, 1999.
- [5] U. Andreaus, P. Casini, “Dynamics of three-block assemblies with unilateral deformable contacts. Part 1: contact modelling”, *Earthquake Engineering and Structural Dynamics*, vol.28, pp.1621-1636, 1999.
- [6] M. Aslam, W.G. Godden, D.T. Scalise, “Earthquake rocking response of rigid bodies”, *J. Struct. Engrg. ASCE*, vol.106, no 2, pp.377-392, 1980.
- [7] P. Ballard, “The dynamics of discrete mechanical systems with perfect unilateral constraints”, *Archive for Rational Mechanics and Applications*, vol.154, pp.199-274, 2000.
- [8] R. Boroschek, A. Iruretagoyena, “Controlled overturning of unanchored rigid bodies”, *Earthquake Engineering and Structural Dynamics*, vol.35, no 6, pp.695-711, 2006.
- [9] R.M. Brach, *Mechanical Impact Dynamics*, John Wiley, New-York, 1991.
- [10] B. Brogliato, *Nonsmooth Mechanics*, Springer London, 2nd Ed., 1999.
- [11] V. Ceanga, Y. Hurmuzlu, “A new look at an old problem: Newton’s cradle”, *ASME Journal of Applied Mechanics*, vol.68, no 4, pp.575-583, 2001.
- [12] A. Chatterjee, A. Ruina, “A new algebraic rigid-body collision law based on impulse space considerations”, *ASME J. of Applied Mechanics*, vol.65, pp.939-951, December 1998.
- [13] S. Djerassi, “Collision with friction; Part A: Newton’s hypothesis”, *Multi-body Systems Dynamics*, vol.29, pp.37-54, 2009.
- [14] S. Dorbolo, D. Volfson, L. Tsimring, A. Kudrolli, “Dynamics of a bouncing dimer”, *Physical Review Letters*, vol.95, no 4, art. no 044101, pp. 1-4, 2005.

-
- [15] R. Dzonou, M.D.P. Monteiro-Marques, “A sweeping process approach to inelastic contact problems with general inertia operators”, *European Journal of Mechanics A/Solids*, vol.26, no 3, pp.474-490, 2007.
- [16] A. Di Egidio, A. Contento, “Base isolation of slide-rocking non-symmetric rigid blocks under impulsive and seismic excitations”, *Engineering Structures*, vol.31, pp.2723-2734, 2009.
- [17] M.A. ElGawady, Q. Ma, J. W. Butterworth, J. Ingham, “Effects of interface material on the performance of free rocking blocks”, *Earthquake Engineering and Structural Dynamics*, 2010, in press.
- [18] E. Falcon, C. Laroche, S. Fauve, S. Coste, “Collision of a 1-D column of beads with a wall”, *European Physical Journal B* vol.5, no 1, pp. 111-131, 1998.
- [19] W.T. Fielder, L.N. Virgin, R.H. Plaut, “Experiments and simulation of overturning of an asymmetric rocking block on an oscillating foundation”, *European Journal of Mechanics, A/Solids*, vol.16, no 5, pp.905-923, 1997.
- [20] M. Frémond, *Collisions*, Istituto Poligrafico e Zecca Dello Stato s.p.a., Roma, 2007.
- [21] Ch. Glocker, “Concepts for modeling impacts without friction”, *Acta Mechanica*, vol.168, pp.1-19, 2004.
- [22] B. Heidenreich, *Small and Half-Scale Experimental Studies of Rockfall Impacts on Sandy Slopes*, PhD thesis, Ecole Polytechnique Fédérale de Lausanne, section de Génie Civil (CH), Thèse no 3059, 2004.
- [23] G.W. Housner, “The behaviour of inverted pendulum structures during earthquakes”, *Bulletin of the Seismological Society of America*, vol.53, no 2, pp.403-417, 1963.
- [24] B. Imre, S. Rabsamen, S.M. Springman, “A coefficient of restitution of rock materials”, *Computers and Geosciences*, vol.37, pp.339-350, 2008.
- [25] M.Y. Jeong, K. Suzuki, S.C.S. Yim, “Chaotic rocking behavior of freestanding objects with sliding motion”, *Journal of Sound and Vibration*, vol.262, pp.1091-1112, 2003.
- [26] D. Konstantinidis, N. Makris, “Experimental and analytical studies on the responses of 1/4-scale models of freestanding laboratory equipment subjected to strong earthquake shaking”, *Bulletin Earthquake Engineering*, vol.8, pp.1457-1477, 2010.
- [27] A.N. Kounadis, “On the overturning instability of a rectangular rigid block under ground excitation”, *The Open Mechanics Journal*, vol.4, pp.43-57, 2010.
- [28] S. Lenci, G. Rega, “A dynamical systems approach to the overturning of rocking block”, *Chaos, Solitons and Fractals*, vol.28, no 2, pp.527-542, 2006.
- [29] P.R. Lipscombe, S. Pellegrino, “Free rocking of prismatic blocks”, *Journal of Engineering Mechanics*, vol.119, no 7, pp.1387-1410, July 1993.

-
- [30] P. Lipscombe, *Dynamics of Rigid Block Structures*, PhD Thesis, University of Cambridge, UK, 1990.
- [31] C. Liu, Z. Zhao, B. Brogliato, 2008 “Frictionless multiple impacts in multi-body systems: Part I. Theoretical framework”, *Proceedings of the Royal Society A, Mathematical, Physical and Engineering Sciences*, vol.464, no 2100, pp.3193-3211, December.
- [32] C. Liu, Z. Zhao, B. Brogliato, 2008 “Energy dissipation and dispersion effects in a granular media”, *Physical Review E*, vol.78, no 3, 031307, September.
- [33] C. Liu, Z. Zhao, B. Brogliato, 2008 “Variable structure dynamics in a bouncing dimer”, *INRIA Research Report 6718*, November, <http://hal.inria.fr/inria-00337482/fr/>.
- [34] C. Liu, Z. Zhao, B. Brogliato, 2009 “Frictionless multiple impacts in multi-body systems: Part II. Numerical algorithm and simulation results”, *Proceedings of the Royal Society A, Mathematical, Physical and Engineering Sciences*, vol.465, no 2101, pp.1-23, January.
- [35] V. Lubarda, “The bounds on the coefficients of restitution for the frictional impact of rigid pendulum against a fixed surface”, *Journal of Applied Mechanics, Transactions ASME*, vol.77, no 1, pp.1-7, 2010.
- [36] N. Makris, J. Zhang, “Rocking response and overturning of anchored equipment under seismic excitations”, *PEER Report 1999/06*, Pacific Earthquake Engineering Research Center, College of Engineering, University of California, Berkeley, November 1999, available at <http://nisee.berkeley.edu/elibrary/Text/1200242>.
- [37] S.A. Modarres Najafabadi, J. Kövecses, J. Angeles, “Generalization of the energetic coefficient of restitution for contacts in multibody systems”, *ASME J. of Computational and Nonlinear Dynamics*, vol.3, pp.041008-1 – 041008-14, October 2008.
- [38] M.D.P. Monteiro-Marques, *Differential Inclusions in Nonsmooth Mechanical Problems. Shocks and Dry Friction*, Progress in Nonlinear Differential Equations and their Applications, vol.9, Birkhauser, Basel, 1993.
- [39] J. Milne, “Seismic experiments”, *Trans. Seism. Soc. Japan*, vol.8, pp.1-82, 1885.
- [40] J.J. Moreau, “Some numerical methods in multibody dynamics: application to granular materials”, *European Journal of Mechanics A/Solids*, vol.13, no 4, pp.93-114, 1994.
- [41] H. Mouzakis, I. Psycharis, D. Papastamadiou, P. Carydis, C. Pantanopoulos, C. Zamba, “Experimental investigation of the earthquake response of a model of a marble classical column”, *Earthquake Engineering and Structural Dynamics*, vol.31, pp.1681-1698, 2002.
- [42] A. Palmeri, N. Makris, “Response analysis of rigid structures rocking on viscoelastic foundation”, *Earthquake Engineering and Structural Dynamics*, vol.37, pp.1039-1063, 2008.

-
- [43] L. Paoli, "Continuous dependence on data for vibro-impact problems", *Math. Models Methods Appl. Sci. (M3AS)*, vol.15, no 1, pp.1-41, 2005.
- [44] M. Payr, C. Glocker, "Experimental treatment of multiple contact collisions", *Euromech Conference ENOC*, Eindhoven, 7-12 August, pp.450-459, 2005.
- [45] F. Pena, F. Prieto, P.B. Lourenço, A. Campos Costa, J.V. Lemos, "On the dynamics of rocking motion of single rigid-block structures", *Earthquake Engineering and Structural Dynamics*, vol.36, pp.2383-2399, 2007.
- [46] F. Pena, P.B. Lourenço, A. Campos-Costa, "Experimental dynamic behavior of free-standing multi-block structures under seismic loadings", *Journal of Earthquake Engineering*, vol.12, pp.953-979, 2008.
- [47] J. Perry, "Note on the rocking of a column", *Trans. Seism. Soc. Japan*, vol.3, pp.103-106, 1881.
- [48] M.J.N. Priestley, R.J. Evenson, A.J. Carr, "Seismic response analysis of structures free to rock on their foundations", *Bull. of the New Zealand Seis. Soc. for Earthquake Engrg.*, vol.11, no 3, pp.141-150, 1978.
- [49] A. Pompei, A. Scalia, M.A. Sumbatyan, "Dynamics of rigid block due to horizontal ground motion", *J. Eng. Mech. ASCE*, vol.124, no 7, pp.713-717, 1998.
- [50] F. Prieto, P.B. Lourenço, "On the rocking behavior of rigid objects", *Mecanica*, vol.40, pp.121-133, 2005.
- [51] F. Prieto, P.B. Lourenço, C.S. Oliveira, "Impulsive Dirac-delta forces in the rocking motion", *Earthquake Engineering and Structural Dynamics*, vol.33, pp.839-857, 2004.
- [52] M.D. Purvance, A. Anooshehpour, J.N. Brune, "Freestanding block overturning fragilities: Numerical simulation and experimental validation", *Earthquake Engineering and Structural Dynamics*, vol.37, pp.791-808, 2008.
- [53] M. Raous, "Experimental analysis of the rocking of a rigid block", 3rd Pan American Congress of Applied Mechanics (PACAM III), Sao Paulo, Brazil, January 4-8 1993,
- [54] Y. Shao, C.C. Tung, "Seismic response of temporary structures", *Nuclear Engineering and Design*, vol.181, pp.267-274, 1998.
- [55] H.W. Shenton, "Criteria for initiation of slide, rock, and slide-rock rigid-body modes", *J. Eng. Mech. ASCE*, vol.122, no 7, pp.690-693, 1996.
- [56] B. Shi, A. Anooshenhpour, Y. Zeng, J.N. Brune, "Rocking and overturning of precariously balanced rocks by earthquakes", *Bulletin of the Seismological Society of America*, vol.86, no 5, pp.1364-1371, October 1996.
- [57] <http://siconos.gforge.inria.fr/>

- [58] A. Sinopoli, “Earthquakes and large block monumental structures”, *Annali di Geofisica*, vol. XXXVIII, no 5-6, p.737-751, November-December 1995.
- [59] P.D. Spanos, A.S. Koh, “Rocking of rigid blocks during harmonic shaking”, *J. Engrg. Mech.*, vol.110, no 11, pp.1627-1642, 1984.
- [60] A.B. Stevens, C.M. Hrenya, “Comparison of soft-sphere models to measurements of collision properties during normal impacts”, *Powder Technology*, vol.154, pp.99-109, 2005.
- [61] W.J. Stronge, *Impact Mechanics*, Cambridge University Press, 2000.
- [62] T. Taniguchi, “Non-linear response analyses of rectangular rigid bodies subjected to horizontal and vertical ground motion”, *Earthquake Engineering and Structural Dynamics*, vol.31, pp;1481-1500, 2002.
- [63] M. Tsesarsky, Y.H. Hatzor, N. Sitar, “Dynamic displacement of a block on an inclined plane: Analytical, experimental and DDA results”, *Rock Mechanics and Rock Engineering*, vol.38, no 2, pp.153-167, 2005.
- [64] W.K. Tso, C.M. Wong, “Steady state rocking response of rigid blocks. Part 1: Analysis”, *Earthquake Engineering and Structural Dynamics*, vol.18, no 1, pp.89-106, 1989.
- [65] W.K. Tso, C.M. Wong, “Steady state rocking response of rigid blocks. Part 2: Experiment”, *Earthquake Engineering and Structural Dynamics*, vol.18, no 1, pp.107-120, 1989.
- [66] T. Winkler, K. Meguro, F. Yamazaki, “Response of rigid body assemblies to dynamic excitation”, *Earthquake Engineering and Structural Dynamics*, vol.24, pp.1389-1408, 1995.
- [67] C. Yilmaz, M. Gharib, Y. Hurmuzlu, “Solving frictionless rocking block problem with multiple impacts”, *Proc. R. Soc. A*, vol.465, pp.3323–3339, 2009.
- [68] C.S. Yim, A.K. Chopra, J. Penzien, “Rocking response of rigid blocks to earthquakes”, *Earthquake Engineering and Structural Dynamics*, vol.8, no 6, pp.565-587,1980.
- [69] S.C.S. Yim, H. Lin, “Nonlinear impact and chaotic response of slender rocking objects”, *J. Eng. Mech.*, vol.117, pp.2079-2100, 1991.
- [70] J. Zhang, N. Makris, “Rocking response of anchored blocks under pulse-type motions”, *Journal of Engineering Mechanics*, vol.127, no 5, pp.411-529, 2001.
- [71] Z. Zhao, C. Liu, B. Brogliato, 2009 “Planar dynamics of a rigid body system with frictional impacts. II. Qualitative analysis and numerical simulations”, *Proceedings of the Royal Society A, Mathematical, Physical and Engineering Sciences*, vol.465, no 2107, pp. 2267-2292, July.

Contents

1 Introduction

3

| | | |
|----------|--|------------|
| 2 | The generalized kinematic restitution approach | 4 |
| 2.1 | The block dynamics | 4 |
| 2.2 | A generalized kinematic restitution mapping | 6 |
| 2.3 | Application to the block impact dynamics | 9 |
| 2.3.1 | Diagonal \mathcal{E}_n , $p_{n,1}(t) \neq 0$, $p_{n,2}(t) = 0$ (sliding rocking motion) | 10 |
| 2.3.2 | Diagonal \mathcal{E}_n , $p_{n,1}(t) \neq 0$, $p_{n,2}(t) \neq 0$ (sliding rocking block) | 11 |
| 2.3.3 | General \mathcal{E}_n , $p_{n,1}(t) \neq 0$, $p_{n,2}(t) \neq 0$ (sliding rocking block) | 11 |
| 2.3.4 | General \mathcal{E}_n , $p_{n,1}(t) \neq 0$, $p_{n,2}(t) \neq 0$ (sticking rocking block) | 12 |
| 2.3.5 | Diagonal \mathcal{E}_n , $p_{n,1}(t) \neq 0$, $p_{n,2}(t) \neq 0$ (half-rocking block) | 13 |
| 2.3.6 | Diagonal \mathcal{E}_n , $p_{n,1}(t) \neq 0$, $p_{n,2}(t) \neq 0$, with Coulomb's friction | 14 |
| 2.4 | The angular velocity restitution law | 14 |
| 2.4.1 | Sliding rocking block | 14 |
| 2.4.2 | Sticking free-rocking block | 16 |
| 2.4.3 | Half-rocking block | 18 |
| 2.5 | Characteristic kinetic angles | 18 |
| 2.6 | General \mathcal{E}_n , $p_{n,1}(t) \neq 0$, $p_{n,2}(t) \neq 0$, rebound at B | 19 |
| 2.7 | Conclusions | 20 |
| 3 | The extended Darboux-Keller impact dynamics | 24 |
| 4 | The frictionless case | 26 |
| 5 | Impacts with Coulomb friction (fixed base) | 34 |
| 5.1 | The role of the kinetic angle | 34 |
| 5.2 | Rocking motions | 44 |
| 5.3 | Conclusions | 50 |
| 6 | Comparisons with free-rocking experimental data | 50 |
| 6.1 | Experimental data in Pena et al [46] | 53 |
| 6.1.1 | The $\theta(t)$ response | 53 |
| 6.1.2 | The angular velocity restitution coefficient | 65 |
| 6.1.3 | Comments | 69 |
| 6.2 | Experimental data of Lipscombe et al [29] | 70 |
| 6.3 | Experimental data of Elgawady et al [17] | 72 |
| 6.4 | Conclusions | 84 |
| 7 | Impacts with Coulomb friction (harmonic base excitation) | 86 |
| 7.1 | Comparisons with experiments in [46] | 86 |
| 7.2 | Study of the onset of rocking | 87 |
| 7.3 | Study of the overturning phenomenon | 92 |
| 7.3.1 | Harmonic base excitation | 92 |
| 7.3.2 | Pulse-type base excitation | 93 |
| 8 | Conclusions | 100 |
| A | The numerical code for the impact dynamics integration | 101 |



Centre de recherche INRIA Grenoble – Rhône-Alpes
655, avenue de l'Europe - 38334 Montbonnot Saint-Ismier (France)

Centre de recherche INRIA Bordeaux – Sud Ouest : Domaine Universitaire - 351, cours de la Libération - 33405 Talence Cedex
Centre de recherche INRIA Lille – Nord Europe : Parc Scientifique de la Haute Borne - 40, avenue Halley - 59650 Villeneuve d'Ascq
Centre de recherche INRIA Nancy – Grand Est : LORIA, Technopôle de Nancy-Brabois - Campus scientifique
615, rue du Jardin Botanique - BP 101 - 54602 Villers-lès-Nancy Cedex
Centre de recherche INRIA Paris – Rocquencourt : Domaine de Voluceau - Rocquencourt - BP 105 - 78153 Le Chesnay Cedex
Centre de recherche INRIA Rennes – Bretagne Atlantique : IRISA, Campus universitaire de Beaulieu - 35042 Rennes Cedex
Centre de recherche INRIA Saclay – Île-de-France : Parc Orsay Université - ZAC des Vignes : 4, rue Jacques Monod - 91893 Orsay Cedex
Centre de recherche INRIA Sophia Antipolis – Méditerranée : 2004, route des Lucioles - BP 93 - 06902 Sophia Antipolis Cedex

Éditeur
INRIA - Domaine de Voluceau - Rocquencourt, BP 105 - 78153 Le Chesnay Cedex (France)
<http://www.inria.fr>
ISSN 0249-6399